# STRUCTURE AND ELECTROCHEMISTRY OF DNA-WRAPPED CARBON NANOTUBES

Jennifer F. Campbell

A dissertation submitted to the faculty of the University of North Carolina at Chapel Hill in partial fulfillment of the requirements for the degree of Doctor of Philosophy in the Department of Chemistry.

Chapel Hill
2009

Approved by:

Professor H. Holden Thorp

Professor Maurice S. Brookhart

Professor Dorothy A. Erie

Professor Michel R. Gagné

Professor Thomas J. Meyer

## Abstract

Jennifer F. Campbell: Structure and Electrochemistry of DNA-Wrapped Carbon Nanotubes
(Under the direction of H. Holden Thorp)

Single-walled carbon nanotubes (CNTs) are a one-dimensional nanomaterial with advantageous mechanical, optical, and electronic properties. An effective method of dispersing individual nanotubes in aqueous solution is to wrap CNTs with single-stranded DNA. To study the structure of this CNT–DNA, we employed atomic force microscopy. Results suggest DNA strands are helically wrapped with ~14-nm pitch and arranged end-to-end in a single layer along the CNT with a structure independent of the wrapping DNA length and sequence. Labeling the wrapping DNA with quantum dots demonstrated the useful functionalization of CNTs in a nondestructive manner and suggests nearly complete CNT surface coverage with DNA. To study CNT solution electrochemistry, we employed metal-mediated cyclic voltammetry. Oxidation of CNT–DNA by tris(2,2′-bipyridine)ruthenium(III) and similar electrogenerated oxidants was found to complete a catalytic cycle, enhancing metal oxidative peak current compared to a voltammogram of the metal alone. We observed an increase in this current enhancement at higher nanotube concentration, slower experimental scan rate, and higher metal redox potential. These observations were shown via digital simulation to be consistent with electron transfer involving different rate constants (on the order of $10^3$–$10^5$ $M^{-1}s^{-1}$) reflecting the varying redox potentials of valence band electrons within one CNT chiral type and within the

distribution of CNTs present in our sample. The lowest observed CNT oxidation potential was between 460 and 645 mV versus Ag/AgCl and, above this potential, the number of transferred electrons increased exponentially with the redox potential of the metal mediator, suggesting that more electrons are accessible to stronger metal oxidants. For example, an oxidant with 645-mV redox potential oxidized CNTs by ~200 electrons per nanotube, while a stronger oxidant (with 1080-mV redox potential) oxidized CNTs by ~2000 electrons per nanotube. This result is attributed to the electronic band structure of CNTs; the stronger oxidant shifts the Fermi level deeper into the CNT valence band. These electron transfer and structural findings are anticipated to benefit the purification of heterogeneous CNT samples, controlled tuning of CNT optical–electronic properties, and development of CNT transistors, charge storage devices, and chemical sensors.

To my grandparents,

Harold and Mary Jane Hastings

&

Richard and Isabelle Fox

**Acknowledgements**

Foremost thanks are owed to my research advisor, Holden Thorp. Holden never failed to support my graduate career, even as his own career spanned from Director of Morehead Planetarium to Chancellor during my five years at UNC (a career move motivated entirely by the pursuit of better seats for basketball games). I have benefited from Holden's advice, friendship, and enthusiasm for research and enjoyed his sense of humor and our science and non-science conversations. Thanks are also due to my Thorp Lab mentors: Patty Ropp, Dom Hull, and Jared Paul, as well as my contemporary lab-mates, for advice and laughs. I especially thank Mary Napier and Steve Feldberg, who were invaluable in straightening out the electrochemistry project, and Tom Meyer, Javier Concepción, and Kyle Brennaman, who have always been available with inorganic and photophysical help. In the AFM world, I am indebted to Dorothy Erie and Ingrid Tessmer for their expertise and guidance. I also thank Noel Kane-Maguire and the rest of the Furman University Chemistry Department who encouraged me to pursue research, Mike Gagné and Brian Hogan for supporting my interest in teaching, and my committee chair Maurice Brookhart.

My parents, Don and Nancy Fox, brother, Adam Fox, and in-laws, Bob and Ann Campbell, are a source of constant support. My extended family members are always interested in my life in Chapel Hill and keep their eyes peeled for carbon nanotube news (especially in connection to "space elevators"). Their encouragement is always appreciated. Most importantly, I thank my husband, Robby, for his invaluable love and support.

## Table of Contents

List of Tables ..... xii

List of Figures ..... xiii

List of Abbreviations and Symbols ..... xvi

**Chapter 1. Introduction to Carbon Nanotubes** ..... 1

1.1 Structure ..... 1

Chirality ..... 1

1.2 Synthesis ..... 3

1.3 Properties ..... 5

Mechanical Properties ..... 5

Optical and Electronic Properties ..... 5

*Electronic Character* ..... 5

*Absorption* ..... 6

*Fluorescence* ..... 8

1.4 Applications ..... 8

Polymer Reinforcement ..... 8

Nanotools ..... 8

Electronics ..... 9

Chemical Sensors ..... 10

Electrode Materials ..... 10

Energy Storage ..... 11
Biological Uses ..... 12
Challenges to Applications ..... 13
*Heterogeneity* ..... 14
*Insolubility* ..... 14
1.5 Suspensions and Solutions ..... 15
Covalent Modification ..... 15
Noncovalent Modification ..... 16
1.6 Towards Structural Homogeneity ..... 16
1.7 Focus of this Dissertation ..... 18
1.8 References ..... 19
**Chapter 2. Characterization of DNA-Wrapped Carbon Nanotubes** ..... 26
2.1 Abstract ..... 26
2.2 Introduction ..... 27
DNA-Wrapped Carbon Nanotubes ..... 27
Applications of DNA-Wrapped Carbon Nanotubes ..... 29
*Electronic Devices* ..... 29
*Advantages in Solution* ..... 30
*Biological Applications* ..... 30
*CNT Sorting and Separation* ..... 31
2.3 Experimental Section ..... 31
Solubilization of Carbon Nanotubes with DNA ..... 31
Absorbance Spectroscopy ..... 34

Determination of CNT Concentration ....34
Determination of DNA Concentration....35
*Method 1* ....35
*Method 2* ....36
Fluorescence Spectroscopy....36
Spectrophotometric Redox Titration....37
Cyclic Voltammetry and Chronoamperometry....37
2.4 Results and Discussion ....38
Solutions of DNA-Wrapped Carbon Nanotubes....38
Concentrations of DNA and Carbon Nanotubes....40
Identification of CNT Types....42
Fluorescence of DNA-Wrapped Carbon Nanotubes....44
Spectrophotometric Redox Titration of DNA-Wrapped Carbon Nanotubes...47
Reversibility of DNA-Wrapped Carbon Nanotube Chemical Oxidation ....50
Addition of Reducing Agents and Base to DNA-Wrapped Carbon Nanotubes....54
Direct Electrochemical Behavior of DNA-Wrapped Carbon Nanotubes....56
2.5 Conclusions....59
2.6 References....61
**Chapter 3. Structure of DNA-Wrapped Carbon Nanotubes**....66
3.1 Abstract....66
3.2 Introduction....67
Structure and Stability of DNA on Carbon Nanotubes....67

Atomic Force Microscopy .....67

3.3 Experimental Section .....69

Atomic Force Microscopy .....69

Imaging of DNA-Wrapped Carbon Nanotubes .....70

Imaging of Surfactant-Suspended Carbon Nanotubes .....70

Quantum Dot Labeling of DNA-Wrapped Carbon Nanotubes .....71

Calculations and Modeling .....72

3.4 Results .....73

Measurements of the DNA-Wrapped Carbon Nanotube Surface Pattern .....73

Effect of the DNA Sequence .....76

Effect of the DNA Length .....78

Quantum Dot Labeling of the Wrapping DNA .....80

Comparison to Surfactant-Suspended Carbon Nanotubes .....84

3.5 Discussion .....88

Location of DNA in DNA-Wrapped Carbon Nanotubes .....88

Modeling of DNA-Wrapped Carbon Nanotube Structure .....89

Surface Pattern on DNA-Wrapped Versus Surfactant-Suspended Carbon Nanotubes .....94

DNA-Wrapped Carbon Nanotube–Quantum Dot Conjugates .....96

3.6 Conclusions .....97

3.7 References .....99

**Chapter 4. Electrochemistry of DNA-Wrapped Carbon Nanotubes** .....101

4.1 Abstract .....101

4.2 Introduction .....102

Cyclic Voltammetry....102

Metal-Mediated Electrochemistry....104

Electron Transfer in Carbon Nanotubes....108

4.3 Experimental Section....111

General....111

Electrodes....111

Cyclic Voltammetry....112

Digital Simulation....112

Size-Exclusion Chromatography....113

Reaction of DNA-Wrapped Carbon Nanotubes with Tris(bipyridine)osmium(III)....114

4.4 Results....115

Metal-Mediated Electrochemical Oxidation of DNA-Wrapped Carbon Nanotubes....115

*Effect of Nanotube and Metal Concentrations*....116

*Effect of Metal Redox Potential*....117

*Effect of Scan Rate*....118

Origin of the Increased Metal Mediator Oxidative Peak Current....121

*Electrochemistry of DNA-Wrapped Carbon Nanotubes after Size-Exclusion Chromatography*....121

*Reaction of DNA-Wrapped Carbon Nanotubes with Tris(bipyridine)osmium(III)*....122

4.5 Discussion....123

Origin of the Increased Metal Mediator Oxidative Peak Current....123

Digital Simulation of Metal Voltammograms in the Absence of DNA-Wrapped Carbon Nanotubes ..... 126

*Heterogeneous Rate Constants* ..... 126

*Metal Mediator Redox Potentials* ..... 126

*Metal Mediator Concentration and Diffusion* ..... 127

*Simulation Mechanism* ..... 127

Digital Simulation of Metal-Mediated Electrochemical Oxidation of DNA-Wrapped Carbon Nanotubes ..... 129

*Diffusion of DNA-Wrapped Carbon Nanotubes* ..... 131

*Concentration of DNA-Wrapped Carbon Nanotubes* ..... 132

*Homogeneous Rate Constants* ..... 132

*Homogeneous Equilibrium Constants* ..... 132

*Simulation Mechanism* ..... 133

*Three Singly Oxidized Populations of Redox-Active Sites* ..... 136

*Effect of Metal Redox Potential* ..... 146

*Comparison to Solution Redox Titration* ..... 148

*Comparison to Polycyclic Aromatic Hydrocarbons and Previous Reports* ..... 149

4.6 Conclusions ..... 151

4.7 References ..... 154

## List of Tables


Table 2.1 Characteristics of Deoxyribooligonucleotide Sequences for CNT–DNA .....33

Table 4.1 Extinction Coefficients, Redox Potentials, and Experimental Cyclic Voltammetry Potentials for Metal Mediators .....107

Table 4.2 Digital Simulation Parameters Describing Cyclic Voltammetry of Metal Mediators in the Absence of CNT–DNA .....129

Table 4.3 Digital Simulation Parameters of an $EC_1'C_2'C_3'$ Mechanism Describing Metal-Mediated CNT–DNA Oxidation .....141

Table 4.4 Extent of CNT–DNA Oxidation during Metal-Mediated Cyclic Voltammetry .....145

## List of Figures


Figure 1.1 Basic structure of single-walled CNTs ..... 2

Figure 1.2 Chirality and naming of CNTs ..... 3

Figure 1.3 Effect of CNT chirality on CNT optical–electronic properties ..... 7

Figure 1.4 Single-walled CNTs for applications ..... 13

Figure 2.1 Model of the interaction between a CNT and ssDNA ..... 29

Figure 2.2 Geometry of an achiral CNT for average molecular weight determination ..... 35

Figure 2.3 Absorbance spectrum of CNTs wrapped with $(GT)_{30}$ oligonucleotide ..... 40

Figure 2.4 Assignment of CNT–DNA electronic transitions to chiral CNT types ..... 44

Figure 2.5 CNT–DNA bandgap fluorescence ..... 46

Figure 2.6 Spectrophotometric titration of CNT–DNA with hexachloroiridate(IV) oxidant ..... 49

Figure 2.7 Reduction of chemically oxidized CNT–DNA over time ..... 52

Figure 2.8 CNT–DNA after cycles of chemical oxidation ..... 54

Figure 2.9 CNT–DNA treated with reducing agents and base ..... 55

Figure 2.10 Direct electrochemistry of CNT–DNA ..... 57

Figure 3.1 Model for the geometry of helically wrapped DNA on a CNT ..... 72

Figure 3.2 Length distribution of CNTs wrapped with $(GT)_{30}$ oligonucleotide ..... 74

Figure 3.3 AFM images of CNTs wrapped with $(GT)_{30}$ oligonucleotide ..... 75

Figure 3.4 AFM height image of CNTs wrapped with $T_{60}$ oligonucleotide ..... 76

Figure 3.5 AFM phase images of CNTs wrapped with $(GT)_{30}$ and $T_{60}$ oligonucleotide ..... 77

Figure 3.6 AFM images of CNTs wrapped with oligonucleotides of varying length ..... 79

Figure 3.7 QD labeling procedure to identify the location of DNA on CNT–DNA ..... 80

Figure 3.8 AFM image of QD-labeled CNT–DNA ....81

Figure 3.9 Selective binding of QDs to the DNA on CNT–DNA....82

Figure 3.10 Distance between QDs on CNT–DNA ....84

Figure 3.11 AFM height image of CNTs suspended by SDS (in the absence of DNA)....85

Figure 3.12 AFM images of the different structures observed for CNT–SDS....86

Figure 3.13 Comparison of CNT–DNA to CNT–SDS....87

Figure 3.14 Simulated AFM images of CNT–DNA models....91

Figure 4.1 The cyclic voltammetry experiment ....104

Figure 4.2 Metal-mediated electrochemistry....106

Figure 4.3 Effect of oxidation and reduction on CNT electronic band structure....109

Figure 4.4 Absorbance spectra of CNT–DNA fractions after size-exclusion chromatography ....114

Figure 4.5 Metal-mediated oxidation of CNT–DNA ....116

Figure 4.6 Concentration dependence of metal-mediated CNT–DNA oxidation....117

Figure 4.7 Dependence of metal-mediated CNT–DNA oxidation on metal redox potential....118

Figure 4.8 Scan rate dependence of metal-mediated CNT–DNA oxidation....120

Figure 4.9 Metal-mediated oxidation of CNT–DNA purified by size-exclusion chromatography ....122

Figure 4.10 Chemical oxidation of CNT–DNA by tris(bipyridine)osmium(III) ....123

Figure 4.11 Catalytic cycle responsible for metal-mediated oxidation of CNT–DNA....125

Figure 4.12 Digital simulation of metal mediator CVs in the absence of CNT–DNA ....128

Figure 4.13 Digital simulation of metal-mediated CNT–DNA oxidation by one versus multiple electrons per CNT....134

Figure 4.14 Attempted digital simulation of metal-mediated CNT–DNA oxidation with an EC′ mechanism ..... 136

Figure 4.15 Digital simulation of CNT–DNA oxidation mediated by different metals with either different ET rate constants or different concentrations of redox sites ..... 139

Figure 4.16 Digital simulation of metal-mediated CNT–DNA oxidation with an $EC_1'C_2'C_3'$ mechanism ..... 140

Figure 4.17 Digital simulation of metal-mediated CNT–DNA oxidation at varying concentrations of CNT–DNA and metal ..... 142

Figure 4.18 Concentration of CNT–DNA electrons available to different metal mediators ..... 144

Figure 4.19 Effect of metal redox potential on the CNT density of electronic states ..... 147

## List of Abbreviations and Symbols

| | |
|---|---|
| 120-mer | deoxyribooligonucleotide of 120-base length |
| 3′ | deoxyribooligonucleotide end containing a terminal hydroxyl group |
| 30-mer | deoxyribooligonucleotide of 30-base length |
| 5′ | deoxyribooligonucleotide end containing a terminal phosphate group |
| 60-mer | deoxyribooligonucleotide of 60-base length |
| $\Delta G$ | change in Gibbs free energy |
| $\varepsilon$ | molar extinction coefficient |
| $\lambda$ | reorganization energy |
| $\lambda_{em}$ | wavelength of emission maximum |
| A | absorbance |
| AFM | atomic force microscopy |
| Ag/AgCl | silver–silver chloride electrode |
| ANOVA | analysis of variance between groups |
| bpy | 2,2′-bipyridine |
| C | chemical electron transfer reaction |
| C′ | catalytic chemical electron transfer reaction |
| $c_n$ | van Hove singularity in the conduction band |
| CNT | carbon nanotube(s) |
| $CNT_n^{m+}$ | oxidized carbon nanotubes |
| CNT–biotin | carbon nanotubes wrapped with biotinylated 60-mers |
| CNT–dithiol | carbon nanotubes wrapped with dithiolated 60-mers |

| | |
|---|---|
| CNT–DNA | DNA-wrapped carbon nanotube(s) |
| CNT–thiol | carbon nanotubes wrapped with monothiolated 60-mers |
| CoMoCAT | a trademarked name for one carbon nanotube synthetic method |
| CV | cyclic voltammetry; cyclic voltammogram |
| D | diffusion coefficient |
| dmb | 4,4′-dimethyl-2,2′-bipyridine |
| $d^n$ | formally containing n electrons in d-type orbitals |
| DNA | deoxyribonucleic acid |
| dsDNA | double-stranded deoxyribonucleic acid |
| E | electrochemical electron transfer reaction |
| $e^-$ | electron |
| $E^0$ | standard potential |
| $E^{0\prime}$ | formal potential |
| $E_{1/2}$ | half-wave redox potential |
| EC′ | classical catalytic mechanism |
| $EC_1'C_2'C_3'$ | classical catalytic mechanism with three CNT populations |
| $E_{nn}$ | an electronic transition |
| ET | electron transfer |
| F | Faraday's constant |
| $Fe^{3+/2+}$ | iron(III/II) redox couple |
| $Fe(bpy)_3^{2+}$ | tris(2,2′-bipyridine)iron(II) |
| $Fe(dmb)_3^{2+}$ | tris(4,4′-dimethyl-2,2′-bipyridine)iron(II) |
| G | guanine nucleobase |

| | |
|---|---|
| g | gravitational field at the surface of Earth |
| Gox | guanine oxidized by loss of one electron |
| $(GT)_{30}$ | 30-mer deoxyribooligonucleotide containing guanine and thymine |
| $(GT)_{60}$ | 60-mer deoxyribooligonucleotide containing guanine and thymine |
| HEPES | 4-(2-hydroxyethyl)-1-piperazineethanesulfonic acid |
| HiPco | a trademarked name for one carbon nanotube synthetic method |
| IR | infrared |
| ITO | tin-doped indium oxide |
| $k_n'$ | catalytic electron transfer rate constant |
| *m* | a unit vector used to describe carbon nanotube structure |
| $M^{2+}$ | metal(II) species |
| $M^{3+}$ | metal(III) species |
| $M^{3+/2+}$ | metal(III/II) redox couple |
| n | in statistics: number of measurements |
| n | in electrochemistry: stoichiometric number of electrons transferred |
| *n* | a unit vector used to describe carbon nanotube structure |
| n-doped | charge doped by negative-type doping |
| NHE | normal hydrogen electrode |
| NMR | nuclear magnetic resonance |
| $Os^{3+/2+}$ | osmium(III/II) redox couple |
| $Os(bpy)_3^{2+}$ | tris(2,2′-bipyridine)osmium(II) |
| $Os(dmb)_3^{2+}$ | tris(4,4′-dimethyl-2,2′-bipyridine)osmium(II) |
| p | a statistical parameter used to determine significance |

| | |
|---|---|
| p-doped | charge doped by positive-type doping |
| pH | negative logarithm of the hydronium ion concentration |
| QD(s) | quantum dot(s) |
| R | the gas constant |
| RT | room temperature |
| $Ru^{3+/2+}$ | ruthenium(III/II) redox couple |
| $Ru(bpy)_3^{2+}$ | tris(2,2′-bipyridine)ruthenium(II) |
| $Ru(bpy)_2(dmb)^{2+}$ | bis(2,2′-bipyridine)mono(4,4′-dimethyl-2,2′-bipyridine)ruthenium(II) |
| $Ru(dmb)_3^{2+}$ | tris(4,4′-dimethyl-2,2′-bipyridine)ruthenium(II) |
| SDS | sodium dodecyl sulfate |
| ssDNA | single-stranded deoxyribonucleic acid |
| T | in equations: temperature |
| T | in DNA sequences: thymine nucleobase |
| $T_{30}$ | 30-mer deoxyribooligonucleotide containing thymine |
| $T_{60}$ | 60-mer deoxyribooligonucleotide containing thymine |
| $T_{120}$ | 120-mer deoxyribooligonucleotide containing thymine |
| UV | ultraviolet |
| $v_n$ | van Hove singularity in the valence band |

# Chapter 1

# Introduction to Carbon Nanotubes

## 1.1 Structure

In 1991, Iijima discovered that the arc-discharge sublimation of graphite produces needle-like carbon formations.[1] These carbon nanotubes (CNTs) are distinct from the other allotropes of carbon (diamond, graphite, and fullerenes) because of their unique one-dimensional shape. The small, ~1-nm diameters of CNTs are dwarfed by their typically considerable lengths, which range from nanometers to centimeters.[2] CNTs exist as multi-walled nanotubes (typically consisting of 2–25 concentric tubes)[1] and single-walled nanotubes (comprising a single tube),[3, 4] with only the latter studied and discussed in the present work. Single-walled CNTs are composed of $sp^2$-hybridized carbon atoms arranged in graphitic hexagons to form the sidewalls of a hollow tube (Figure 1.1A).

**Chirality.** The alignment of these carbon hexagons determines the chirality of a CNT (Figure 1.1B,C). Achiral CNTs have belts of edge-sharing hexagons arranged either parallel or perpendicular to the nanotube axis (Figure 1.2D), while other alignments relative to the tube axis give rise to chiral CNTs (Figure 1.2B).[1, 3] The chirality of an individual CNT is denoted by the unit vector coefficients *n* and *m*, which are used to name each type of CNT; e.g., the (6,4) CNT has $n = 6$ and $m = 4$. The structure and name for each type of nanotube can be determined by visualizing its formation from a seamlessly rolled graphene sheet. For example, to form the chiral (6,4) tube, a graphene sheet is rolled along a vector whose

components are six times and four times the lengths of the unit vectors (Figure 1.2A). In contrast, an achiral CNT is produced by rolling a graphene sheet along either vector 2 or 3 in Figure 1.2C to form (*n*,*n*) or (*n*,0) tubes, respectively. In each case, the length of the rolling vector dictates the circumference and thus the diameter of the resulting nanotube, and its angle relative to the unit vectors determines nanotube chirality. The diameter and chirality of each CNT type are therefore reflected in its (*n*,*m*) name.

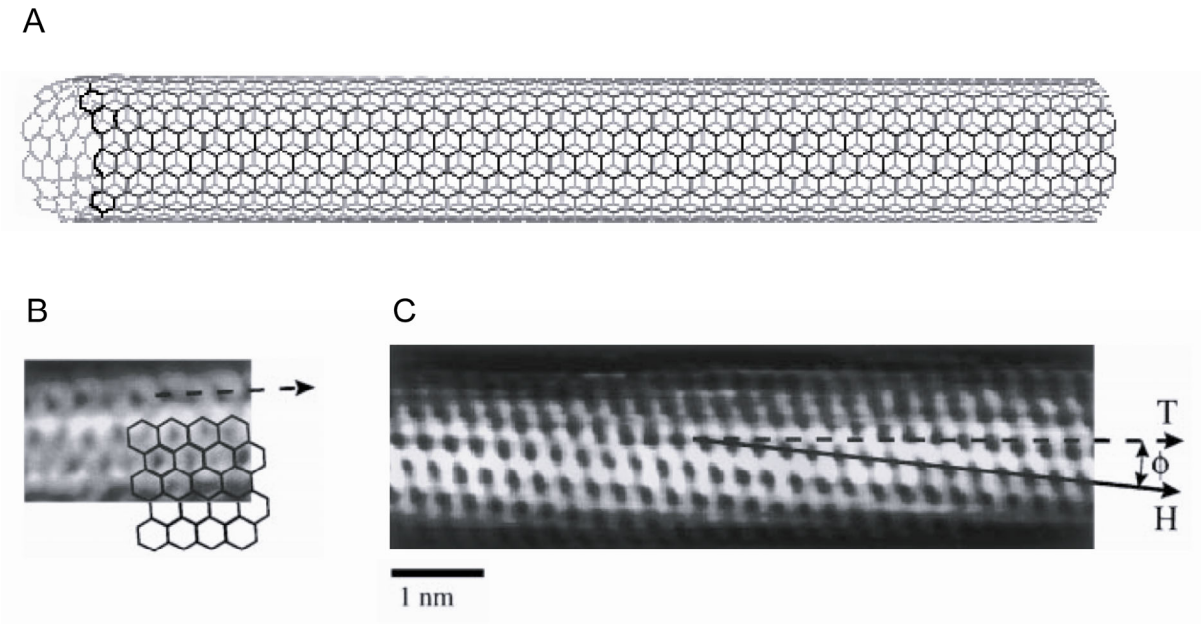


**Figure 1.1 Basic structure of single-walled CNTs.** (A) Arrangement of carbon atoms in a CNT. (B) Achiral and (C) chiral CNTs imaged by scanning tunneling microscopy with atomic resolution. The nanotube axis (T) can be compared to a belt of edge-sharing hexagons (H) to differentiate chiral and achiral CNTs. Adapted from Wildoer, J.W.G. et al.[5]

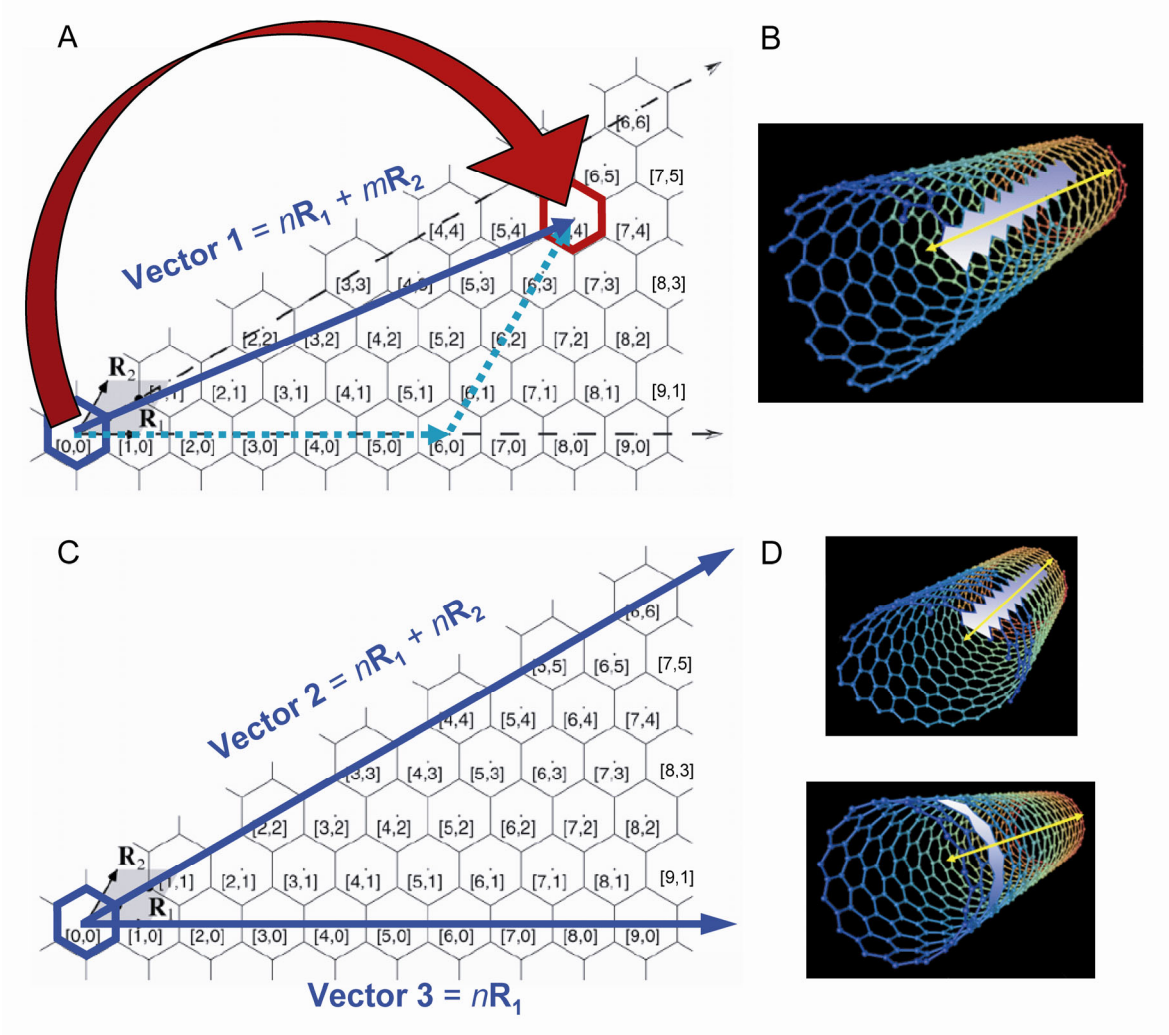


**Figure 1.2 Chirality and naming of CNTs.** Rolling a graphene sheet to form a seamless cylinder results in the formation of (A, B) chiral or (C, D) achiral CNTs. The (6,4) tube is formed by rolling along vector 1, whose component vectors (dashed arrows) are six and four times the length of unit vectors $R_1$ and $R_2$, respectively. Rolling along vector 2 or 3 forms the top or bottom CNTs shown in D, respectively. Yellow arrows show the direction of the CNT axis. Adapted from White, C.T. et al.[6]

## 1.2 Synthesis

CNTs can be produced by electric-arc discharge sublimation of metal-doped graphite electrodes,[3, 4, 7] laser vaporization of metal-doped carbon,[8] and a catalytic technique. The latter method is a scalable process that promotes the decomposition of carbon-containing molecules on unsupported[9] or supported[10] catalyst particles such as Fe, Ni, Co, and Mo. The

CNTs used in the present work were produced by a version of this technique called the CoMoCAT[10, 11] process, which employs a mixture of Co and Mo catalysts on a silica support to promote CO disproportionation (1). At high temperature and CO pressure, carbon monoxide decomposes over activated catalyst sites, resulting in the crystallization of carbon. These nascent CNTs grow as carbon diffuses across their surface, producing a single nanotube on the millisecond timescale.[12]

(1) $2\ CO\ (g) \rightarrow C\ (s) + CO_2\ (g)$

The initial products of single-walled CNT synthesis are contaminated by many different types of impurities, including catalyst particles, the catalyst support, and carbonaceous impurities (amorphous carbon, graphite, multi-walled CNTs, and carbon nanoparticles). Following CNT production via CoMoCAT, treatment with sodium hydroxide removes the silica support and most of the catalyst; subsequent high-temperature oxidation and acid treatment removes carbonaceous impurities and the remaining catalyst particles.[10]

One major shortcoming of current CNT synthetic methods is the heterogeneity of the product, which is a mixture of CNTs that vary in length, diameter, and chirality.[9, 11] The CoMoCAT process produces CNTs that are predominantly semiconducting with a narrow spread of diameters (averaging 0.81 nm) and a relatively narrow ($n$,$m$) distribution.[11] However, no synthetic method has been developed thus far that can produce a homogeneous sample of CNTs.

## 1.3 Properties

**Mechanical Properties.** The Young's modulus is the ratio of tensile stress (force applied to an object per unit area) to tensile strain (the degree to which the material deforms under the applied stress). CNTs have a Young's modulus of ~ 1 TPa, which is greater than that of steel and makes CNTs one of the strongest materials known.[13] The axial strength of CNTs stems from the seamless network of C-to-C bonding, and, owing to the high aspect ratio of a typical CNT, this strength is complemented by great flexibility.

**Optical and Electronic Properties.** The $sp^2$ hybridization of carbon atoms in a CNT creates a highly conjugated aromatic system, and the regular atomic arrangement causes CNT energy levels to form bands. CNTs can therefore be described by a rigid band model with the Fermi level indicating the energy where it is equally probable for the level to be occupied by an electron or vacant.[14] Depending on the structure of the CNT, the valence band (which is nearly filled with electrons) and conduction band (which is not) may meet at the Fermi level as they do in graphene, have moderate separation, or cross through the Fermi level, giving rise to different electronic character for different CNTs.[15]

***Electronic Character.*** The band structure and resulting electronic character of a particular CNT is determined by its chirality. CNTs in which $n = m$ or $n - m = 3p$ (where p is an integer) are metallic with bands crossing the Fermi level, whereas all other CNTs are semiconducting with a bandgap whose energy is inversely dependent on tube diameter.[5] Metallic CNTs behave as molecular wires, with electronic conduction through long single-molecular orbitals in the direction of the nanotube axis[16] and an electron mean free path that can be microns in length.[17] In contrast, disorder causes semiconducting CNTs to behave as a string of isolated quantum dots between which electrons must tunnel.[17]

A depiction of the density of electronic states in a semiconducting CNT is shown in Figure 1.3B,C. The density of states in a metallic CNT is similar except while a semiconducting CNT has a bandgap with zero electronic states, there is a small but finite density of states near the Fermi level of a metallic CNT. For all types of CNTs, the one-dimensional nature of the nanotubes creates a high density of states called a van Hove singularity at the edge of each band.[5] The energies of these van Hove singularities (labeled as $c_n$ or $v_n$ in Figure 1.3B,C) vary with CNT (*n*,*m*) type and can be calculated or measured by scanning tunneling microscopy for any type of CNT.[5, 18]

***Absorption.*** Electronic transitions between van Hove singularities are highly polarized parallel to the CNT axis[19] and occur when CNTs absorb visible and near-infrared light. Absorption from the highest valence ($v_1$) to the lowest conduction ($c_1$) van Hove singularity is designated the $E_{11}$ electronic transition (i.e., $v_1 \rightarrow c_1$), and light absorbed to promote this transition has energy equal to the bandgap of a semiconducting CNT. Since each (*n*,*m*) type of semiconducting CNT has different energy levels, the energies (and corresponding wavelengths) of this electronic transition vary with nanotube chirality. This sensitivity of CNT optical and electronic characteristics to tube chirality is demonstrated by the absorption spectra of two nanotubes possessing the same diameter, yet different (*n*,*m*) types. While the (9,1) and (6,5) CNTs are both semiconducting and have the same diameter, it is evident from the absorbance spectrum of a CNT mixture containing these two CNT types that they have different bandgap energies (Figure 1.3A).

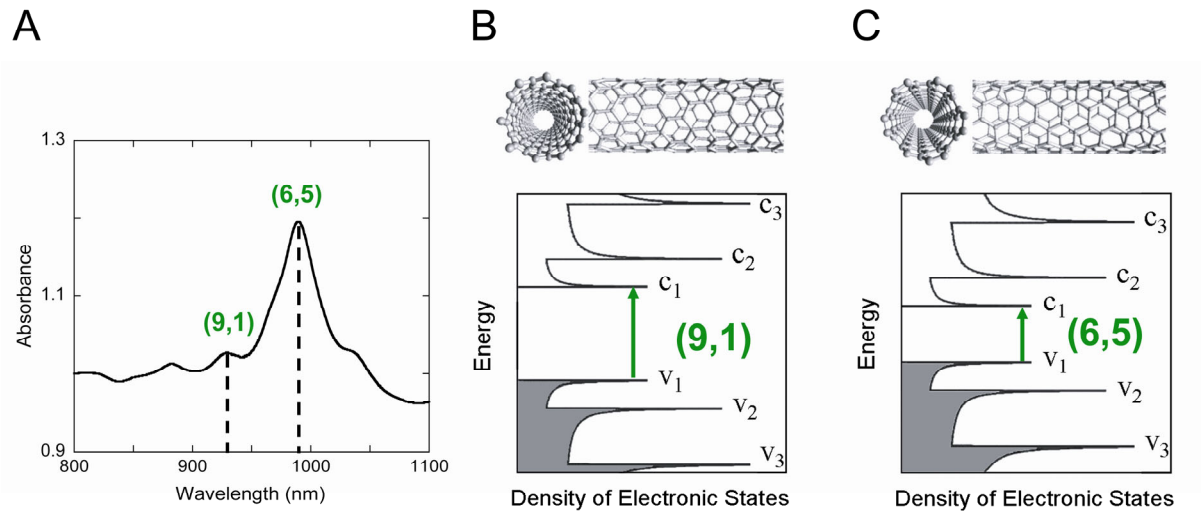


**Figure 1.3 Effect of CNT chirality on CNT optical–electronic properties.** (A) The bandgap absorption ($v_1 \rightarrow c_1$) of (9,1) CNTs occurs at higher energy than that of another semiconducting CNT type with the same tube diameter, (6,5). (B) Structure and density of electronic states diagram for (9,1) CNTs, showing its similar structure yet larger bandgap compared to (C) (6,5) CNTs. Shading indicates states filled with electrons; $c_1$, $v_1$, etc., designate van Hove singularities in the conduction and valence bands. Adapted from Zheng, M. et al.[20]

Other absorption processes such as the $E_{22}$ ($v_2 \rightarrow c_2$) and $E_{33}$ ($v_3 \rightarrow c_3$) electronic transitions are also observed, while selection rules forbid transitions such as $v_2 \rightarrow c_1$. Upon the absorption of light by semiconducting CNTs, electronic excitation creates both bound-excitonic and free-carrier electron–hole pairs,[21] which can diffuse ~50 nm in either direction along the CNT and will be trapped at lower energy states.[22] These electron–hole pairs are mostly strongly bound excitons, but the existence of only one optically allowed excitonic state per matching pair of van Hove singularities (e.g., the $v_1$, $c_1$ pair or the $v_2$, $c_2$ pair) allows the simple free electron picture to serve as a visualization of CNT energy states.[23] The excited states created by light absorption relax through the continuum of states in the conduction band of metallic CNTs, while semiconducting CNTs undergo electron–hole

recombination via nonradiative processes (suggested to involve low-lying triplet and optically forbidden singlet states[24]) or radiative decay (fluorescence).[23]

***Fluorescence.*** Following $v_1 \rightarrow c_1$ absorption, semiconducting CNTs subsequently fluoresce with a similar energy, $c_1 \rightarrow v_1$, across the bandgap.[25] The $v_2 \rightarrow c_2$ and $v_3 \rightarrow c_3$ absorptions also result in bandgap fluorescence, as the promoted electron and its hole decay nonradiatively to the $c_1$ and $v_1$ states, respectively, prior to emission.[23] CNT fluorescence is only observable when the emissive semiconducting CNTs are separated from the quenching metallic CNTs, which can be accomplished by dispersing CNTs in aqueous solution with a surfactant.[25] While the fluorescence quantum yield of ensembles containing both semiconducting and metallic CNTs is < 0.05%, that of individual semiconducting CNTs is ~8%.[26, 27] By comparison to resonance Raman spectra (where the CNT radial breathing mode frequency is directly related to CNT diameter), the emission peaks observed by fluorescence spectroscopy have been assigned to particular CNT types.[28]

## 1.4 Applications

**Polymer Reinforcement.** Carbon fibers are widely used to increase the strength of polymer materials. In this application, CNTs (Figure 1.4A) have advantages over macroscopic fibers because of their large surface area.[29] The high Young's modulus and low density of CNTs make them ideal components of high-strength polymer composites that are also lightweight.

**Nanotools.** The strength, flexibility, and well-defined structure of a single CNT suggest its use as a probe for nanoscopic measurements (Figure 1.4F). Tips for atomic force microscopy (AFM) can be fashioned by attaching a CNT to a conventional AFM tip using

micromanipulation or by growing a CNT directly onto the conventional tip.[30] CNT tips for AFM are robust, can withstand repeated bending at nearly 90°, have been used to reproducibly image the structure of protein complexes at high resolution, and show promise in mapping the functional sites of molecules using chemical force microscopy.[30]

**Electronics.** CNTs are envisioned for future use in electronic circuits, where they may permit easier processing at lower costs and potentially provide a means to miniaturize computer chips beyond the size-barrier of present technology. Functional electronic devices such as field-effect transistors[31-33] have been built using semiconducting CNTs (Figure 1.4E) and demonstrate an advantage over silicon transistors in their high capacity to carry current.[32] These CNT transistors can be assembled into high-gain logic circuits, effectively integrating the transistors onto the same chip.[33] Metallic CNTs also show promise in the construction of circuits, providing a means of transporting electrons over long distances with a higher current density than copper wire. The use of metallic CNTs as interconnect wires has been demonstrated with operation above 1 GHz.[34]

A significant obstacle to CNT-based electronics lies in a lack of techniques to cheaply fabricate devices, including the simple ability to control the position of individual CNTs on surfaces. Advances in this area include use of the Langmuir-Blodgett method to generate highly aligned, densely packed monolayers of CNTs (Figure 1.4B),[35] growth of highly aligned CNTs on insulating substrates,[36] and synthesis of vertically aligned "forests" of CNTs on silicon[37] (Figure 1.4C) or conducting substrates.[38] Techniques have also been developed for the assembly of many single-nanotube devices on a single chip, such as the use of radio frequency dielectrophoresis to maneuver CNTs into the position of bridging two electrodes.[39]

Another current investigation into the use of CNTs for electronic applications is in the production of conductive films and coatings. Metallic CNTs are preferable to semiconducting CNTs for this application due to their higher electrical conductivity and lower sensitivity to chemical doping.[40, 41] Films made with predominately metallic CNTs have demonstrated improved optical properties, including transmittance that can be tuned by varying the diameter of the component CNTs (Figure 1.4D), and higher conductivity compared to films of mixed semiconductor and metallic CNTs.[42] Films of CNTs can be produced with high mechanical strength, flexibility, conductivity, and transparency. These features, especially the superior flexibility compared to current materials, make CNT films a potential substitute for solar cell substrates[43] or the electrodes of organic light-emitting diodes.[44, 45]

**Chemical Sensors.** CNTs can act as sensors for a variety of small molecules because of their high sensitivity to environment. This sensitivity exists because the association of small molecules (such as the electron-donating $NH_3$ and electron-withdrawing $NO_2$ gases) with the CNT surface can cause negative (n-) or positive (p-) charge doping of CNT electronic bands. Charge doping drastically increases the charge carrier density of semiconducting nanotubes due to the large density of states near the edges of the valence and conduction bands (and has a lesser impact on metallic CNTs due to the finite density of states present near their Fermi level). This change in carrier density upon chemical doping induces substantial changes in CNT electrical resistance that can be used to detect the presence of the dopant molecule.[46]

**Electrode Materials.** Electrodes based on single-walled CNTs have been used extensively for analysis and also demonstrate a useful platform for electrochemical

biosensors.[47, 48] The CNT ends have been compared to the edge planes of highly oriented pyrolytic graphite (HOPG), while the CNT sidewalls are akin to the basal planes of HOPG with the addition of oxide modifications that enhance their performance as an electrode surface.[49] Typically, CNT electrodes are made by modifying a substrate electrode such as glassy carbon with CNTs. However, other electrode constructions have been demonstrated: single-nanotube electrodes that may be useful in scanning electrochemical microscopy,[50] ultramicroelectrodes formed on insulating surfaces without the interference of a substrate electrode,[51] and arrays of vertically aligned CNTs that act as molecular wires to investigate biological molecules attached to the nanotube ends.[47]

CNT-based electrodes have been reported to reduce the overpotential needed for the reduction or oxidation of many species and to enhance the electrode robustness, limits of detection, reversibility, and sensitivity.[49] The improvements observed in some early reports of enhanced electrode properties have been attributed to the presence of metal catalyst impurities rather than the CNT itself.[52] However, studies of single, pristine CNTs (with no interference by metal particle impurities) demonstrate that the CNT sidewalls can support fast rates of electron transfer with outer-sphere redox couples.[53]

**Energy Storage.** CNT electrodes have large surface area and little separation from the counter-charge produced by electrolyte in solution, suggesting their use as supercapacitors,[54] which require only a low applied potential to induce the charge injection that results in energy storage.[54] CNT electrodes may prove useful in lithium batteries, which reversibly inject lithium cations into the carbon electrode material.[55] However, current devices using CNTs suffer in performance compared to other carbon-based electrodes, in part due to a large irreversible trapping of ions upon the first charging cycle.[54, 55]

CNTs have also been proposed as a solid-state storage medium for hydrogen gas. Hydrogen physisorption and chemisorption are possible along CNT sidewalls, within pores created by the contact of many CNTs in bundles, and inside the nanotube cavities. Measurement of the hydrogen storage capacity of CNTs has so far yielded conflicting results, due to differences in CNT synthesis and purification and in the methodologies used to measure hydrogen uptake,[55] but the appeal of hydrogen as an energy source has maintained an active investigation into hydrogen storage by CNTs.

**Biological Uses.** The ~1-nm diameter of CNTs suggests interfacing nanotubes with biological molecules. Cells can internalize CNTs via endocytosis,[56] with some CNT suspensions exhibiting little cytotoxicity at useful CNT concentrations.[57] However, toxicity data vary widely for CNTs with different surface modifications, suggesting that careful design of CNT surface functionalization is necessary for compatibility in a biological environment. CNTs noncovalently associated with single-stranded DNA (ssDNA) are one type of functionalized CNT (discussed further in Chapter 2) that may prove useful for biological applications.

CNTs have been employed in bio-sensing[58] and biological imaging (e.g., of cell surface receptors,[59] within cells,[60] and within living Drosophila larvae[61]). These sensing and imaging applications take advantage of CNT fluorescence, which occurs in a spectral window compatible with biological tissue. CNTs have also been investigated as vectors for drug delivery. They can be tethered through cleavable linkages to cargo that is not normally taken up by cells, such as anticancer pro-drugs[62] or short interfering RNA (siRNA).[57] These modified CNTs can be internalized into cells and the linkages cleaved to release the cargo molecules. This scheme of transporting cargo has been successfully demonstrated by the

effective gene silencing induced by CNT-delivered siRNA and the cytotoxicity of CNT-delivered cancer drugs.

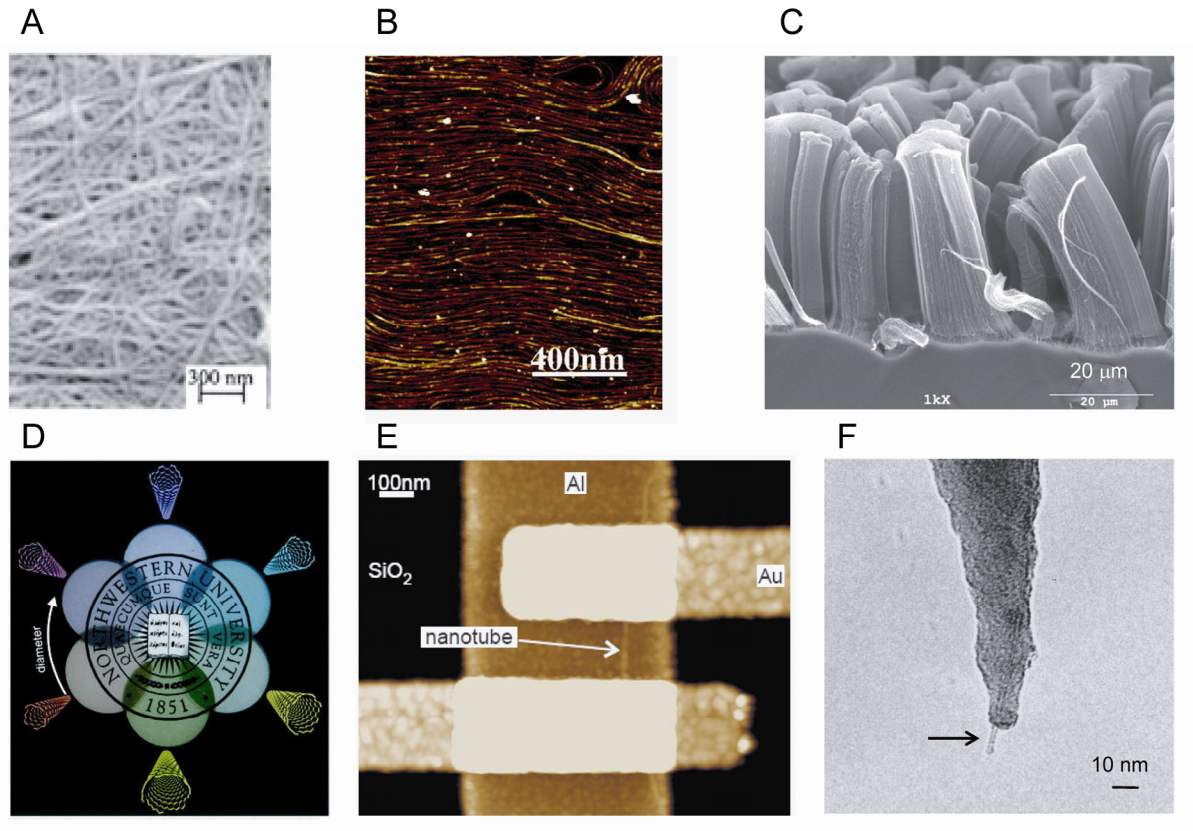


**Figure 1.4 Single-walled CNTs for applications.** (A) Scanning electron micrograph of a CNT film made with oleum.[63] (B) Atomic force microscopy height image of Langmuir-Blodgett monolayers, demonstrating highly aligned CNTs.[35] (C) Scanning electron micrograph of vertical pillars grown on silicon, containing many aligned single-walled CNTs.[37] (D) Photograph of colored, semitransparent, conductive CNT films made on polyethylene terephthalate for use in solar cells or organic light-emitting diodes.[42] (E) Atomic force microscopy height image of a transistor made from a single semiconducting CNT.[33] (F) Transmission electron micrograph of a single nanotube protruding from a support, to be employed as a tip for atomic force microscopy.[30] Adapted from Sreekumar, T.V. et al.; Li, X. et al.; Zhang, L. et al.; Green, A.A. et al.; Bachtold, A. et al.; and Hafner, J.H. et al.

**Challenges to Applications.** Some obstacles to the practical application of CNTs are discussed above, including the need for efficient methods to assemble CNTs for electronics.

This and other technological hurdles are important issues to address for the useful application of CNTs. There are also challenges stemming from the heterogeneity of currently available CNTs and their resistance to solubilization.

***Heterogeneity.*** Nanotubes are synthesized as a heterogeneous population of lengths, diameters, and chiralities. Each of these attributes affects CNT use in applications, with perhaps the most significant barrier to CNT applications being the chiral heterogeneity of commercially available CNTs. This heterogeneity is problematic because each CNT chiral type has different electronic characteristics. Selective use of either metallic or semiconducting tubes is essential to the fabrication of electronic devices, chemical sensors, and conducting nanotools, polymer composites, and films. Therefore, a cost-effective means to generate CNT samples with electronic and chiral homogeneity is a current focus of intense research. Progress in this area is described in Section 1.6 below.

***Insolubility.*** Another significant obstacle to utilizing CNTs in a variety of applications is their insolubility. Due to strong hydrophobic interactions between tubes, CNTs are produced in the form of bundles or ropes composed of many aligned nanotubes. These bundles obviously pose a problem for any application relying upon the isolation of individual CNTs. Bundle formation also reduces the surface area of CNTs (leading, for instance, to poorer performance in polymer composites and films[29, 64]) and perturbs the optical–electronic properties of the constituent CNTs: CNT absorption is significantly broadened,[25] fluorescence is quenched,[25] and conduction through CNT films is decreased.[40, 64] Bundles cause inherent CNT insolubility in most organic solvents and in aqueous solutions. To overcome this insolubility and the attendant detrimental effects on CNT

properties, CNTs can be separated from each other through functionalization (discussed in Section 1.5 below).

### 1.5 Suspensions and Solutions

CNTs can be dispersed in certain solvents without modification; however, the concentration of dispersed CNTs is low and dispersion can be short-lived.[65] Therefore, interactions with a variety of molecules have been utilized to debundle and suspend CNTs in solvents via both covalent and noncovalent strategies.

**Covalent Modification.** Many reactions have been reported to induce the dispersion of CNTs (usually in the form of suspended CNT bundles) through covalent modification. These schemes often target the ends of CNTs and defect sites on the CNT sidewalls, which have a partial loss of conjugation and therefore enhanced reactivity. These sites can be treated with sulfuric and nitric acids or with sulfuric acid and hydrogen peroxide to introduce oxygenated functional groups, including carboxylic acids, quinones, and esters.[66] The oxygen-containing functionalities can be readily exploited to further modify the CNTs with a variety of moieties,[66] including groups that confer water solubility.[67] More extensive covalent modification strategies target the CNT sidewalls. Smaller-diameter CNTs are more reactive to this sidewall chemistry than larger-diameter CNTs because their higher curvature increases strain and well-positions orbitals for functionalization.[68] Useful reactions include fluorination, alkylation, diazotization, ozonation, radical and nucleophilic addition, hydrogenation, and protonation by superacids.[66, 69, 70] These types of reactions can lead to both the incorporation of useful functional groups and the dispersion of CNTs in various solvents. However, one significant drawback of the covalent functionalization of CNTs is

that disruption of the $sp^2$-hybridized carbon network by covalent bonding to functional groups deteriorates both the structural quality[71] and electronic communication[70, 72] of the CNT.

**Noncovalent Modification.** Interactions such as the adsorption of small aromatic molecules to the CNT sidewalls or wrapping of CNTs by organic polymers have proved useful to suspend CNTs in organic solvents.[73, 74] In aqueous media, a common method to suspend CNTs is to coat the surface of individual tubes or small bundles with a surfactant. The resulting CNT–surfactant material is made water-soluble by the hydrophilic surfactant headgroups, while the hydrophobic tails bind to the CNT surface in random orientations, hemispherical micelles, or an encapsulating cylindrical micelle.[75] The strength of this interaction can be increased by selecting surfactants (e.g., Triton X and sodium dodecylbenzenesulfonate) with planar aromatic components that are capable of π-stacking on the CNT surface. Amphiphilic polymers can also solubilize CNTs in water, usually binding to the CNT surface in a manner that involves π-stacking.[76] One highly useful polymer for dissolving individual CNTs in aqueous solution is ssDNA. Noncovalent interactions between the ssDNA nucleobases and the CNT surface result in a stable CNT–DNA hybrid material, which has promise in chemical sensing, electronic devices, and biological applications such as *in vivo* transport, biosensors, and biological imaging. Chapter 2 contains further discussion of the applications for CNT–DNA.

## 1.6 Towards Structural Homogeneity

The separation of CNTs by length has largely been accomplished using traditional analytical separation techniques, such as capillary electrophoresis,[77] gel electrophoresis,[78]

and size-exclusion chromatography.[79] On a larger scale, extractions to obtain CNTs with narrowed length distributions relative to the starting material may prove useful.[80] For separation of CNTs according to diameter, angstrom-level resolution can be attained by ultracentrifugation of surfactant-suspended CNTs through density gradients.[42]

Metallic and semiconducting CNTs can be separated through many promising methods. Alternating current dielectrophoresis of a surfactant-suspended CNT mixture takes advantage of the different CNT dipole moments induced by an electric field to selectively deposit metallic CNTs onto an electrode.[81] Ion exchange chromatography of CNTs wrapped with ssDNA can separate CNTs according to electronic type and even produce solutions enriched in a single (*n,m*) type.[20, 82] On a larger scale, one strategy is to suspend CNTs with surfactants or ammines that selectively interact with CNTs of a particular electronic character or chiral type and then isolate the selected CNTs by precipitation.[83, 84] Since CNTs of different electronic structure exhibit different reactivities,[85] chemical reactions such as phenolic functionalization via diazonium salt reagents have been used to selectively react metallic CNTs, which can later be separated from unreacted semiconducting CNTs due to a difference in density.[86] Variation in CNT density can also be exploited for noncovalently functionalized CNTs, such as those suspended with a surfactant that will organize differently on the nanotube surface depending on the structure and electronic character of each CNT.[87] Ultracentrifugation of these surfactant-suspended CNTs through density gradients allows for separation and facile isolation of predominately metallic or semiconducting CNTs, CNTs of a single diameter, and samples predominated by one specific chiral type.[87]

## 1.7 Focus of this Dissertation

Solubilization of individual CNTs is an important step to avoid the detriments of CNT bundles and to enable separation and purification of CNTs according to length, diameter, and chiral type for use in applications. However, many CNT suspensions contain significant quantities of bundles, offer only temporary dispersion, yield low concentrations of dispersed material, and/or damage the structure and deteriorate the electronic characteristics of CNTs.

An effective way to noncovalently dissolve CNTs in aqueous solution is to wrap the nanotubes with ssDNA.[88] These CNT–DNA solutions contain individually solubilized CNTs with very low bundle content, preserve CNT electronic properties, and offer long-term, high-concentration solubility. CNT–DNA solutions are a useful means of studying the optical–electronic properties of individual CNTs,[89-92] may improve electronic devices and sensors, and offer a valuable interface with biological systems for drug delivery, sensing, and imaging applications. CNT–DNA have also been employed for the chromatographic separation of CNTs according to length, diameter, and chiral type,[20, 79, 82, 93] offering a potential route towards homogeneous samples of CNTs. **The present work is an investigation of these DNA-wrapped carbon nanotubes, with the goal of elucidating both the DNA wrapping structure and nanotube solution electrochemistry.** A better understanding of CNT–DNA is expected to benefit the application of this unique nanomaterial to electronic devices, electrodes, biological imaging, and sensors.

## 1.8 References


1. Iijima, S. *Nature* **1991**, *354*, 56-58.

2. Hong, B. H.; Lee, J. Y.; Beetz, T.; Zhu, Y.; Kim, P.; Kim, K. S. *J. Am. Chem. Soc.* **2005**, *127*, 15336-15337.

3. Iijima, S.; Ichihashi, T. *Nature* **1993**, *363*, 603-605.

4. Bethune, D. S.; Kiang, C. H.; Vries, M. S. d.; Gorman, G.; Savoy, R.; Vazquez, J.; Beyers, R. *Nature* **1993**, *363*, 605-607.

5. Wildoer, J. W. G.; Venema, L. C.; Rinzler, A. G.; Smalley, R. E.; Dekker, C. *Nature* **1998**, *391*, 59-62.

6. White, C. T.; Mintmire, J. W. *J. Phys. Chem. B* **2005**, *109*, 52-65.

7. Journet, C.; Maser, W. K.; Bernier, P.; Loiseau, A.; de la Chapelle, M. L.; Lefrant, S.; Deniard, R.; Lee, R.; Fischer, J. E. *Nature* **1997**, *388*, 756-758.

8. Thess, A.; Nikolaev, P.; Dai, H. J.; Petit, P.; Robert, J.; Xu, C. H.; Lee, Y. H.; Kim, S. G.; Rinzler, A. G.; Colbert, D. T.; Scuseria, G. E.; Tomanek, D.; Fischer, R. E.; Smalley, R. E. *Science* **1996**, *273*, 483-487.

9. Nikolaev, P.; Bronikowski, M. J.; Bradley, R. K.; Rohmund, F.; Colbert, D. T.; Smith, K. A.; Smalley, R. E. *Chem. Phys. Lett.* **1999**, *313*, 91-97.

10. Resasco, D. E.; Alvarez, W. E.; Pompeo, F.; Balzano, L.; Herrera, J. E.; Kitiyanan, B.; Borgna, A. *J. Nanopart. Res.* **2002**, *4*, 131-136.

11. Bachilo, S. M.; Balzano, L.; Herrera, J. E.; Pompeo, F.; Resasco, D. E.; Weisman, R. B. *J. Am. Chem. Soc.* **2003**, *125*, 11186-11187.

12. Monzon, A.; Lolli, G.; Cosma, S.; Mohamed, S. B.; Resasco, D. E. *J. Nanosci. Nanotechnol.* **2008**, *8*, 6141-6152.

13. Treacy, M. M. J.; Ebbesen, T. W.; Gibson, J. M. *Nature* **1996**, *381*, 678-680.

14. Kavan, L.; Frank, O.; Green, A. A.; Hersam, M. C.; Koltai, J.; Zolyomi, V.; Kurti, J.; Dunsch, L. *J. Phys. Chem. C* **2008**, *112*, 14179-14187.

15. Colbert, D. T.; Smalley, R. E. *Trends Biotechnol.* **1999**, *17*, 46-50.

16. Tans, S. J.; Devoret, M. H.; Dai, H.; Thess, A.; Smalley, R. E.; Geerligs, L. J.; Dekker, C. *Nature* **1997**, *386*, 474-477.

17. McEuen, P. L.; Bockrath, M.; Cobden, D. H.; Yoon, Y.-G.; Louis, S. G. *Phys. Rev. Lett.* **1999**, *83*, 5098-5101.

18. Odom, T. W.; Huang, J.-L.; Kim, P.; Lieber, C. M. *Nature* **1998**, *391*, 62-64.

19. Bozovic, I.; Bozovic, N.; Damnjanovic, M. *Phys. Rev. B* **2000**, *62*, 6971-6974.

20. Zheng, M.; Semke, E. D. *J. Am. Chem. Soc.* **2007**, *129*, 6084-6085.

21. Mohite, A.; Lin, J.-T.; Sumanasekera, G.; Alphenaar, B. W. *Nano Lett.* **2006**, *6*, 1369-1373.

22. Cognet, L.; Tsyboulski, D. A.; Rocha, J.-D. R.; Doyle, C. D.; Tour, J. M.; Weisman, R. B. *Science* **2007**, *316*, 1465-1468.

23. Carlson, L. J.; Krauss, T. D. *Acc. Chem. Res.* **2008**, *41*, 235-243.

24. Tretiak, S. *Nano Lett.* **2007**, *7*, 2201-2206.

25. O'Connell, M. J.; Bachilo, S. M.; Huffman, C. B.; Moore, V. C.; Strano, M. S.; Haroz, E. H.; Rialon, K. L.; Boul, P. J.; Noon, W. H.; Kittrell, C.; Ma, J.; Hauge, R. H.; Weisman, R. B.; Smalley, R. E. *Science* **2002**, *297*, 593-596.

26. Carlson, L. J.; Maccagnano, S. E.; Zheng, M.; Silcox, J.; Krauss, T. D. *Nano Lett.* **2007**, *7*, 3698-3703.

27. Tsyboulski, D. A.; Rocha, J.-D. R.; Bachillo, S. M.; Cognet, L.; Weisman, R. B. *Nano Lett.* **2007**, *7*, 3080-3085.

28. Bachilo, S. M.; Strano, M. S.; Kittrell, C.; Hauge, R. H.; Smalley, R. E.; Weisman, R. B. *Science* **2002**, *298*, 2361-2366.

29. Cadek, M.; Coleman, J. N.; Ryan, K. P.; Nicolosi, V.; Bister, G.; Fonseca, A.; Nagy, J. B.; Szostak, K.; Beguin, F.; Blau, W. J. *Nano Lett.* **2004**, *4*, 353-356.

30. Hafner, J. H.; Cheung, C.-L.; Woolley, A. T.; Lieber, C. M. *Prog. Biophys. Mol. Biol.* **2001**, *77*, 73-110.

31. Tans, S. J.; Verschueren, A. R. M.; Dekker, C. *Nature* **1998**, *393*, 49-52.

32. Durkop, T.; Getty, S. A.; Cobas, E.; Fuhrer, M. S. *Nano Lett.* **2004**, *4*, 35-39.

33. Bachtold, A.; Hadley, P.; Nakanishi, T.; Dekker, C. *Science* **2001**, *294*, 1317-1320.

34. Close, G. F.; Yasuda, S.; Paul, B.; Fujita, S.; Wong, H.-S. P. *Nano Lett.* **2008**, *8*, 706-709.

35. Li, X.; Zhang, L.; Wang, X.; Shimoyama, I.; Sun, X.; Seo, W.-S.; Dai, H. *J. Am. Chem. Soc.* **2007**, *129*, 4890-4891.

36. Ryu, K.; Badmaev, A.; Gomez, L.; Ishikawa, F.; Lei, B.; Zhou, C. *J. Am. Chem. Soc.* **2007**, *129*, 10104-10105.

37. Zhang, L.; Resasco, D. E. *Langmuir* **2009**, *A.S.A.P.*, DOI: 10.1021/la8040264.

38. Hiraoka, T.; Yamada, T.; Hata, K.; Futaba, D. N.; Kurachi, H.; Uemura, S.; Yumura, M.; Iijima, S. *J. Am. Chem. Soc.* **2006**, *128*, 13338-13339.

39. Vijayaraghavan, A.; Blatt, S.; Weissenberger, D.; Oron-Carl, M.; Hennrich, F.; Gerthsen, D.; Hahn, H.; Krupke, R. *Nano Lett.* **2007**, *7*, 1556-1560.

40. Stadermann, M.; Papadakis, S. J.; Falvo, M. R.; Novak, J.; Snow, E.; Fu, Q.; Liu, J.; Fridman, Y.; Boland, J. J.; Superfine, R.; Washburn, S. *Phys. Rev. B* **2004**, *69*, 201402/1-3.

41. Miyata, Y.; Yanagi, K.; Maniwa, Y.; Kataura, H. *J. Phys. Chem. C* **2008**, *112*, 3591-3596.

42. Green, A. A.; Hersam, M. C. *Nano Lett.* **2008**, *8*, 1417-1422.

43. Shim, B. S.; Tang, Z.; Morabito, M. P.; Agarwal, A.; Hong, H.; Kotov, N. A. *Chem. Mater.* **2007**, *19*, 5467-5474.

44. Li, J.; Hu, L.; Wang, L.; Zhou, Y.; Gruner, G.; Marks, T. J. *Nano Lett.* **2006**, *6*, 2472-2477.

45. Zhang, D.; Ryu, K.; Liu, X.; Polikarpov, E.; Ly, J.; Tompson, M. E.; Zhou, C. *Nano Lett.* **2006**, *6*, 1880-1886.

46. Kauffman, D. R.; Star, A. *J. Phys. Chem. C* **2008**, *112*, 4430-4434.

47. Gooding, J. J.; Wibowo, R.; Liu, J.; Yang, W.; Losic, D.; Orbons, S.; Mearns, F. J.; Shapter, J. G.; Hibbert, D. B. *J. Am. Chem. Soc.* **2003**, *125*, 9006-9007.

48. Wang, J. *Electroanal.* **2005**, *17*, 7-14.

49. Gooding, J. J. *Electrochim. Acta* **2005**, *50*, 3049-3060.

50. Campbell, J. K.; Sun, L.; Crooks, R. M. *J. Am. Chem. Soc.* **1999**, *121*, 3779-3780.

51. Dumitrescu, I.; Unwin, P. R.; Wilson, N. R.; Macpherson, J. V. *Anal. Chem.* **2008**, *80*, 3598-3605.

52. Kruusma, J.; Mould, N.; Jurkschat, K.; Crossley, A.; Banks, C. E. *Electrochem. Commun.* **2007**, *9*, 2330-2333.

53. Heller, I.; Kong, J.; Heering, H. A.; Williams, K. A.; Lemay, S. G.; Dekker, C. *Nano Lett.* **2005**, *5*, 137-142.

54. Baughman, R. H.; Zakhidov, A. A.; de Heer, W. A. *Science* **2002**, *297*, 787-792.

55. Liu, C.; Cheng, H.-M. *J. Phys. D.: Appl. Phys.* **2005**, *38*, R231-R252.

56. Kam, N. W. S.; Jessop, T. C.; Wender, P. A.; Dai, H. *J. Am. Chem. Soc.* **2004**, *126*, 6850-6851.

57. Liu, Z.; Winters, M.; Holodniy, M.; Dai, H. *Angew. Chem. Int. Ed.* **2007**, *46*, 2023-2027.

58. Barone, P.; Baik, S.; Heller, D. A.; Strano, M. S. *Nat. Mater.* **2005**, *4*, 86-92.

59. Welsher, K.; Liu, Z.; Daranciang, D.; Dai, H. *Nano Lett.* **2008**, *8*, 586-590.

60. Cherukuri, P.; Bachillo, S. M.; Litovsky, S. H.; Weisman, R. B. *J. Am. Chem. Soc.* **2004**, *126*, 15638-15639.

61. Leeuw, T. K.; Reith, R. M.; Simonette, R. A.; Harden, M. E.; Cherukuri, P.; Tsyboulski, D. A.; Beckingham, K. M.; Weisman, R. B. *Nano Lett.* **2007**, *7*, 2650-2654.

62. Feazell, R. P.; Nakayama-Ratchford, N.; Dai, H.; Lippard, S. J. *J. Am. Chem. Soc.* **2007**, *129*, 8438-8439.

63. Sreekumar, T. V.; Liu, T.; Kumar, S.; Ericson, L. M.; Hauge, R. H.; Smalley, R. E. *Chem. Mater.* **2003**, *15*, 175-178.

64. Yu, A.; Bekyarova, E.; Itkis, M. E.; Fakhrutdinov, D.; Webster, R.; Haddon, R. C. *J. Am. Chem. Soc.* **2006**, *128*, 9902-9908.

65. Giordani, S.; Bergin, S. D.; Nicolosi, V.; Lebedkin, S.; Kappes, M. M.; Blau, W. J.; Coleman, J. N. *J. Phys. Chem. B* **2006**, *110*, 15708-15718.

66. Bahr, J. L.; Tour, J. M. *J. Mater. Chem.* **2002**, *12*, 1952-1958.

67. Pompeo, F.; Resasco, D. E. *Nano Lett.* **2002**, *2*, 369-373.

68. Zheng, G.; Wang, Z.; Irle, S.; Morokuma, K. *J. Am. Chem. Soc.* **2006**, *128*, 15117-15126.

69. Davis, V. A.; Ericson, L. M.; Parra-Vasquez, N. G.; Fan, H.; Wang, Y.; Prieto, V.; Longoria, J. A.; Ramesh, S.; Saini, R. K.; Kittrell, C.; Billups, W. E.; Adams, W. W.; Hauge, R. H.; Smalley, R. E.; Pasquali, M. *Macromolecules* **2004**, *37*, 154-160.

70. Banerjee, S.; Hemraj-Benny, T.; Wong, S. S. *Adv. Mater.* **2005**, *17*, 17-29.

71. Garg, A.; Sinnott, S. B. *Chem. Phys. Lett.* **1998**, *295*, 273-278.

72. Bahr, J. L.; Yang, J.; Kosynkin, D. V.; Bronikowski, M. J.; Smalley, R. E.; Tour, J. M. *J. Am. Chem. Soc.* **2001**, *123*, 6536-6542.

73. Debnath, S.; Cheng, Q.; Hedderman, T. G.; Byrne, H. J. *J. Phys. Chem. C* **2008**, *112*, 10418-10422.

74. Hwang, J.-Y.; Nish, A.; Doig, J.; Douven, S.; Chen, C.-W.; Chen, L.-C.; Nicholas, R. J. *J. Am. Chem. Soc.* **2008**, *130*, 3543-3553.

75. Valcarcel, M.; Cardenas, S.; Simonet, B. M. *Anal. Chem.* **2007**, *79*, 4788-4797.

76. O'Connell, M. J.; Boul, P.; Ericson, L. M.; Huffman, C.; Wang, Y.; Haroz, E.; Kuper, C.; Tour, J.; Ausman, K. D.; Smalley, R. E. *Chem. Phys. Lett.* **2001**, *342*, 265-271.

77. Doom, S. K.; Fields, R. E.; Hu, H.; Hamon, M. A.; Haddon, R. C.; Selegue, J. P.; Majidi, V. *J. Am. Chem. Soc.* **2002**, *124*, 3169-3174.

78. Heller, D. A.; Mayrhofer, R. M.; Baik, S.; Grinkova, Y. V.; Usrey, M.; Strano, M. S. *J. Am. Chem. Soc.* **2004**, *126*, 14567-14573.

79. Huang, X.; McLean, R. S.; Zheng, M. *Anal. Chem.* **2005**, *77*, 6225-6228.

80. Ziegler, K. J.; Schmidt, D. J.; Rauwald, U.; Shah, K. N.; Flor, E. L.; Hauge, R. H.; Smalley, R. E. *Nano Lett.* **2005**, *5*, 2355-2359.

81. Krupke, R.; Hennrich, F.; Lohnysen, H.; Kappes, M. M. *Science* **2003**, *301*, 344-347.

82. Zheng, M.; Jagota, A.; Strano, M. S.; Santos, A. P.; Barone, P.; Chou, S. G.; Diner, B. A.; Dresselhaus, M. S.; McLean, R. S.; Onoa, G. B.; Samsonidze, G. G.; Semke, E. D.; Usrey, M.; Walls, D. J. *Science* **2003**, *302*, 1545-1548.

83. McDonald, T. J.; Engtrakul, C.; Jones, M.; Rumbles, G.; Heben, M. J. *J. Phys. Chem. B* **2006**, *110*, 25339-25346.

84. Chattopadhyay, D.; Galeska, I.; Papadimitrakopoulos, F. *J. Am. Chem. Soc.* **2003**, *125*, 3370-3375.

85. Strano, M. S.; Dyke, C. A.; Usrey, M.; Barone, P. W.; Allen, M. J.; Shan, H.; Kittrell, C.; Hauge, R. H.; Tour, J. M.; Smalley, R. E. *Science* **2003**, *301*, 1519-1522.

86. Kim, W.-J.; Nair, N.; Lee, C. Y.; Strano, M. S. *J. Phys. Chem. C* **2008**, *112*, 7326-7331.

87. Arnold, M. S.; Green, A. A.; Hulvat, J. F.; Stupp, S. I.; Hersam, M. C. *Nat. Nanotechnol.* **2006**, *1*, 60-65.

88. Zheng, M.; Jagota, A.; Semke, E. D.; Diner, B. A.; McLean, R. S.; Lustig, S. R.; Richardson, R. E.; Tassi, N. G. *Nat. Mater.* **2003**, *2*, 338-342.

89. Zheng, M.; Diner, B. A. *J. Am. Chem. Soc.* **2004**, *126*, 15490-15494.

90. Napier, M. E.; Hull, D. O.; Thorp, H. H. *J. Am. Chem. Soc.* **2005**, *127*, 11952-11953.

91. Chou, S. G.; Ribeiro, H. B.; Barros, E. B.; Santos, A. P.; Nezich, D.; Samsonidze, G. G.; Fantini, C.; Pimenta, M. A.; Jorio, A.; Filho, F. P.; Dresselhaus, M. S.; Dresselhaus, G.; Saito, R.; Zheng, M.; Onoa, G. B.; Semke, E. D.; Swan, A. K.; Unlu, M. S.; Goldberg, B. B. *Chem. Phys. Lett.* **2004**, *397*, 296-301.

92. Chou, S. G.; DeCamp, M. F.; Jiang, J.; Samsonidze, G. G.; Barros, E. B.; Plentz, F.; Jorio, A.; Zheng, M.; Onoa, G. B.; Semke, E. D.; Tokmakoff, A.; Saito, R.; Dresselhaus, G.; Dresselhaus, M. S. *Phys. Rev. B* **2005**, *72*, 195415/1-8.

93. Arnold, M. S.; Stupp, S. I.; Hersam, M. C. *Nano Lett.* **2005**, *5*, 713-718.

# Chapter 2

# Characterization of DNA-Wrapped Carbon Nanotubes

## 2.1 Abstract

Carbon nanotubes can be dispersed individually in aqueous solution by noncovalent association with single-stranded DNA. Here, we adapted the literature procedure to produce solutions of DNA-wrapped carbon nanotubes (CNT–DNA) for spectrophotometric and electrochemical studies (Chapters 2 and 4), as well as an investigation of the DNA wrapping structure (Chapter 3). Typical CNT–DNA preparations yielded a final solution concentration of 450 μg $mL^{-1}$ or ~2.7 μM CNT and an estimated 5.5–50 μM DNA. Absorbance and fluorescence spectroscopy suggest CNT types including (6,5), (7,5), (6,4), (8,3), (9,1), (8,4), (7,6), (8,6), and (8,7) are present in solution as individually suspended CNTs.

Treatment with reducing agents demonstrates the near lack of native positive-charge doping in this CNT–DNA, while reaction with hexachloroiridate(IV) oxidant caused significant CNT oxidation, which was observed by absorbance spectroscopy. Spectrophotometric titration revealed the availability of ~39 μM electrons per absorbance unit of CNT–DNA (measured with 1-cm path length) to an oxidant with a redox potential of 700 mV vs. Ag/AgCl, which corresponds to the removal of ~500 electrons per CNT–DNA. The resulting oxidized CNT–DNA was unstable in aqueous solution and was spontaneously reduced in a manner dependent upon pH and the redox potential of each CNT type. We propose that the observed reduction of the majority of oxidized CNT–DNA over time results

from the complete, sacrificial oxidation of a minor amount of CNT at susceptible sites such as defects and the nanotube ends, in a mechanism involving initial nucleophilic addition of hydroxide.

In contrast to this reversible redox chemistry observed for CNT–DNA in solution, we observed no direct, reversible electron transfer at an electrode. CNT–DNA was irreversibly oxidized at high potential (~1100 mV vs. Ag/AgCl), but no evidence of electron transfer was observed at lower potentials, where the CNT redox potentials are predicted to lie. To investigate CNT–DNA oxidation in this region, we employed an indirect electrochemical experiment described in Chapter 4.

## 2.2 Introduction

**DNA-Wrapped Carbon Nanotubes.** Single-walled carbon nanotubes inspire multidisciplinary interest, with promising roles in nanoelectronics[1] and biology[2-4] and value as an analytical tool[5] (refer to Chapter 1). However, applications requiring isolated CNTs and access to CNTs of certain electronic character or optical properties are encumbered by the poor solubility of unmodified CNTs in aqueous and organic solvents. The water solubilization of CNTs facilitates these applications, is essential to the development of CNT biological uses, and has elucidated important nanotube properties, including their solution near-infrared fluorescence[6-8] and electrochemistry.[9, 10] Aqueous CNT solutions have been formed through chemical modification of CNTs[11] and also via noncovalent interactions with CNTs, such as the adsorption of surfactants[6] and polymer-wrapping.[12-14] Covalent functionalization adversely affects CNT electronic and optical properties;[15, 16] therefore, noncovalent modification has the advantage of providing CNTs with water solubility while

preserving their remarkable properties. A particularly useful and well-studied noncovalent dispersant for the water solubilization of CNTs is single-stranded (ss)DNA.[17]

Individually solubilized CNTs wrapped with ssDNA (CNT–DNA) can be produced by ultrasonication, which facilitates the separation of bundled CNTs and their association with ssDNA.[17] This CNT–DNA material consists of planar, aromatic DNA nucleobases π-stacked on the hydrophobic CNT surface,[17, 18] exposing the polyanionic DNA backbone to confer water solubility. In support of this proposed structure, the binding energies of single nucleotides to CNTs in water have been suggested by molecular dynamics simulations to be competitive with the van der Waals forces attracting two CNTs together.[19]

Structural modeling has demonstrated that the backbone flexibility of a short DNA oligonucleotide allows it to associate with the CNT in a variety of ways, including linear and helical wrapping.[17, 20] A model showing ssDNA helically wrapped around a CNT is depicted in Figure 2.1; the DNA nucleobases interact with the CNT surface while the sugar–phosphate backbone is oriented towards the exterior of the CNT–DNA hybrid. The structure of DNA on CNTs is further discussed in Chapter 3.

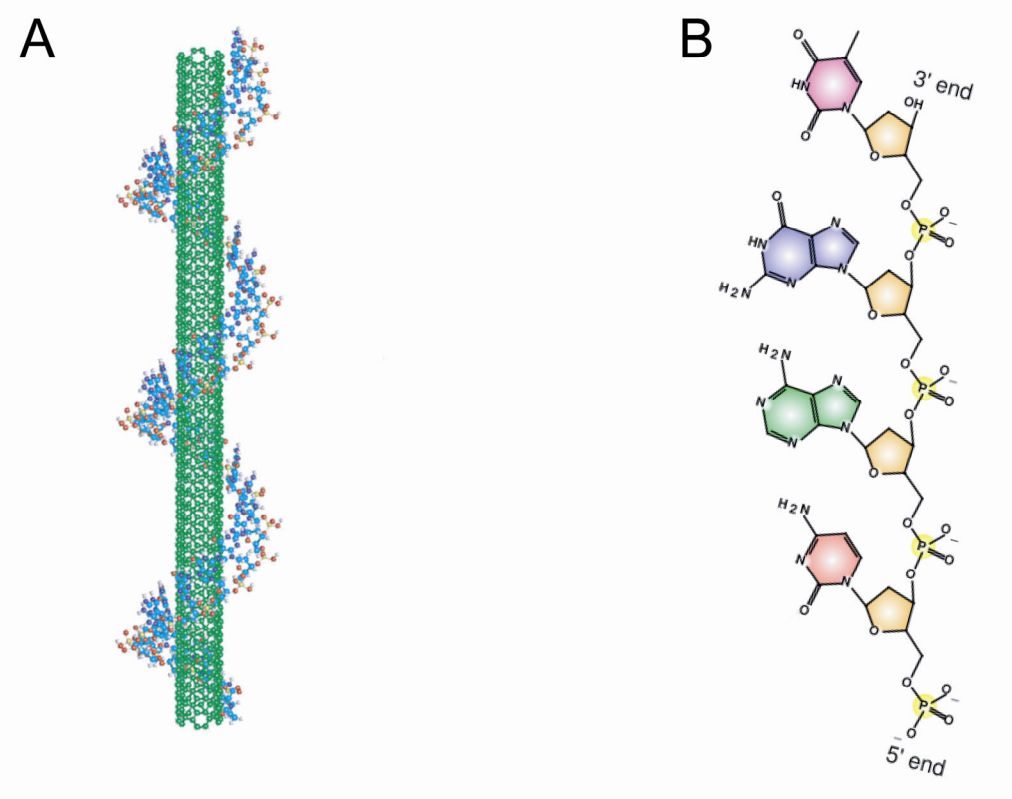


**Figure 2.1 Model of the interaction between a CNT and ssDNA.** (A) CNT–DNA in which ssDNA is helically wrapped around the CNT. (B) Structure of ssDNA, showing the planar, aromatic nucleobases and polyanionic sugar–phosphate backbone. Adapted from Enyashin, A.N., et al.[21]

**Applications of DNA-Wrapped Carbon Nanotubes.** ***Electronic Devices.*** Association of CNTs with DNA offers advantages in the construction of circuit components and sensors. CNT field effect transistors are improved by the DNA, which serves as a thin dielectric layer to prevent gate leakages and shorting.[22] Since CNTs are sensitive to environment, field-effect transistors built from CNT–DNA can also function as chemical sensors. The DNA coating allows for the detection of gas molecules that do not provoke a response in CNT transistors lacking DNA, and the device response can be tuned by employing different DNA sequences.[23] The DNA may also overcome the difficulty of constructing CNT electronic devices without lithography by employing the sequence-specific

nature of DNA base-pairing to arrange CNTs into useful architectures and to self-assemble electronic devices.[24-26]

***Advantages in Solution.*** While many CNT suspensions contain bundles whose inter-tube interactions alter CNT properties, CNT–DNA solutions contain individually solubilized CNTs with very low bundle content. The high quality of this dispersion makes CNT–DNA advantageous for studying the optical–electronic properties of individual CNTs,[9, 10, 27, 28] biological applications, and separating CNTs according to structural and electronic characteristics.

***Biological Applications.*** The use of the DNA biomolecule to dissolve CNTs makes it possible to apply molecular biology tools to manipulate CNTs and to interface CNTs with biological systems. CNT–DNA is nontoxic to a variety of cell lines at concentrations below ~25 μg $mL^{-1}$, suggesting their use in biological imaging, cellular drug delivery, and targeted cell destruction.[29] In biological imaging, CNTs are attractive fluorophores because of their resistance to photobleaching and emission wavelengths that avoid conflict with cellular autofluorescence (in both the 700–1100 nm window commonly used for bio-imaging and the more attractive region above 1125 nm).[30] Taking advantage of this fluorescence as well as the intense Raman scattering of CNTs, CNT–DNA has been employed *in vitro* as a long-term optical label.[3] In cellular drug delivery schemes, CNTs show promise because they can enter cells via endocytosis[31] and release attached cargo molecules.[32] CNT–DNA can enter living cells in culture and release DNA upon treatment with short pulses of near-IR radiation, demonstrating a biologically compatible delivery system for oligonucleotides.[4] Long, continuous near-IR irradiation of CNT–DNA inside cells causes heating of CNTs and subsequent cell death,[4] a method that has been employed to selectively destroy cells with

folate receptor tumor markers (using CNT–DNA modified with folate groups), while leaving normal cells unharmed.[4]

***CNT Sorting and Separation.*** Wrapping CNTs with DNA allows them to be chromatographically sorted by nanotube length, diameter, and (*n,m*) type (where *n* and *m* together describe the diameter and chirality, and thus the electronic character, of an individual CNT).[17, 33-36] Size-exclusion chromatography (SEC) affords separation by CNT length, producing samples with well-defined, narrow length distributions.[35] Anion-exchange chromatography, where column retention time depends on the effective charge density of each CNT–DNA (determined by the DNA wrapping geometry and the CNT electronic character and diameter), affords some separation between metallic and semiconducting CNTs and sorts the latter according to CNT diameter.[17, 33, 37] The combination of anion-exchange chromatography and SEC yields samples containing predominately one (*n,m*) type.[34] Since the heterogeneity of CNT samples is one of the largest obstacles to nanotube study and application, these achievements toward purifying CNTs highlight the usefulness of CNT–DNA hybrids.

## 2.3 Experimental Section

**Solubilization of Carbon Nanotubes with DNA.** The DNA wrapping procedure to dissolve CNTs was modified from the literature.[10, 17] Single-walled CNT gel made via the CoMoCAT process was purchased from SouthWest NanoTechnologies (Norman, OK), and oligonucleotides were synthesized and lyophilized by MWG-Biotech, Inc. (High Point, NC). The oligonucleotides used to make CNT–DNA are identified in Table 2.1; their molecular weight values were provided by the supplier, and molar extinction coefficients were

calculated using the "nearest-neighbor" approach.[38] In-house distilled water was passed through a Milli-Q Plus water purification system (Millipore; Bedford, MA), and buffer chemicals were used as received from Sigma-Aldrich (St. Louis, MO).

CNT–DNA was produced from a 1-mL mixture of CNT gel (10 mg) and oligonucleotide (1 mg $mL^{-1}$) in 100 mM sodium phosphate buffer (pH 7.0). This mixture was tip-sonicated (VC130 PB, Sonics and Materials Inc., Newtown, CT) in a microcentrifuge tube on an ice-water bath for 2 h at 3 W, with vortex agitation every 15 minutes. The resulting material was centrifuged (Eppendorf 5415 C) for 1.5 h at ~16,000g and the supernatant sonicated further (1 h at 3 W) and centrifuged (1 h at ~16,000g).

To remove unsuspended bundled CNTs, the supernatant was purified by passage through 0.45-μm Millex-HV syringe-tip filters (Millipore). To remove free oligonucleotide, the solution was passed through Y100 kDa molecular weight cut-off filters (Millipore) by centrifuging for 10 minutes at ~10,000g and then adding buffer to and inverting the filters into new tubes to re-suspend the CNT–DNA material (by centrifuging for 4 minutes at ~4,000g). These purification steps were repeated; then the solution was centrifuged (1 h at ~16,000g) and the supernatant retained to yield the final CNT–DNA solution.

**Table 2.1 Characteristics of Deoxyribooligonucleotide Sequences for CNT–DNA**

| Sequence Name (includes any modifications) | Sequence (5′ to 3′) | Molecular Weight (g mol$^{-1}$) | Extinction Coefficient at 260 nm (M$^{-1}$ cm$^{-1}$) |
|---|---|---|---|
| $T_{30}$ | TTT TTT TTT TTT TTT TTT TTT TTT TTT TTT | 9,064 | 243,600 |
| $T_{60}$ | TTT TTT TTT TTT TTT TTT TTT TTT TTT TTT TTT TTT TTT TTT TTT TTT TTT TTT TTT TTT | 18,189 | 486,600 |
| $(GT)_{30}$ | GTG TGT GTG TGT GTG TGT GTG TGT GTG TGT GTG TGT GTG TGT GTG TGT GTG TGT GTG TGT | 18,940 | 565,200 |
| 5′-thiol-$(GT)_{30}$ | Refer to $(GT)_{30}$ | 19,199 | 565,200 |
| 5′,3′-dithiol-$(GT)_{30}$ | Refer to $(GT)_{30}$ | 19,416 | 565,200 |
| 5′-biotin-$(GT)_{30}$ | Refer to $(GT)_{30}$ | 19,387 | 565,200 |
| $T_{120}$ | TTT TTT TTT TTT TTT TTT TTT TTT TTT TTT TTT TTT TTT TTT TTT TTT TTT TTT TTT TTT TTT TTT TTT TTT TTT TTT TTT TTT TTT TTT TTT TTT TTT TTT TTT TTT TTT TTT TTT TTT | 36,441 | 963,900 |
| 5′-thiol-$(GT)_{60}$ | GTG TGT GTG TGT GTG TGT GTG TGT GTG TGT GTG TGT GTG TGT GTG TGT GTG TGT GTG TGT GTG TGT GTG TGT GTG TGT GTG TGT GTG TGT GTG TGT GTG TGT GTG TGT GTG TGT | 38,272 | 1,120,500 |

**Absorbance Spectroscopy.** Spectra were collected using Cary 300-Bio UV-visible and Shimadzu UV-3600 UV–VIS–NIR spectrophotometers. A baseline spectrum (or single-wavelength reading) of the cuvette containing the same solvent as the analyte solution was subtracted from all spectra (and single-wavelength readings).

**Determination of CNT Concentration.** The concentration of CNT in CNT–DNA solutions was determined from the 990-nm absorption peak, where 13 μg $mL^{-1}$ CNT yields 1 absorbance unit in a 1-cm cuvette.[9] For approximation of the *molar* concentration of CNTs, a molecular weight of ~170,000 g $mol^{-1}$ was calculated for a CNT with 144-nm length and 0.8-nm diameter (the average length[39] and diameter[40] in our sample).

The simplest geometry to use for this calculation is that of an achiral CNT. The circumference of this CNT is formed by alternating distances equal to the carbon-to-carbon bond distance (0.142 nm) and the distance between two carbon atoms spanning a regular hexagon, which can be observed from the unrolled nanotube in Figure 2.2. When this CNT is rolled into a cylinder along the blue vector so that the red carbon atoms overlap, its circumference will be the sum of the distances shown. The diameter (d) of the CNT is therefore related (1) to the number of atoms (n) contained in one strip of carbon atoms forming the CNT circumference (c) (i.e., n = the carbon atoms along the blue vector in Figure 2.2, where the red atom is shown twice).

$$(1) \qquad c = \pi d = n [\, 0.5(0.284) + 0.5(0.142) \,]$$

The value of n was determined in this way for a CNT with 0.8-nm diameter and scaled with the total number of such carbon strips in a 144-nm long CNT. Note from Figure

2.2 that each addition of n carbon atoms to the CNT extends the CNT length by 0.123 nm. Therefore, a CNT of ~144-nm length contains ~14,000 carbon atoms (or, more generally, every nanometer of CNT length contains ~100 C atoms), giving a molecular weight of ~170,000 g $mol^{-1}$.

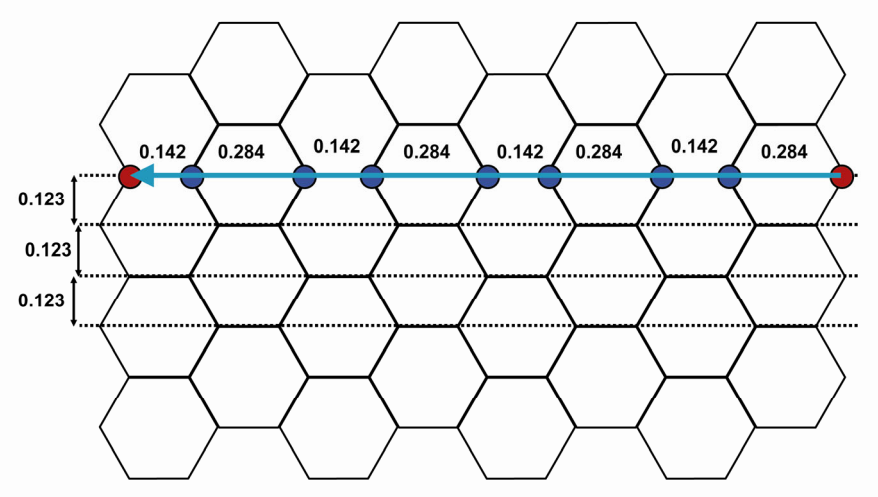


**Figure 2.2 Geometry of an achiral CNT for average molecular weight determination.** This short, unrolled CNT contains eight carbon atoms along its circumference; the carbon in red is shown twice to indicate how the CNT will look when rolled along the blue arrow to form a seamless cylinder. The CNT circumference is the sum of the values (in nm) shown along the blue arrow. Each addition of 0.123 nm in length to the CNT adds another eight carbon atoms to the total mass.

**Determination of DNA Concentration.** The concentration of DNA in a solution of CNT–DNA was determined in two ways: by accounting for DNA lost during the preparation of CNT–DNA (method 1) and through quantification of DNA that could be removed from the final CNT–DNA solution (method 2).

***Method 1.*** During the preparation of CNT–DNA, some volume of reaction mixture assumed to be homogeneous in DNA concentration was lost during the ultrasonication, centrifugation, and 0.45-μm filtration steps. DNA was also removed by molecular weight

cut-off filtration, in which the CNT–DNA material was retained on the filter, while only unwrapped DNA passed through. Therefore, an estimation of the concentration of DNA that remained in the final CNT–DNA could be made by subtracting the moles of DNA lost in each step of the preparation from the initial moles of DNA.

***Method 2.*** The second approach to ascertain the concentration of DNA in the CNT–DNA material was to remove its DNA by the addition of phosphoric acid. This acid treatment caused CNT precipitation as a fine black particulate, leaving a clear solution of DNA that could be isolated through 0.45-μm filtration and measured by absorbance spectroscopy to quantify the number of moles of DNA removed from the CNT–DNA. The precipitated CNTs were washed several times with phosphoric acid, and the acid solutions filtered and measured for DNA absorption until no further DNA was removed.

**Fluorescence Spectroscopy.** CNT–DNA samples were diluted with water to a CNT concentration of 8.0 μg $mL^{-1}$ (~47 nM) in emission cells of 1-cm path length and purged of oxygen by bubbling with Ar gas (for 1 h or longer). Emission and excitation spectra were collected using a Photon Technology International Inc. QuantaMaster 4SE-NIR5 emission instrument with InGaAs near-infrared detection and a lock-in amplifier. A 760-nm cut-off filter was placed between the sample and the near-infrared detection monochromator, and the slits allowed 8-nm excitation bandwidth and 16-nm detection bandwidth. Emission spectra were collected by exciting samples at 573 or 660 nm with detection in the 800–1600 nm range. Excitation spectra were collected by monitoring the emission intensity at 890, 976, 1003, or 1047 nm while scanning the excitation wavelength from 250 to 850 nm. All spectra were corrected for the monochromator response and the lamp intensity.

**Spectrophotometric Redox Titration.** Separate solutions of 6.75 μg $mL^{-1}$ (~40 nM) CNT–DNA in 100 mM sodium phosphate buffer (pH 7.0) were made with increasing concentrations of $K_2[IrCl_6]$ oxidant (in the range of 0–100 μM) and 800 μL total volume. To minimize the spontaneous reaction of $IrCl_6^{2-}$ to $IrCl_6^{3-}$ over time in the absence of CNT–DNA, a new oxidant solution was prepared for each titration solution and used immediately (after assessing its concentration with $\varepsilon_{487}$ = 3280 $M^{-1}$ $cm^{-1}$).[41] Absorbance spectra of CNT–DNA solutions after the addition of oxidant were collected with 1-cm path length from 1300–200 nm for 60 consecutive measurements (each lasting 114 s). Approximately 30 s elapsed between the time of the $K_2[IrCl_6]$ addition and collection of the first spectrum. The titration endpoint was determined by collecting absorbance spectra for solutions with 0, 10, 20, 30, 40, and 50 μM $K_2[IrCl_6]$ in three independent trials, each of which yielded similar results.

**Cyclic Voltammetry and Chronoamperometry.** Cyclic voltammetry (CV) and chronoamperometry (CA) were performed using a three-electrode cell assembly[42] and a CH Instruments 600 series potentiostat. The reduction potentials ($E_{1/2}$) of $K_2[IrCl_6]$, $K_4[Fe(CN)_6]$, and hydroquinone (Sigma-Aldrich) were determined for solutions in 100 mM sodium phosphate buffer at pH 7.0 with Pt disk working, Pt wire auxiliary, and Ag/AgCl reference electrodes. After five consecutive CVs of buffer (200 μL or more) at 25 mV $s^{-1}$ over the -200 to +1100 mV potential range, a CV of $K_2[IrCl_6]$, $K_4[Fe(CN)_6]$, or hydroquinone was collected with the same scan rate and potential range.

Direct electrochemistry of CNT–DNA was performed in 100 mM sodium phosphate buffer at pH 7.0 with ITO working, Pt wire auxiliary, and Ag/AgCl reference electrodes. ITO electrodes were prepared as described in Chapter 4, and a new cleaned ITO electrode was used for each experiment, with a rubber o-ring defining the exposed ITO surface area

(0.32 $cm^2$). This electrode was preconditioned in buffer (60 μL or more) by five consecutive CVs at 25 mV $s^{-1}$ over the 0–1250 mV potential range. Then CNT–$T_{60}$ was added to the preconditioning buffer (final concentration = 300 μg $mL^{-1}$ ≈ 1.8 μM CNT) and CV or CA performed. In CV, the potential was swept from 0 to 1250 to 0 mV at 25 mV $s^{-1}$, while in CA, the potential was held at 0 mV for 360 s, stepped to 1000 mV for 10 s, and stepped back to 0 mV for another 10 s. Control experiments with both techniques were performed for buffer in the absence of CNT–$T_{60}$.

## 2.4 Results and Discussion

**Solutions of DNA-Wrapped Carbon Nanotubes.** DNA has an affinity for the surface of CNTs in the absence of sonication,[43] suggesting that ssDNA associates with the exposed CNT surface area of raw CoMoCAT bundles. Upon sonication, a black dispersion of CNTs is formed, with the localized high temperature, pressure, and friction forces created by the collapse of cavitation bubbles in solution assisting in creating separation between individual CNTs in a bundle and allowing ssDNA to associate with each CNT. Since high-powered (~17 W) sonication causes CNT damage in organic solvents and, to a less-severe extent, in aqueous solutions,[44] we relied on low-powered (~3 W) sonication to disperse CNTs.

Our protocol to disperse CNTs with ssDNA and purify the resulting CNT–DNA was adapted from Zheng, M. et al.[17] with the goal of removing both excess ssDNA and bundles of CNTs.[10] CNT–DNA was purified of excess ssDNA via molecular weight cut-off filtration, which removed 29 ± 4% of the initial DNA content (n = 14). Another 22 ± 4% of the initial DNA was estimated to be lost in other purification steps (such as the reaction mixture

volume discarded after centrifugation), leaving about half of the DNA initially added to the CNTs available to form the soluble CNT–DNA product.

CNT bundles were removed via centrifugation and 0.45-μm filtration. The ~16,000g centrifugation steps resulted in a black homogeneous supernatant solution, leaving a small, diffuse pellet of black material at the bottom of the centrifuged tube. Likewise, 0.45-μm filtration permitted the black solution to pass through while retaining a small amount of black material on the filter. These centrifugation and 0.45-μm filtration steps were effective in removing bundled CNTs, as evidenced by the stability of the CNT–DNA solutions obtained after purification, which remained solubilized for months at room temperature without appreciable precipitation.

The absorbance spectrum of the final CNT–DNA solutions (Figure 2.3) contains an absorption continuum attributed to the π-plasmon (an oscillation of delocalized CNT π electronic states in the direction of the nanotube axis) and to absorption by carbonaceous impurities.[45] This feature increases towards higher energy with a peak at ~270 nm,[35] which is near the ~260 nm $\pi \rightarrow \pi^*$ absorptions of DNA nucleobases. In the visible and near-infrared, absorption peaks are observed resulting from electronic transitions of the different types of CNTs present in our sample. These narrow absorptions are indicative of a solution containing individually dispersed CNTs.[6]

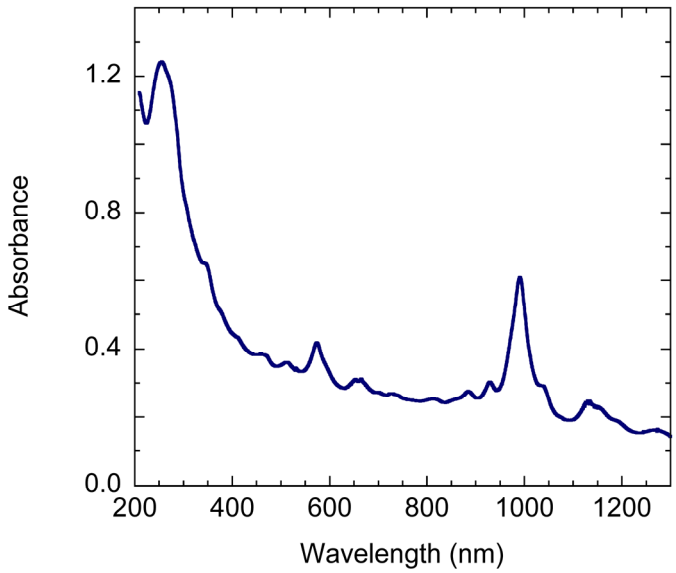


**Figure 2.3 Absorbance spectrum of CNTs wrapped with $(GT)_{30}$ oligonucleotide.** The spectrum was collected in 100 mM sodium phosphate, pH 7.0, and is representative of the CNT–DNA solutions used in this work.

**Concentrations of DNA and Carbon Nanotubes.** The concentration of CNT in CNT–DNA was determined from a mass extinction coefficient reported in the literature for CoMoCAT CNTs with the same absorption spectra (and distribution of CNT types) as our sample.[9] To convert this value to a molar concentration, we used the average molecular weight for CNTs in our sample (170,000 g $mol^{-1}$; refer to the Experimental Section). Typical CNT–DNA preparations yielded a final CNT concentration of 450 ± 40 μg $mL^{-1}$ or ~2.7 μM (n = 15), but could also be prepared at nearly double that concentration.

To estimate the concentration of DNA that remained in the final CNT–DNA solutions, two methods were employed. The first was an attempt to account for the amount of DNA lost during the CNT–DNA preparation (method 1), and the second was an unwrapping procedure to quantify the amount of DNA it was possible to remove from the prepared CNT–DNA material (method 2).

CNT–$T_{60}$ was estimated to contain 50 ± 6 μM DNA after preparation (n = 14; method 1), while phosphoric acid could remove 5.5 ± 0.3 μM DNA (n = 4; method 2). These values are in agreement with the reasonable expectation that method 1 would produce a high limit and method 2 a low limit on the true concentration of DNA in the solution. The first method assumes that all DNA in the original reaction mixture is retained except what quantity of DNA is shown to be lost during the CNT–DNA preparation; however, it is possible that further (unaccounted for) DNA loss occurs if DNA associates with CNT bundles that are discarded after centrifugation. The second method, on the other hand, only quantifies the DNA that can be successfully removed from the prepared CNT–DNA solution, and it is likely that some DNA remains associated with the precipitated CNTs or is otherwise lost in the unwrapping attempt. Therefore, it was useful to employ both strategies of estimating the concentration of DNA in CNT–DNA, which together suggest a range of 5.5 to 50 μM DNA in CNT–DNA.

This estimation of the DNA concentration compared to the approximate concentration of CNTs (2.7 μM) in a CNT–DNA solution suggests more DNA is present than CNT on a molar basis, with a molar ratio of ~2–19 60-mer DNA strands per CNT. This result is consistent with our structural model of DNA interaction with CNTs (discussed in Chapter 3), in which we propose that 3–4 60-mer oligonucleotides interact with one CNT of average length.

Additionally, some of the DNA measured for CNT–DNA is likely to be free in solution rather than associated with CNTs. Despite our use of purification steps to remove unwrapped DNA from samples, a dynamic equilibrium between the DNA associated with CNTs and free DNA would maintain some concentration of unwrapped DNA. Some

evidence for a slow equilibrium between associated and free DNA has been reported in the literature.[46] Our two methods of determining the DNA concentration in a solution of CNT–DNA do not distinguish between DNA that is dissolved in solution versus associated with the CNT; therefore, the likely presence of DNA in solution increases the observed ratio of DNA to CNT.

**Identification of CNT Types.** The CNT electronic transitions for the various CNT types present in our CNT–DNA are shown in the visible and near-infrared regions of absorbance spectra. Other reports of CNT–DNA absorbance spectra using CoMoCAT CNTs demonstrate an absence of CNT absorption peaks in the region from 1300 to 1850 nm,[47] where we were unable to collect data due to high solvent absorbance, and CNT broadband absorbance from 1590–1790 nm.[47] Our routinely collected spectra from 200–1300 nm therefore cover the range of CNT–DNA optical absorptions, which were assigned from the literature to the following semiconducting CNT types: (6,5), (7,5), (6,4), (8,3), (9,1), (8,4), (7,6), (8,6), and (8,7).[9, 27, 34, 36, 48] Our sample may also contain other semiconducting CNTs, such as (10,2), (9,7), (9,5), and (11,0), which are produced by the CoMoCAT method used to make the CNTs of our CNT–DNA.[27]

Each of these semiconducting CNTs exhibits three absorption peaks due to the $E_{11}$ ($v_1 \rightarrow c_1$), $E_{22}$ ($v_2 \rightarrow c_2$), and $E_{33}$ ($v_3 \rightarrow c_3$) electronic transitions between valence and conduction van Hove singularities. The CNT types responsible for $E_{11}$ and $E_{22}$ peaks are designated in Figure 2.4 in green and blue, respectively (some assignments were hindered due to overlapping absorptions). The shorter-wavelength $E_{33}$ ($v_3 \rightarrow c_3$) transitions are mostly unidentifiable due to the strong absorptions in the UV region; however, the $E_{33}$ transition of the (6,5) CNTs is visible at ~350 nm. The $E_{11}$ ($v_1 \rightarrow c_1$) transitions for specific metallic

CNTs in our sample could not be assigned from comparison to literature reports; these transitions occur in a region overlapping the $E_{22}$ and $E_{33}$ semiconducting transitions (dotted red region of the spectrum in Figure 2.4).

The relative intensities of the different CNT absorption peaks suggest our sample is predominately semiconducting, with over half the semiconductors having (6,5) and (7,5) chirality. This determination assumes a similar CNT length for the different chiral types, as samples with the same mass concentration of CNT exhibit increased absorption when the sample consists of longer nanotubes.[47] Our observation that CNT–DNA contains mostly semiconducting CNTs of the types identified here is consistent with the composition reported for CoMoCAT CNTs.[40]

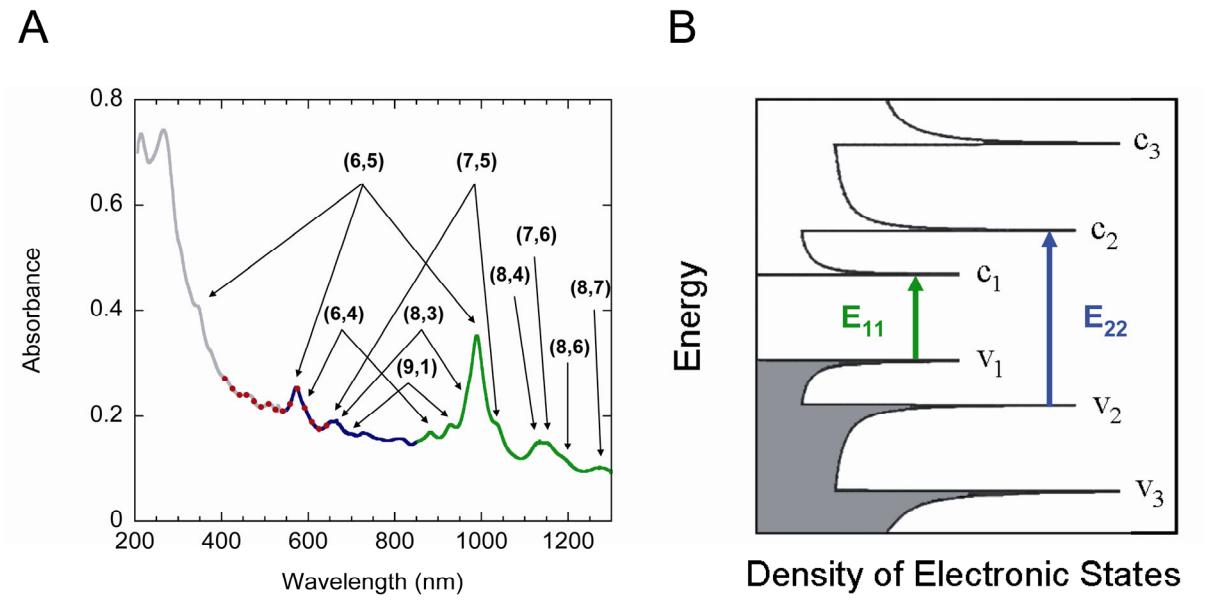


**Figure 2.4 Assignment of CNT–DNA electronic transitions to chiral CNT types.** (A) Absorption spectrum of CNT–$T_{60}$ in 100 mM sodium phosphate buffer, pH 7.0, with assignments of the major CNT types present. Colors indicate the approximate regions of semiconducting $E_{11}$ (1300–850 nm, green), semiconducting $E_{22}$ (850–550 nm, blue), and metallic $E_{11}$ (650–400 nm, dotted red) electronic transitions, in addition to the region that includes absorptions of the DNA, CNT π-plasmon, and semiconducting CNT $E_{33}$ transitions (400–200 nm, gray). (B) Density of states diagram for a semiconducting CNT showing the $E_{11}$ and $E_{22}$ transitions. Shading indicates states filled with electrons, and van Hove singularities are labeled in the valence ($v_n$) and conduction ($c_n$) bands.

**Fluorescence of DNA-Wrapped Carbon Nanotubes.** Excitation of semiconducting CNTs promoting the $v_1 \rightarrow c_1$, $v_2 \rightarrow c_2$, or $v_3 \rightarrow c_3$ absorptions results in $c_1 \rightarrow v_1$ fluorescence.[7] To observe this bandgap fluorescence, we excited CNT–DNA solutions at wavelengths near the $E_{22}$ absorptions of (6,5) and (7,5) CNTs and collected the resulting emission spectra. The observations of fluorescence (Figure 2.5A) and narrow absorption peaks (Figure 2.4A) suggest our CNT–DNA solutions consist of individually solubilized CNTs with few CNT bundles.[6]

The energy of CNT fluorescence (like absorption) depends on the energies of van Hove singularities and is therefore sensitive to CNT type. Emission energies have been

assigned to particular CNT types for surfactant-suspended CNTs by correlation with resonance Raman spectra,[7] and these energies are red-shifted in the DNA environment of CNT–DNA.[49] To determine the major CNT types contributing to the fluorescence peaks observed at 890, 976, 1003, and 1047 nm, we collected excitation spectra by scanning the excitation wavelength over the visible region comprising $E_{22}$ absorptions and monitoring the emission intensity at each of the four emission peak wavelengths. The excitation spectra of CNTs is particularly useful for (*n,m*) identification because CNTs such as (8,3) and (6,5), whose $E_{11}$ absorptions and emissions are close in energy and difficult to distinguish, have very different $E_{22}$ absorption energies. The overlapping emission peaks at 976 and 1003 nm can be readily assigned to the (8,3) and (6,5) CNTs, respectively, by comparison of excitation spectra monitored at each wavelength with the absorbance spectrum of the CNT mixture (Figure 2.5B). Comparison of the excitation and absorbance spectra allowed identification of the emission peak at 890 nm as (6,4), 976 nm as (8,3), 1003 nm as (6,5), and 1047 nm as (7,5) CNTs. Emission at 935 nm was assigned to (9,1) CNTs, and two unassigned CNT types absorbing at 470 and 510 nm could be identified as semiconducting, rather than metallic, with fluorescence in the region dominated by emission from (6,5), (8,3), and (7,5) CNTs.

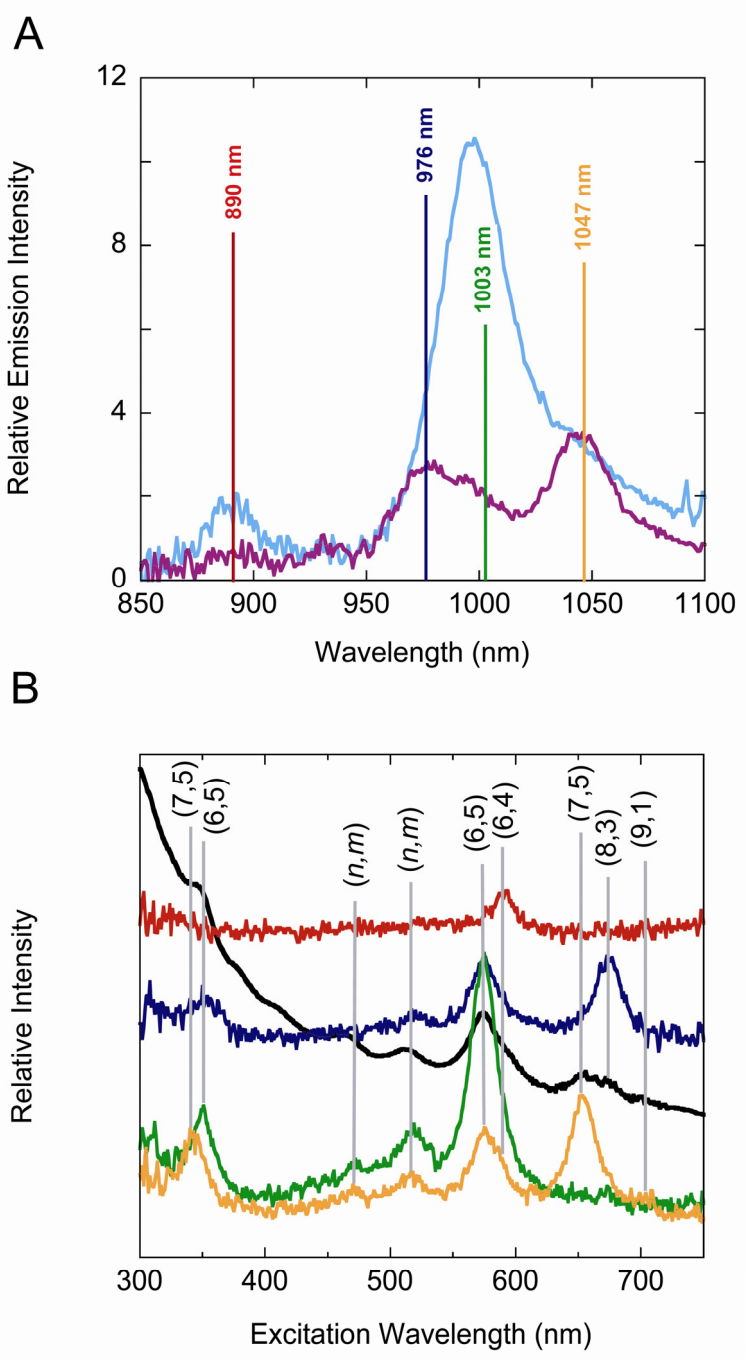


**Figure 2.5 CNT–DNA bandgap fluorescence.** (A) Emission spectra of CNT–$(GT)_{30}$ with excitation at 573 nm (light blue) and 660 nm (purple). (B) Excitation spectra with emission detection near each of the peaks observed in A; spectra are offset for clarity with colors corresponding to the detection wavelengths noted in A. Gray lines show excitation spectra assignments (made by comparison to the absorbance spectrum, black), allowing identification of the major contributing CNT type to each emission peak: (6,4) CNTs at 890 nm, (8,3) CNTs at 976 nm, (6,5) CNTs at 1003 nm, and (7,5) CNTs at 1047 nm.

The relative intensity of the observed emission peaks reflects both the relative abundance of the different CNT types and the degree of overlap between their $E_{22}$ absorption wavelength and the excitation wavelength. As expected, excitation at 573 nm produced prominent emission for the (6,5) and (6,4) CNTs (which have absorption peaks at 573 and 590 nm, respectively). Similarly, emission from (7,5), (8,3), and (9,1) CNTs (which absorb at 655, 670, and 700 nm, respectively) was more observable upon excitation at 660 nm. The emission spectra for these CNTs resemble their $E_{11}$ absorption spectra with a red-shift (~10 nm), as expected for some energy loss between absorption and emission. The (*n,m*) assignments are consistent with reported values,[49] and confirm the assignments made from absorption spectra for the semiconducting CNTs present in our CNT–DNA.

**Spectrophotometric Redox Titration of DNA-Wrapped Carbon Nanotubes.** When valence band electrons are depleted by chemical oxidation, the absorption of CNTs is bleached (i.e., oxidized CNTs have fewer valence electrons available to excite by the absorption of light).[9, 50] Absorbance spectroscopy is thus a useful means to monitor changes in CNT charge state, including those of CNT–DNA, where the density of electronic states is largely a superposition of the states for CNT and DNA.[21] To study the chemical oxidation of our CNT–DNA, we monitored the absorption spectrum while performing a redox titration with $K_2[IrCl_6]$. This Ir(IV) compound is a one-electron oxidant capable of oxidizing CNT–DNA in a reversible manner.[9] Use of $K_2[IrCl_6]$ as a titrant for CNT–DNA enriched in (6,5) CNTs has revealed an electron density of 2 μM electrons per absorbance unit at 990 nm (measured with 1-cm path length) for the first valence band of (6,5) CNTs.[9] In a similar titration, we determined the total electrons available from the CNT types present in our CNT–DNA for reaction with $K_2[IrCl_6]$.

The absorption peaks of CNT–DNA are bleached by the addition of $K_2[IrCl_6]$, indicating a solution redox reaction occurs to oxidize the CNTs (2). The extent of bleaching is dependent upon the concentration of oxidant added to the CNTs, with decreased absorbance as more CNT valence electrons are removed by higher concentrations of oxidant (Figure 2.6).

(2) $\quad CNT + Ir^{4+} \rightarrow CNT^{+} + Ir^{3+}$

This spectral bleach varies with CNT chiral type: the absorption peaks at higher wavelength are bleached prior to those at lower wavelength. In Figure 2.6A, note that addition of 2 μM oxidant partially bleaches the prominent $E_{11}$ absorption of the (6,5) tubes at 990 nm. The $E_{11}$ absorptions of CNTs at higher wavelength are significantly bleached, while those at lower wavelength (and all the $E_{22}$ absorptions) remain unaffected. This effect is the result of different redox potentials for different CNT types; when a small amount of $K_2[IrCl_6]$ is added to CNT–DNA, CNTs with lower redox potential are oxidized more readily than those of higher redox potential.

As the concentration of oxidant is increased, CNT absorptions are progressively bleached from higher to lower wavelength. This trend reflects the direct variation of CNT redox potential with the size of the CNT bandgap. CNT types with smaller bandgap energies absorb ($E_{11}$) at higher wavelength and have a lower redox potential (i.e., are easier to oxidize).[9, 51]

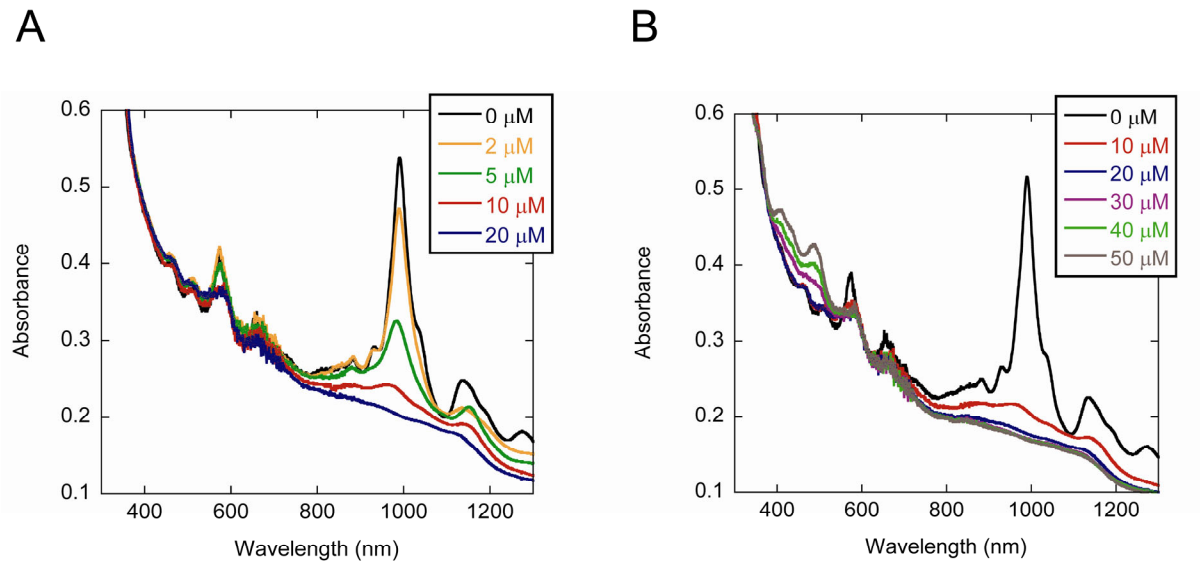


**Figure 2.6 Spectrophotometric titration of CNT–DNA with hexachloroiridate(IV) oxidant.** Absorbance spectra of 6.75 μg $mL^{-1}$ (~40 nM) CNT–DNA with increasing concentrations of $K_2[IrCl_6]$ in 100 mM sodium phosphate, pH 7.0, were collected using separate solutions to avoid dilution effects. (A) The CNT absorptions are bleached by the addition of oxidant, beginning with those at higher wavelength (lower redox potential) and progressing to those at lower wavelength (higher redox potential). (B) Addition of 20 μM oxidant results in a maximal bleach of CNT absorption peaks without any absorption of excess, unreacted oxidant (apparent in the 390–530 nm region).

The extent of the spectral bleach is maximized when excess $K_2[IrCl_6]$ is added relative to the number of available CNT–DNA electrons. For the CNT–DNA solution in Figure 2.6B, no further bleaching is observed for additions of oxidant greater than 20 μM, and the absorption bands of unreacted $K_2[IrCl_6]$ become visible in the 390–530 nm range for any further addition of oxidant. This 20 μM Ir(IV) addition therefore represents the titration endpoint, when all CNT valence electrons with redox potentials less than that of the $Ir^{4+/3+}$ redox couple (700 mV vs. Ag/AgCl) have been removed. Based on the extent of spectral bleaching, these electrons appear to include nearly all of the electrons in the first valence band (~1300–850 nm) and some of the electrons in the second valence band (< 850 nm) of the CNT types present in our CNT–DNA. For the prevalent (6,5) CNTs, $K_2[IrCl_6]$ removes

all electrons in the first valence band ($E_{11}$ = 990 nm) and approximately half of those in the second valence band ($E_{22}$ = 573 nm), suggesting 700 mV is more positive than the energy of the first valence band and positioned within the second valence band. This result is consistent with the reported redox potential of 600 or 580 mV for the first valence band of (6,5) CNTs.[9, 52]

Since $K_2[IrCl_6]$ is a one-electron oxidant, the concentration of $K_2[IrCl_6]$ necessary for complete reaction is equal to the number of electrons that can be removed from CNT–DNA. At the titration endpoint in Figure 2.6, the addition of 20 μM oxidant removes 20 μM electrons from the 6.75 μg $mL^{-1}$ CNT–DNA ($A_{990}$ = 0.519 measured with 1-cm path length), which means ~39 μM electrons are available per absorbance unit of CNT–DNA. This calculation directly correlates the mass concentration of CNT–DNA to the molar concentration of electrons available to an oxidant with $E_{1/2}$ = 700 mV vs. Ag/AgCl. Removal of 20 μM electrons from the approximate *molar* concentration of CNT–DNA present in this titration (40 nM) suggests 500 electrons are removed by $K_2[IrCl_6]$ from each nanotube.

**Reversibility of DNA-Wrapped Carbon Nanotube Chemical Oxidation.** The chemically oxidized CNT–DNA is not stable in neutral, aqueous solution. The CNT–DNA absorption peaks bleached by $K_2[IrCl_6]$ spontaneously reappear over time, eventually generating an absorbance spectrum nearly the same as that of CNT–DNA unexposed to oxidant. This observation suggests the nearly complete reduction of the chemically oxidized CNT–DNA, which was observed to occur more quickly at higher pH. Spectra in different buffered solutions recovered in the order: pH 7 > pH 6 > pH 4.7.

The reduction of oxidized CNT–DNA over time clearly demonstrates the higher redox potential of CNT types with higher-energy $E_{11}$ absorptions. Once oxidized, these CNT

types are stronger oxidizing agents than CNTs absorbing at lower energy and will therefore be reduced the fastest. Figure 2.7 shows this effect for the example of 2 μM oxidant added to ~40 nM CNT–DNA. This addition significantly bleaches the $E_{11}$ absorption peaks at wavelengths above 990 nm, partially bleaches the $E_{11}$ absorption of the (6,5) tubes at 990 nm, and has no effect on the $E_{11}$ absorptions below 990 nm. The maximal spectral bleaching caused by the addition of 2 μM $K_2[IrCl_6]$ occurs after ~30 s, and then the absorptions begin to spontaneously recover. Spectral recovery begins with the strongest oxidant, the oxidized (6,5) CNTs at 990 nm, which are reduced within ~10 minutes. The (7,5) CNTs at 1035 nm recover in ~20 minutes, and the (8,4), (7,6), and (8,6) CNTs at 1130, 1150, and 1200 nm, respectively, recover ~100 minutes after the addition of oxidant. Longer times result in the recovery of CNTs absorbing at even higher wavelength, such as the (8,7) CNTs at 1270 nm, eventually generating an absorbance spectrum very similar to that of the original, un-oxidized CNT–DNA.

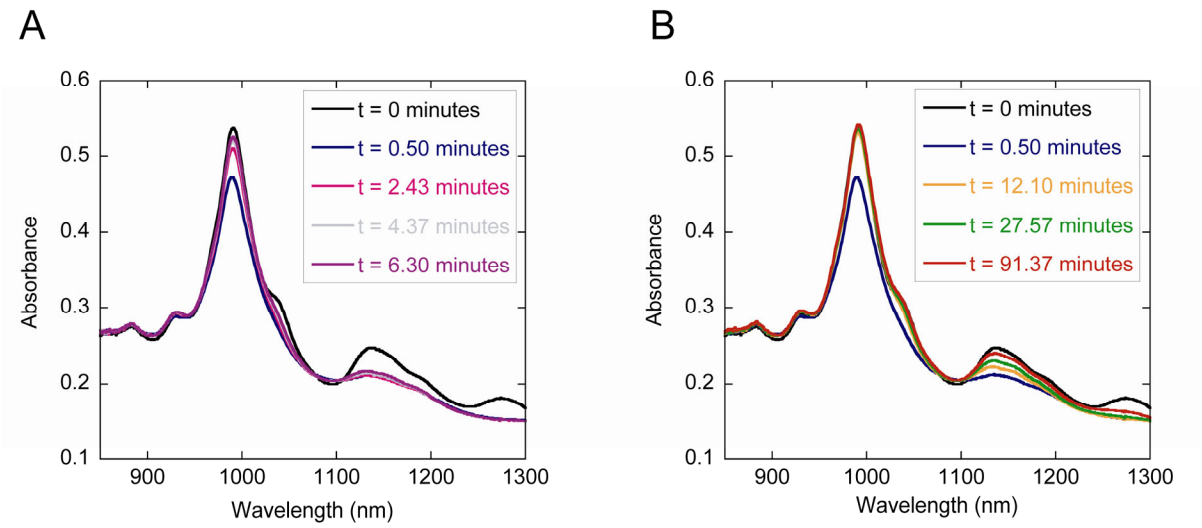


**Figure 2.7 Reduction of chemically oxidized CNT–DNA over time.** (A) Absorbance spectra of 6.75 μg $mL^{-1}$ (~40 nM) CNT–DNA before and at various times after the addition of 2 μM $K_2[IrCl_6]$. The bleached CNT absorption band at 990 nm for the (6,5) CNTs recovers in ~10 minutes, indicating reduction of the oxidized (6,5) CNTs. (B) Absorbance spectra at longer times following the same $K_2[IrCl_6]$ addition. The bleached CNT absorption band of the (7,5) CNTs at 1035 nm recovers by ~20 minutes after addition of oxidant. The (8,4), (7,6), and (8,6) CNTs at 1130, 1150, and 1200 nm, respectively, recover ~100 minutes after the addition of oxidant, and the (8,7) CNTs at 1270 nm recover at longer times.

Others have also reported the spontaneous recovery of absorption and fluorescence peaks for solutions of noncovalently functionalized CNTs after chemical oxidation.[9, 50] Two key observations about this reduction process involve the roles of pH and dissolved oxygen: reduction of oxidized CNTs is slower at lower pH and in the presence of oxygen. To account for these observations, a mechanism has been proposed implicating reduction of oxidized CNTs by water (3), which predicts slower CNT spectral recovery at high proton and oxygen concentrations.[9, 50]

(3) $CNT^+ + \frac{1}{2} H_2O \rightarrow CNT + \frac{1}{4} O_2 + H^+$

We propose another possible mechanism for the spontaneous reduction of oxidized CNTs. After chemical oxidation of CNTs (as occurs, for example, in Figure 2.6 upon the addition of 20 μM $IrCl_6^{2-}$), the majority of the sample could be reduced by the complete, sacrificial oxidation of a small number of nanotubes. Since CNTs are only partially oxidized by $IrCl_6^{2-}$, complete oxidation of one nanotube could reduce many Ir(IV)-oxidized CNTs, allowing the destruction of a small number of CNTs (or CNT sites) to accomplish the reduction of the bulk of the Ir(IV)-oxidized sample. In this scheme, the sacrificial oxidation is likely to be initiated by nucleophilic addition of $OH^-$ (or water) to the aromatic CNT structure, analogous to behavior seen for the self-reduction of polypyridyl transition metal complexes[53, 54] and accounting for the slower $CNT^+$ reduction reaction observed at lower pH. The reported observation that oxidized CNTs are reduced more slowly in the presence of $O_2$ may be attributed to the p-doping effect observed for CNTs when $O_2$ is present.[55, 56]

This mechanism avoids invoking the water oxidation half-reaction, which is notoriously difficult to accomplish, and is supported by our observation that the CNT–DNA absorbance spectrum does not fully recover after chemical oxidation and is noticeably reduced following a second round of oxidation (Figure 2.8). This spectrum does not recover any further over time and does not result from p-doping, as any excess Ir(IV) oxidant is reduced in neutral solution in a matter of days. The diminished CNT absorbance suggests that the spontaneous reduction process observed for oxidized CNT–DNA in solution causes some destruction of the CNT–DNA. CNTs are likely oxidized at defect sites or shortened by oxidation at the tube ends (Figure 2.8C).

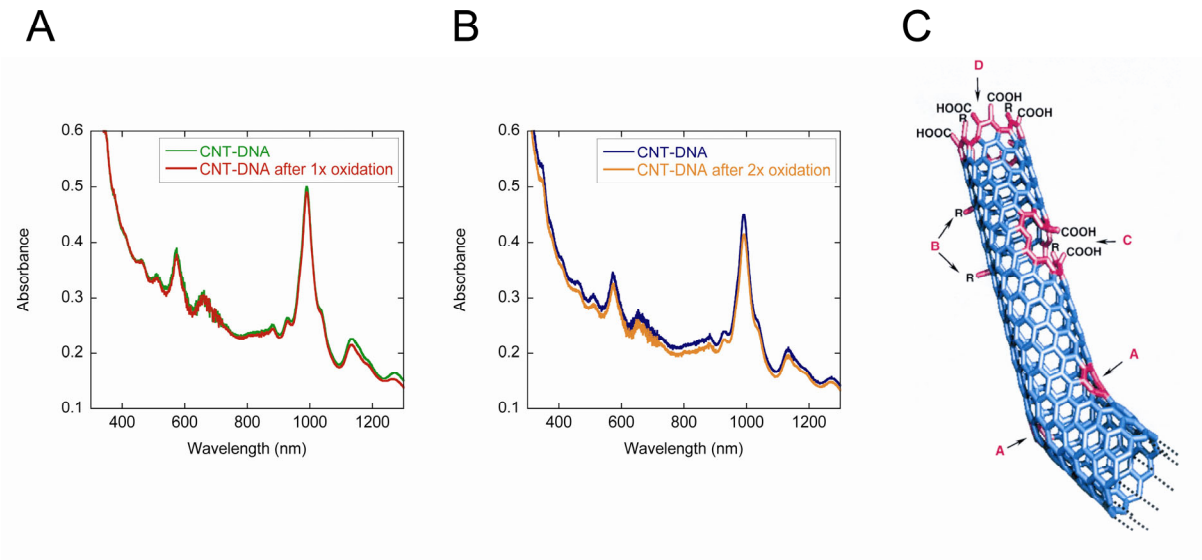


**Figure 2.8 CNT–DNA after cycles of chemical oxidation.** (A) Absorbance spectra of 6.5 μg $mL^{-1}$ (~38 nM) CNT–DNA in 100 mM sodium phosphate, pH 7.0, with and without 30 μM $K_2[IrCl_6]$. Spectra were collected 24 h after the addition of oxidant, showing the near recovery of the bleached CNT absorption spectrum. (B) Absorbance spectra 13 days after a second treatment with 30 μM $K_2[IrCl_6]$ (or equal-volume addition of buffer), showing diminished CNT absorbance after recovery (even after any $IrCl_6^{2-}$ oxidant has decomposed). (C) Model indicating the locations on a CNT that are susceptible to extensive oxidation: a) kinks caused by five- or seven-membered rings, b) $sp^3$-hybridized carbons functionalized with R = H or OH, c) defect sites along the CNT sidewall, and d) the open tube ends. Adapted from Hirsch, A.[57]

**Addition of Reducing Agents and Base to DNA-Wrapped Carbon Nanotubes.** Many CNT preparations exhibit p-doped behavior under ambient conditions, which has been attributed to a partial positive charge induced by adsorbed $H^+$ and $O_2$.[6, 52, 55, 56] To determine whether our CNT–DNA exhibits such p-doping, we monitored absorbance spectra during treatment with hydroquinone, $K_4[Fe(CN)_6]$, and sodium hydroxide. The reduction potentials of hydroquinone (two-electron, $E_{1/2}$ = 133 mV vs. Ag/AgCl) and $K_4[Fe(CN)_6]$ (one-electron, $E_{1/2}$ = 220 mV) are considerably lower than that of $K_2[IrCl_6]$ (one-electron, $E_{1/2}$ = 700 mV), which was observed to oxidize CNT–DNA (as discussed above). If CNT–DNA exhibits p-doping, the addition of these reducing agents should refill partially emptied CNT valence

bands and thus increase CNT absorbance. Likewise, if the CNT–DNA is being doped by protonation, CNT absorbance should be increased by the addition of NaOH.

However, we observed only slight increases in CNT–DNA absorbance upon treatment with reducing agents and base (Figure 2.9), indicating a low extent of p-doping in our CNT–DNA solutions. The positive charge-transfer predicted from physisorbed oxygen may be negated by negative charge transfer from the DNA nucleobases to the CNT,[21, 58] analogous to the effect of ammine-rich polymers on CNT transistors.[59] The negligible p-doping observed for CNT–DNA suggests the redox titration with $K_2[IrCl_6]$ described above and the electrochemical studies described below and in Chapter 4 were carried out with CNTs that did not have substantial charge doping.

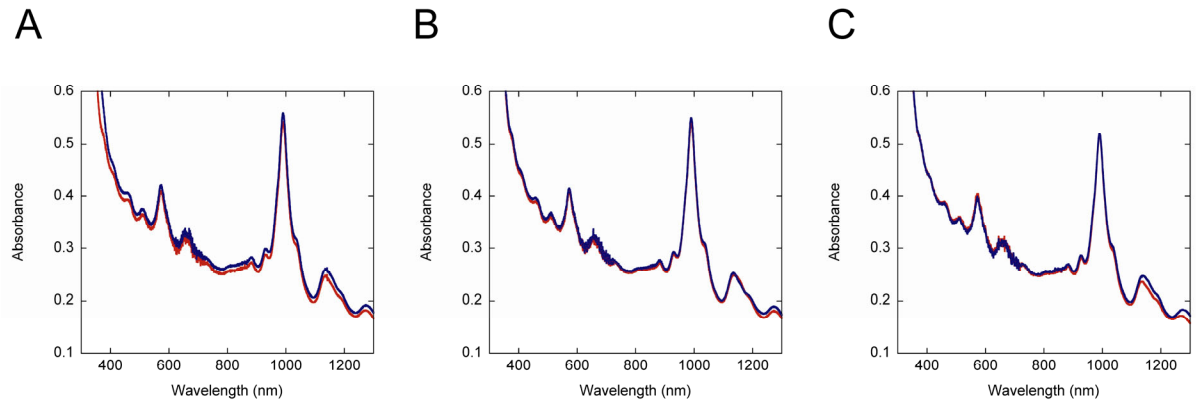


**Figure 2.9 CNT–DNA treated with reducing agents and base.** Absorbance spectra of CNT–DNA with (blue) and without (red) (A) $K_4[Fe(CN_6)]$, (B) hydroquinone, and (C) NaOH. Concentrations were: 7.1 μg $mL^{-1}$ (~42 nM) CNT–DNA with 1000 μM $K_4[Fe(CN_6)]$, 7.0 μg $mL^{-1}$ (~41 nM) CNT–DNA with 100 μM hydroquinone, and 6.8 μg $mL^{-1}$ (~40 nM) CNT–DNA with 5 mM NaOH (pH ≈ 11.7). Solutions were made in 100 mM sodium phosphate, pH 7.0, except in C, where solutions were in water. Spectra were collected ~30 s after addition of reagents, and no further spectral changes were observed over 24 h.

**Direct Electrochemical Behavior of DNA-Wrapped Carbon Nanotubes.** The reversible oxidation of CNT–DNA by chemical oxidants (such as $K_2[IrCl_6]$ described above) raises the question of whether CNT–DNA can be reversibly oxidized by a positively biased electrode. For CNTs serving as the working electrode, this behavior has been observed via spectroscopy, which demonstrates reversible depletion of the CNT valence band under an oxidative applied potential.[60, 61] Cyclic voltammetry (CV) showing this electrochemical charging of CNT-modified electrodes shows greatly enhanced current in the potential range of -1500 to +1500 mV vs. Ag/AgCl, which is attributed to charge injection.[61, 62] Here, we investigated the behavior of *solubilized* CNTs under an applied potential via CV and chronoamperometry (CA).

In CV experiments, the current response of a CNT–DNA solution was monitored as the electrode potential was increased at a constant rate (25 mV $s^{-1}$) from 0 to 1250 mV and back to 0 mV. CV of CNT–DNA shows an irreversible oxidation at ~1100 mV, but no reversible wave was observed in the vicinity of the reported redox potential (~600 mV vs. Ag/AgCl)[9] for CNT–DNA enriched in (6,5) CNTs (Figure 2.10A). In CA experiments, the current response of a CNT–DNA solution was monitored over time after changing the potential from 0 to 1000 mV in a quick step (rather than the steady potential sweep employed in CV). After 10 s, a potential step in the reverse direction (from 1000 to 0 mV) was executed to examine the reversibility of the initial oxidation. While the first (oxidizing) step demonstrated increased CNT–DNA current compared to the charging current of the buffer, indicating oxidation of CNT–DNA, the reverse (reducing) step showed very little difference between CNT–DNA and buffer (i.e., no reduction of the oxidized CNT–DNA formed in the

first step) (Figure 2.10B). This result is consistent with the CV and suggests that the CNT–DNA oxidation observed at 1100 mV is largely irreversible.

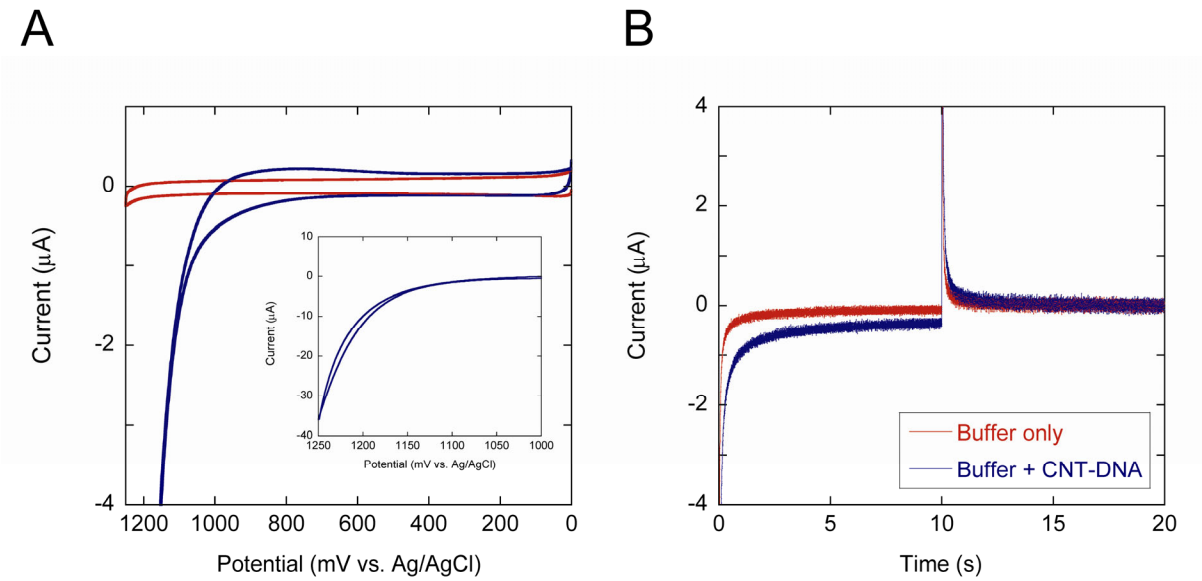


**Figure 2.10 Direct electrochemistry of CNT–DNA.** (A) Cyclic voltammogram of 300 μg $mL^{-1}$ (~1.8 μM) CNT–$T_{60}$ in 100 mM sodium phosphate buffer (pH 7.0) compared to the buffer-only voltammogram collected at 25 mV $s^{-1}$. Inset: CNT–$T_{60}$ voltammogram shown with different scale. (B) Chronoamperogram of 300 μg $mL^{-1}$ (~1.8 μM) CNT–$T_{60}$ in 100 mM sodium phosphate buffer (pH 7.0) compared to the buffer-only amperogram. The first step was from 0 to 1000 mV, and the reverse step was executed 10 s later from 1000 to 0 mV.

Additionally, the current response of the first CA step (in which CNT–DNA is oxidized) was found to be linear when graphed as the charge (the integral of current over time) versus the square root of time. This response follows the integrated Cottrell equation (4), in which charge (Q) under conditions of diffusion control depends upon the square root of time (as well as constants: the stoichiometric number of electrons transferred, n; Faraday's constant, F; electrode area, A; bulk concentration of CNT–DNA, $C^*$; and diffusion coefficient of CNT–DNA, D).[63] Therefore, our direct electrochemical measurements of

CNT–DNA demonstrate irreversible oxidation of CNT–DNA that is not adsorbed to the electrode but instead freely diffusing in solution.

(4) $Q = 2\ n\ F\ A\ C^{*}\ D^{1/2}\ \pi^{-1/2}\ t^{1/2}$

Our observation is consistent with the potential window observed for electrodes made from CNT–DNA, which shows irreversible oxidation in aqueous 100 mM KCl at ~1200 mV vs. Ag/AgCl.[64] It is likely that this irreversible oxidation of CNT–DNA results in functionalization or partial destruction of the nanotubes. Irreversible oxidation of CNTs has been observed for CNT-modified electrodes at high positive potential, either during laser irradiation[61, 62] or in sulfuric acid, which has been suggested to result in C–O bond formation.[65] Even without an applied potential, chemical reaction of CNTs under harsh acidic or oxidative conditions leads to extensive carboxylation of CNT tube ends and defect sites along the CNT sidewalls[66] and can shorten CNTs by attacking the nanotube ends.[67] Future studies of the length distribution and infrared spectra of CNT–DNA after bulk electrolysis may reveal whether the solubilized CNTs are extensively damaged at a positively biased electrode.

Direct electrochemical analysis of CNT–DNA demonstrated only this irreversible oxidation at high potentials. No evidence was observed of reversible CNT valence band depletion and filling for CNT–DNA in solution as would be expected for CNTs utilized as the working electrode. We interpret this absence of reversible CNT–DNA oxidation at an ITO electrode as the result of slow electron transfer kinetics on the time-scale of the electrochemical experiments. This behavior is typical for many compounds analyzed at ITO

electrodes[68, 69] and suggests the use of *indirect* electrochemistry to study CNT–DNA oxidation. Our investigation using this indirect approach is the subject of Chapter 4.

## 2.5 Conclusions

Our CNT–DNA was found to consist of mostly semiconducting CNT types consistent with the composition reported for CoMoCAT CNTs. The observation of fluorescence as well as narrow absorption peaks suggests that solutions consist of individually solubilized CNTs with few CNT bundles. The estimated molar ratio of ~2–19 DNA strands per CNT in CNT–$T_{60}$ is consistent with our structural model of the interaction between DNA and CNTs, in which we propose that 3–4 oligonucleotides of 60-base length interact with one average-length CNT (Chapter 3).

While we observed very little native p-doping of the CNT–DNA solutions, CNT–DNA could be oxidized by chemical reagents in solution. Spectrophotometric titration of CNT–DNA with hexachloroiridate(IV) revealed the availability of ~39 μM electrons per absorbance unit of CNT–DNA (1-cm path length) to an oxidant with 700-mV redox potential (vs. Ag/AgCl), which corresponds to the removal of ~500 electrons per CNT–DNA. This chemical oxidation of CNT–DNA is spontaneously reversible and reduction occurs faster at higher pH, which we explain by a mechanism of hydroxide attack on susceptible CNT–DNA sites to initiate the complete oxidation of a small amount of CNT–DNA, providing the electrons necessary to reduce the majority of the sample.

In contrast to the oxidation of CNT–DNA by solution oxidants, we observed no reversible redox of CNT–DNA at an electrode. CNT–DNA was irreversibly oxidized at high potential (~1100 mV vs. Ag/AgCl), but no reversible redox was observed by direct

electrochemistry at lower potentials where the CNT redox potentials are expected. These findings suggest the usefulness of examining the structure of DNA on CNT–DNA (Chapter 3) and employing indirect electrochemistry to investigate CNT–DNA oxidation (Chapter 4).

## 2.6 References


1. Colbert, D. T.; Smalley, R. E. *Trends Biotechnol.* **1999**, *17*, 46-50.

2. Barone, P.; Baik, S.; Heller, D. A.; Strano, M. S. *Nat. Mater.* **2005**, *4*, 86-92.

3. Heller, D. A.; Baik, S.; Eurell, T. E.; Strano, M. S. *Adv. Mater.* **2005**, *17*, 2793-2799.

4. Kam, N. W. S.; O'Connell, M.; Wisdom, J. A.; Dai, H. *Proc. Natl. Acad. Sci. USA* **2005**, *102*, 11600-11605.

5. Trojanowicz, M. *Trends Anal. Chem.* **2006**, *25*, 480-489.

6. O'Connell, M. J.; Bachilo, S. M.; Huffman, C. B.; Moore, V. C.; Strano, M. S.; Haroz, E. H.; Rialon, K. L.; Boul, P. J.; Noon, W. H.; Kittrell, C.; Ma, J.; Hauge, R. H.; Weisman, R. B.; Smalley, R. E. *Science* **2002**, *297*, 593-596.

7. Bachilo, S. M.; Strano, M. S.; Kittrell, C.; Hauge, R. H.; Smalley, R. E.; Weisman, R. B. *Science* **2002**, *298*, 2361-2366.

8. Strano, M. S.; Doorn, S. K.; Haroz, E. H.; Kittrell, C.; Hauge, R. H.; Smalley, R. E. *Nano Lett.* **2003**, *3*, 1091-1096.

9. Zheng, M.; Diner, B. A. *J. Am. Chem. Soc.* **2004**, *126*, 15490-15494.

10. Napier, M. E.; Hull, D. O.; Thorp, H. H. *J. Am. Chem. Soc.* **2005**, *127*, 11952-11953.

11. Pompeo, F.; Resasco, D. E. *Nano Lett.* **2002**, *2*, 369-373.

12. O'Connell, M. J.; Boul, P.; Ericson, L. M.; Huffman, C.; Wang, Y.; Haroz, E.; Kuper, C.; Tour, J.; Ausman, K. D.; Smalley, R. E. *Chem. Phys. Lett.* **2001**, *342*, 265-271.

13. Star, A.; Steuerman, D. W.; Heath, J. R.; Stoddart, J. F. *Angew. Chem. Int. Ed.* **2002**, *41*, 2508-2512.

14. Dieckmann, G. R.; Dalton, A. B.; Johnson, P. A.; Razal, J.; Chen, J.; Giordano, G. M.; Munoz, E.; Musselman, I. H.; Baughman, R. H.; Draper, R. K. *J. Am. Chem. Soc.* **2003**, *125*, 1770-1777.

15. Bahr, J. L.; Yang, J.; Kosynkin, D. V.; Bronikowski, M. J.; Smalley, R. E.; Tour, J. M. *J. Am. Chem. Soc.* **2001**, *123*, 6536-6542.

16. Banerjee, S.; Hemraj-Benny, T.; Wong, S. S. *Adv. Mater.* **2005**, *17*, 17-29.

17. Zheng, M.; Jagota, A.; Semke, E. D.; Diner, B. A.; McLean, R. S.; Lustig, S. R.; Richardson, R. E.; Tassi, N. G. *Nat. Mater.* **2003**, *2*, 338-342.

18. Hughes, M. E.; Brandin, E.; Golovchenko, J. A. *Nano Lett.* **2007**, *7*, 1191-1194.

19. Frischknecht, A. L.; Martin, M. G. *J. Phys. Chem. C* **2008**, *112*, 6271-6278.

20. Johnson, R. R.; Johnson, A. T. C.; Klein, M. L. *Nano Lett.* **2008**, *8*, 69-75.

21. Enyashin, A. N.; Gemming, S.; Seifert, G. *Nanotechnology* **2007**, *18*, 245702-245712.

22. Lu, Y.; Bangsaruntip, S.; Wang, X.; Zhang, L.; Nishi, Y.; Dai, H. *J. Am. Chem. Soc.* **2006**, *128*, 3518-3519.

23. Staii, C.; Chen, M.; Gelperin, A.; Johnson, A. T. *Nano Lett.* **2005**, *5*, 1774-1778.

24. Chen, Y.; Liu, H.; Ye, T.; Kim, J.; Mao, C. *J. Am. Chem. Soc.* **2007**, *129*, 8696-8697.

25. Zuccheri, G.; Brucale, M.; Samori, B. *Small* **2005**, *1*, 590-592.

26. Keren, K.; Berman, R. S.; Buchstab, E.; Sivan, U.; Braun, E. *Science* **2003**, *302*, 1380-1382.

27. Chou, S. G.; Ribeiro, H. B.; Barros, E. B.; Santos, A. P.; Nezich, D.; Samsonidze, G. G.; Fantini, C.; Pimenta, M. A.; Jorio, A.; Filho, F. P.; Dresselhaus, M. S.; Dresselhaus, G.; Saito, R.; Zheng, M.; Onoa, G. B.; Semke, E. D.; Swan, A. K.; Unlu, M. S.; Goldberg, B. B. *Chem. Phys. Lett.* **2004**, *397*, 296-301.

28. Chou, S. G.; DeCamp, M. F.; Jiang, J.; Samsonidze, G. G.; Barros, E. B.; Plentz, F.; Jorio, A.; Zheng, M.; Onoa, G. B.; Semke, E. D.; Tokmakoff, A.; Saito, R.; Dresselhaus, G.; Dresselhaus, M. S. *Phys. Rev. B* **2005**, *72*, 195415/1-8.

29. Becker, M. L.; Fagan, J. A.; Gallant, N. D.; Bauer, B. J.; Bajpai, V.; Hobbie, E. K.; Lacerda, S. H.; Migler, K. B.; Jakupciak, J. P. *Adv. Mater.* **2007**, *19*, 939-945.

30. Cherukuri, P.; Bachillo, S. M.; Litovsky, S. H.; Weisman, R. B. *J. Am. Chem. Soc.* **2004**, *126*, 15638-15639.

31. Kam, N. W. S.; Jessop, T. C.; Wender, P. A.; Dai, H. *J. Am. Chem. Soc.* **2004**, *126*, 6850-6851.

32. Liu, Z.; Winters, M.; Holodniy, M.; Dai, H. *Angew. Chem. Int. Ed.* **2007**, *46*, 2023-2027.

33. Zheng, M.; Jagota, A.; Strano, M. S.; Santos, A. P.; Barone, P.; Chou, S. G.; Diner, B. A.; Dresselhaus, M. S.; McLean, R. S.; Onoa, G. B.; Samsonidze, G. G.; Semke, E. D.; Usrey, M.; Walls, D. J. *Science* **2003**, *302*, 1545-1548.

34. Zheng, M.; Semke, E. D. *J. Am. Chem. Soc.* **2007**, *129*, 6084-6085.

35. Huang, X.; McLean, R. S.; Zheng, M. *Anal. Chem.* **2005**, *77*, 6225-6228.

36. Arnold, M. S.; Stupp, S. I.; Hersam, M. C. *Nano Lett.* **2005**, *5*, 713-718.

37. Lustig, S. R.; Jagota, A.; Khripin, C.; Zheng, M. *J. Phys. Chem. B* **2005**, *109*, 2559-2566.

38. Tataurov, A. V.; You, Y.; Owczarzy, R. *Biophys. Chem.* **2008**, *133*, 66-70.

39. Campbell, J. F.; Tessmer, I.; Thorp, H. H.; Erie, D. A. *J. Am. Chem. Soc.* **2008**, *130*, 10648-10655.

40. Bachilo, S. M.; Balzano, L.; Herrera, J. E.; Pompeo, F.; Resasco, D. E.; Weisman, R. B. *J. Am. Chem. Soc.* **2003**, *125*, 11186-11187.

41. Jorgensen, C. K. *Mol. Phys.* **1959**, *2*, 309-332.

42. Willit, J. L.; Bowden, E. F. *J. Phys. Chem. B* **1990**, *94*, 8241-8246.

43. Cathcart, H.; Nicolosi, V.; Hughes, J. M.; Blau, W. J.; Kelly, J. M.; Quinn, S. J.; Coleman, J. N. *J. Am. Chem. Soc.* **2008**, *130*, 12734-12744.

44. Lu, K. L.; Lago, R. M.; Chen, Y. K.; Green, M. L. H.; Harris, P. J. F.; Tsang, S. C. *Carbon* **1996**, *34*, 814-816.

45. Pichler, T.; Knupfer, M.; Golden, M. S.; Fink, J. *Phys. Rev. Lett.* **1998**, *80*, 4729-4732.

46. Bauer, B. J.; Fagan, J. A.; Hobbie, E. K.; Chun, J.; Bajpai, V. *J. Phys. Chem. C* **2008**, *112*, 1842-1850.

47. Fagan, J. A.; Simpson, J. R.; Bauer, B. J.; Lacerda, S. H.; Becker, M. L.; Chun, J.; Migler, K. B.; Walker, A. R.; Hobbie, E. K. *J. Am. Chem. Soc.* **2007**, *129*, 10607-10612.

48. Dukovic, G.; Balaz, M.; Doak, P.; Berova, N. D.; Zheng, M.; McLean, R. S.; Brus, L. E. *J. Am. Chem. Soc.* **2006**, *128*, 9004-9005.

49. Strano, M. S.; Zheng, M.; Jagota, A.; Onoa, G. B.; Heller, D. A.; Barone, P. W.; Usrey, M. *Nano Lett.* **2004**, *4*, 543-550.

50. O'Connell, M.; Eibergen, E. E.; Doorn, S. K. *Nat. Mater.* **2005**, *4*, 412-418.

51. Okazaki, K.-I.; Nakato, Y.; Murakoshi, K. *Phys. Rev. B* **2003**, *68*, 035434-1/5.

52. Nish, A.; Nicholas, R. J. *Phys. Chem. Chem. Phys.* **2006**, *8*, 3547-3551.

53. Roecker, L.; Kutner, W.; Gilbert, J. A.; Simmons, M.; Murray, R. W.; Meyer, T. J. *Inorg. Chem.* **1985**, *24*, 3784-3791.

54. Ghosh, P.; Brunschwig, B. S.; Chou, M.; Creutz, C.; Sutin, N. *J. Am. Chem. Soc.* **1984**, *106*, 4772-4783.

55. Strano, M. S.; Huffman, C. B.; Moore, V. C.; O'Connell, M. J.; Haroz, E. H.; Hubbard, J.; Miller, M.; Rialon, K.; Kittrell, C.; Ramesh, S.; Hauge, R. H.; Smalley, R. E. *J. Phys. Chem. B* **2003**, *107*, 6979-6985.

56. Collins, P. G.; Bradley, K.; Ishigami, M.; Zettl, A. *Science* **2000**, *287*, 1801-1804.

57. Hirsch, A. *Angew. Chem. Int. Ed.* **2002**, *41*, 1853-1859.

58. Yang, Q.-H.; Gale, N.; Oton, C. J.; Li, F.; Vaughan, A.; Saito, R.; Nandhakumar, I. S.; Tang, Z.-Y.; Cheng, H.-M.; Brown, T.; Loh, W. H. *Nanotechnology* **2007**, *18*, 405706.

59. Shim, M.; Javey, A.; Kam, N. W. S.; Dai, H. *J. Am. Chem. Soc.* **2001**, *123*, 11512-11513.

60. Kazaoui, S.; Minami, N.; Matsuda, N. *Appl. Phys. Lett.* **2001**, *78*, 3433-3435.

61. Kavan, L.; Rapta, P.; Dunsch, L.; Bronikowski, M. J.; Willis, P.; Smalley, R. E. *J. Phys. Chem. B* **2001**, *105*, 10764-10771.

62. Kavan, L.; Rapta, P.; Dunsch, L. *Chem. Phys. Lett.* **2000**, *328*, 363-368.

63. Bard, A. J.; Faulkner, L. R. *Electrochemical Methods: Fundamentals and Applications*; John Wiley and Sons, Inc.: New York, 2001.

64. Hu, C.; Zhang, Y.; Bao, G.; Zhang, Y.; Liu, M.; Wang, Z. L. *J. Phys. Chem. B* **2005**, *109*, 20072-20076.

65. Sumanasekera, G. U.; Allen, J. L.; Fang, S. L.; Loper, A. L.; Rao, A. M.; Eklund, P. C. *J. Phys. Chem. B* **1999**, *103*, 4292-4297.

66. Bahr, J. L.; Tour, J. M. *J. Mater. Chem.* **2002**, *12*, 1952-1958.

67. Liu, J.; Rinzler, A. G.; Dai, H.; Hafner, J. H.; Bradley, R. K.; Boul, P. J.; Lu, A.; Iverson, T.; Shelimov, K.; Huffman, C. B.; Rodriguez-Macias, F.; Shon, Y.-S.; Lee, T. R.; Colbert, D. T.; Smalley, R. E. *Science* **1998**, *280*, 1253-1256.

68. Johnston, D. H.; Cheng, C.-C.; Campbell, K. J.; Thorp, H. H. *Inorg. Chem.* **1994**, *33*, 6388-6390.

69. Fecenko, C. J.; Meyer, T. J.; Thorp, H. H. *J. Am. Chem. Soc.* **2006**, *128*, 11020-11021.

# Chapter 3

## Structure of DNA-Wrapped Carbon Nanotubes

Reproduced in part with permission from Campbell, J. F.; Tessmer, I.; Thorp, H. H.; Erie, D. A. "Atomic Force Microscopy Studies of DNA-Wrapped Carbon Nanotube Structure and Binding to Quantum Dots" *J. Am. Chem. Soc.* **2008**, *130*, 10648–10655.



### 3.1 Abstract

Single-stranded DNA is an effective noncovalent dispersant for individual single-walled carbon nanotubes (CNTs) in aqueous solution, forming a CNT–DNA hybrid material that has advantages for CNT separations and applications. Atomic force microscopy (AFM) reveals a regular pattern on the surface of CNT–DNA. We found this pattern to be independent of the length and sequence of the wrapping DNA, yet different from the structures observed for CNTs dispersed with sodium dodecyl sulfate in the absence of DNA. We wrapped CNTs with thiol-modified DNA to form stable conjugates of CNT–DNA and core/shell CdSe/ZnS quantum dots; AFM imaging of these conjugates identified for the first time the location of DNA on the CNT–DNA nanomaterial. Our results suggest that the AFM pattern of CNT–DNA is formed by helical turns (~14-nm pitch) of wrapped DNA strands that are closely arranged end-to-end in a single layer along the CNT. This work demonstrates the useful functionalization of CNTs with quantum dots in a manner that avoids

direct, destructive modification of the CNT surface and suggests nearly complete surface coverage of the nanotubes with DNA.

## 3.2 Introduction

**Structure and Stability of DNA on Carbon Nanotubes.** In the applications envisioned for DNA-wrapped carbon nanotubes (CNT–DNA) described in Chapter 2, an important feature remains not entirely understood: the structure of ssDNA on the CNTs. Modeling and molecular dynamics simulations of CNT–DNA demonstrate the spontaneous helical wrapping of DNA around CNTs (Figure 2.1).[1-3] However, the flexibility of ssDNA allows for a variety of other potential structures, including achiral loops and disordered conformations of DNA on the CNT.[1-3] The formation of stable CNT–DNA solutions is driven by π-stacking interactions between DNA nucleobases and the CNT surface, where the nucleobase adsorption energy must compensate for the energy needed to break apart CNT bundles.[4] The conformation adopted by an oligonucleotide on the CNT surface is influenced by the positioning of each nucleobase to π-stack with the CNT and the electrostatic repulsion between phosphates of the DNA backbone, as well as the electronic and physical characteristics of each nanotube (*n,m*) type.[2-5] The connection between the DNA wrapping structure and intrinsic characteristics of each CNT is what allows the separation of CNT–DNA according to nanotube diameter and electronic character.[5-7] Since the separation of CNTs into homogenous samples is critical to most of their proposed applications, further investigation of the CNT–DNA structure is expected to prove valuable.

**Atomic Force Microscopy.** Atomic force microscopy (AFM) is an imaging technique with a superior resolution to that of optical microscopy, allowing investigation of

objects in the 10 to 200-nm size range that may be too complex for NMR or X-ray crystallographic analysis.[8] AFM has proven to be a useful alternative technique to electron microscopy, as it offers advantages over the vacuum environment and potentially damaging sample preparation required by traditional electron microscopy. With AFM, imaging can occur at room temperature, in air, and in a hydrated environment, which is particularly advantageous for the study of biological molecules in an environment more conducive to native structure.[8, 9]

In AFM, a sample is deposited onto an atomically flat surface such as freshly cleaved mica. To deposit DNA, an aqueous DNA solution containing $MgCl_2$ is placed on the mica surface for a few minutes, the excess solution blotted away, and the surface rinsed and then evaporated with nitrogen. The magnesium cation facilitates binding of the negatively charged DNA to the negatively charged mica surface.[8]

An area of the mica is imaged by moving it beneath a sharp tip (with an end radius of several nanometers) in a raster pattern so that the tip scans the entire area by physically interacting with the surface.[8] In tapping mode, the tip and the cantilever arm it is mounted upon are oscillated so that the tip comes into and out of contact with the surface. This intermittent contact between the tip and the surface has the advantage of reducing the lateral force applied to sample objects during imaging (which is much higher when AFM is performed in contact mode, where the tip is in constant contact with the surface during imaging).[8] Information is collected about the oscillating motion of the tip by training a laser onto the back of the cantilever arm and detecting the position of the reflected beam with photodiodes.

As the AFM tip interacts with the surface, tall objects of the sample deflect its motion, generating an image analogous to a topographical map of the substrate and sample. This height information is the typical image produced by AFM. Microscopes can also measure the phase of the oscillating tip motion, which shifts as the type of material on the surface changes. Phase shifts can be caused by changes in the composition, adhesion, and viscoelasticity of the material being imaged.[8] Phase images, therefore, have image contrast that gives qualitative information about the different materials on the substrate surface.

Here, we employed AFM to determine the structure of DNA in CNT–DNA. Our AFM measurements suggest a model of helically wrapped oligonucleotides that are closely arranged along the entire CNT in a single layer. Turns of the DNA around the CNT each generate a peak in the CNT–DNA height measured by AFM, forming a regular pattern on the nanotube surface. This analysis was supported by imaging CNTs wrapped with oligonucleotides of different lengths and by quantum dot (QD) labeling of the wrapping DNA, which enabled us to identify the location of the individual oligonucleotides on the nanotube surface. The impact of the oligonucleotide sequence was also investigated, and CNT–DNA was compared to CNTs dispersed with sodium dodecyl sulfate (SDS) in the absence of DNA. The insight gained into the organization of DNA on CNT–DNA is anticipated to benefit the future use of this nanomaterial in the study of solution nanotube properties and in the separation of CNTs by (*n,m*) type.

### 3.3 Experimental Section

**Atomic Force Microscopy.** AFM was performed in air using a Nanoscope IIIa microscope (Veeco Instruments, Santa Barbara, CA) in tapping mode to simultaneously

collect height and phase data. Images of 1–2 μm size were collected at 1–3 Hz scan rate and 512 x 512 pixel resolution. AFM cantilevers were Pointprobe Plus tapping mode silicon probes (Agilent Technologies, Tempe, AZ) with ~170 kHz resonance frequency.

**Imaging of DNA-Wrapped Carbon Nanotubes.** CNTs (CoMoCAT process,[10] SouthWest NanoTechnologies, Norman, OK) were wrapped with ssDNA (MWG-Biotech, High Point, NC) in a series of tip-sonication, centrifugation, and purification steps modified from the literature[1] (refer to Chapter 2). CNT–DNA solutions (2.7 μg $mL^{-1}$ or ~16 nM CNT) in 4-(2-hydroxyethyl)-1-piperazineethanesulfonic acid buffer (HEPES, 17 mM, pH 7.5) were prepared for imaging by heating (65°C, 10 minutes), cooling to RT, combining with a similarly heated $MgCl_2$ solution (6 mM), and depositing (10 μL) onto freshly cleaved ruby mica (Spruce Pine Mica Company, Spruce Pine, NC). After ~30 s incubation, the mica was rinsed three times by adding several drops of water, blotted, and evaporated under a nitrogen stream. All concentrations above are reported for the final deposition solution.

**Imaging of Surfactant-Suspended Carbon Nanotubes.** Samples of CNTs suspended by the adsorption of SDS in the absence of DNA (CNT–SDS) were prepared by drying (opening to air for 24 h) the CNT gel before bath-sonication (30 minutes) in a 1% SDS aqueous solution. CNT–SDS samples were deposited onto mica as described above (giving final concentrations of 0.1% SDS, 17 mM HEPES, and 6 mM $MgCl_2$).

Image analysis of both CNT–DNA and CNT–SDS was performed using Nanoscope III v5.12 software (Veeco Instruments) and Image SXM (S.D. Barrett, http://www.ImageSXM.org.uk). Measurements were made for CNTs longer than 50 nm (except for length measurements), excluding CNTs that were not visible (i.e., covered by carbonaceous impurities or large masses of surfactant), and are reported as the Gaussian

center ± one standard deviation (calculated using Origin, OriginLab Corp., Northampton, MA).

**Quantum Dot Labeling of DNA-Wrapped Carbon Nanotubes.** Quantum dot (QD) labeling studies were performed with core/shell CdSe/ZnS ($\lambda_{em}$ = 540 nm) EviDots from Evident Technologies (Troy, NY). A literature procedure was followed to substitute the trioctylphosphine oxide ligands with mercaptoacetic acid to yield water-soluble QDs,[11] and the QD concentration was determined spectrophotometrically from an extinction coefficient provided by Evident Technologies. To form CNT–DNA conjugates with QDs, CNT–DNA made with thiolated oligonucleotide (3.0 μg $mL^{-1}$ or ~18 nM CNT) was incubated with 2.2 μM QDs at RT for 24 h. This solution was deposited onto mica for imaging without heating, but otherwise as described above (with final concentrations of 2.7 μg $mL^{-1}$ or ~16 nM CNT, 17 mM HEPES, 6 mM $MgCl_2$, and 2.0 μM QD, which was chosen to optimize the QD surface coverage on the mica). The CNTs used in QD labeling experiments were wrapped with 5′-biotin-$(GT)_{30}$ (CNT–biotin), 5′-thiol-$(GT)_{30}$ (CNT–thiol), and 5′,3′-dithiol-$(GT)_{30}$ (CNT–dithiol) 60-mers or with the 5′-thiol-$(GT)_{60}$ 120-mer.

In image analysis, "QD-sized objects" refers to all round objects of height > 1 nm in contact with the CNT. Measurements of the distance between QD-sized objects on CNTs wrapped with thiolated oligonucleotide (reported as the Gaussian center ± one standard deviation) were made from the center of each object and excluded objects in contact with each other. The number of QD-sized objects per CNT (reported as the average ± one standard deviation for three experiments) was determined for CNTs longer than 100 nm, and a two-tailed one-way ANOVA with Bonferroni's post-hoc test ($p < 0.05$) was performed to

compare the data for each experimental group using Kaleidagraph (Synergy Software, Reading, PA).

**Calculations and Modeling.** CNTs built in the Microscope Simulator program[12] (http://www.cs.unc.edu/research/nano/cismm/) and used for calculations were 0.8 nm in diameter, which is consistent with both the height of unwrapped nanotube observed in AFM images and the reported diameter of CoMoCAT CNTs.[10] In CNT–DNA, the ssDNA backbone is ~0.5 nm above and below the nanotube due to π-stacking of bases on the CNT surface;[2, 4] ssDNA was therefore modeled as a helical pipe of 0.5-nm diameter tangent to the CNT. An AFM tip radius of 8 nm and cone angle of 20° were used in all simulations.[12]

To determine the number of turns made by one oligonucleotide wrapped helically around a nanotube, the ssDNA was treated as a wire positioned at the DNA backbone (Figure 3.1).

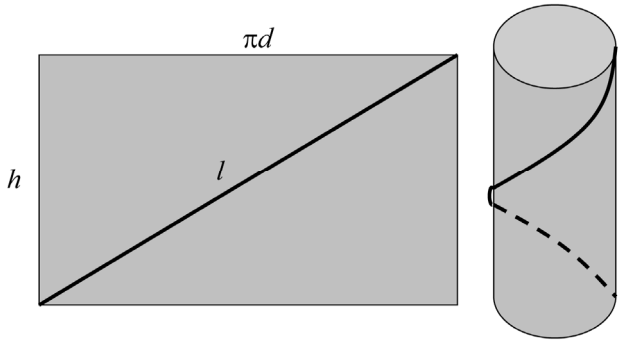


**Figure 3.1 Model for the geometry of helically wrapped DNA on a CNT.** Right: cylinder helically wrapped by one turn of a thin wire. Left: the unrolled cylinder with the wire forming its diagonal, noting the cylinder diameter (*d*), wire wrapping pitch (*h*), and length of the single turn of wire (*l*).

This wire is helically wrapped around a cylinder of 1.8-nm diameter (because the ssDNA backbone is ~0.5 nm above and below the 0.8-nm-diameter CNT[2, 4]). The ssDNA length (*L*),

its wrapping pitch ($h$), or the number of turns it makes around the cylinder ($n$) can be easily calculated when given the other two parameters. A cylinder (of diameter $d$) wrapped with one turn of ssDNA can be formed by rolling a rectangle so that its diagonal makes exactly one helical turn around the cylinder; the length ($l$) of that diagonal (i.e., one turn of the ssDNA) is then given by the Pythagorean theorem. The total length of the ssDNA is $l$ times the number of turns around the cylinder: $L = nl = n\sqrt{h^2 + (\pi d)^2}$. The length of an oligonucleotide was calculated by assuming a distance of 0.7 nm between phosphorus atoms on the ssDNA backbone ($L$ = 42 nm for one 60-mer). This distance is found in ssDNA adopting a C2′ *endo* conformation[13] (and can be calculated by treating one strand of a double helix with 3.4-nm pitch as a wire on a cylinder of 2-nm diameter).

### 3.4 Results

**Measurements of the DNA-Wrapped Carbon Nanotube Surface Pattern.** CNTs produced by the CoMoCAT process[10] were wrapped with a single-stranded guanine–thymine deoxyribooligonucleotide, $(GT)_{30}$. The CNT–$(GT)_{30}$ length distribution measured by AFM shows a trend to three different lengths (47 ± 45 nm, 172 ± 56 nm, and 311 ± 105 nm; Figure 3.2) with an average length of 144 ± 112 nm (n > 800), which is comparable to that reported for CNT–DNA made with HiPco-process CNTs via a similar protocol.[6]

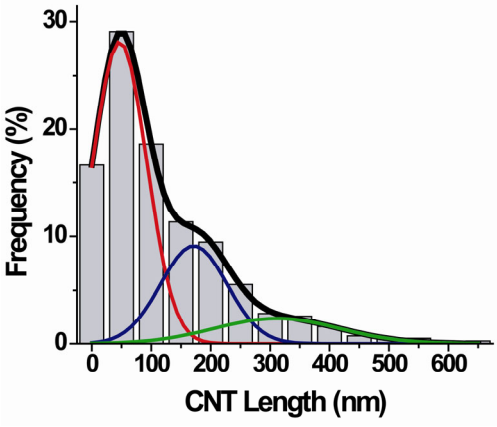


**Figure 3.2 Length distribution of CNTs wrapped with $(GT)_{30}$ oligonucleotide.** The average length of CNT–DNA measured from AFM images is 144 ± 112 nm (n > 800), and Gaussian fitting shows a trend to three different lengths (47 ± 45 nm, 172 ± 56 nm, and 311 ± 105 nm).

AFM imaging reveals a regular pattern on the CNT–DNA surface[6] consisting of peaks and valleys in height along the length of each tube, as well as corresponding shifts in the phase of the cantilever oscillation. This uniform pattern was observed along the entire length of all DNA-wrapped CNTs (Figure 3.3). The nanotube height above the mica substrate was 1.2 ± 0.2 nm at the peaks and 0.8 ± 0.2 nm at the valleys comprising the surface pattern. The width of the peaks along the CNT surface was 12 ± 5 nm, and the pitch (i.e., peak-to-peak distance) was 14 ± 5 nm. For comparison, CNT–$(GT)_{30}$ made from HiPco CNTs (which have a larger diameter than CNTs produced via CoMoCAT[10, 14]) have an average height of ~2 nm and pitch of ~18 nm.[6] Along with CNT–DNA, images show globular objects attributed to carbonaceous impurities from the CNT source material[15] (Figure 3.3A).

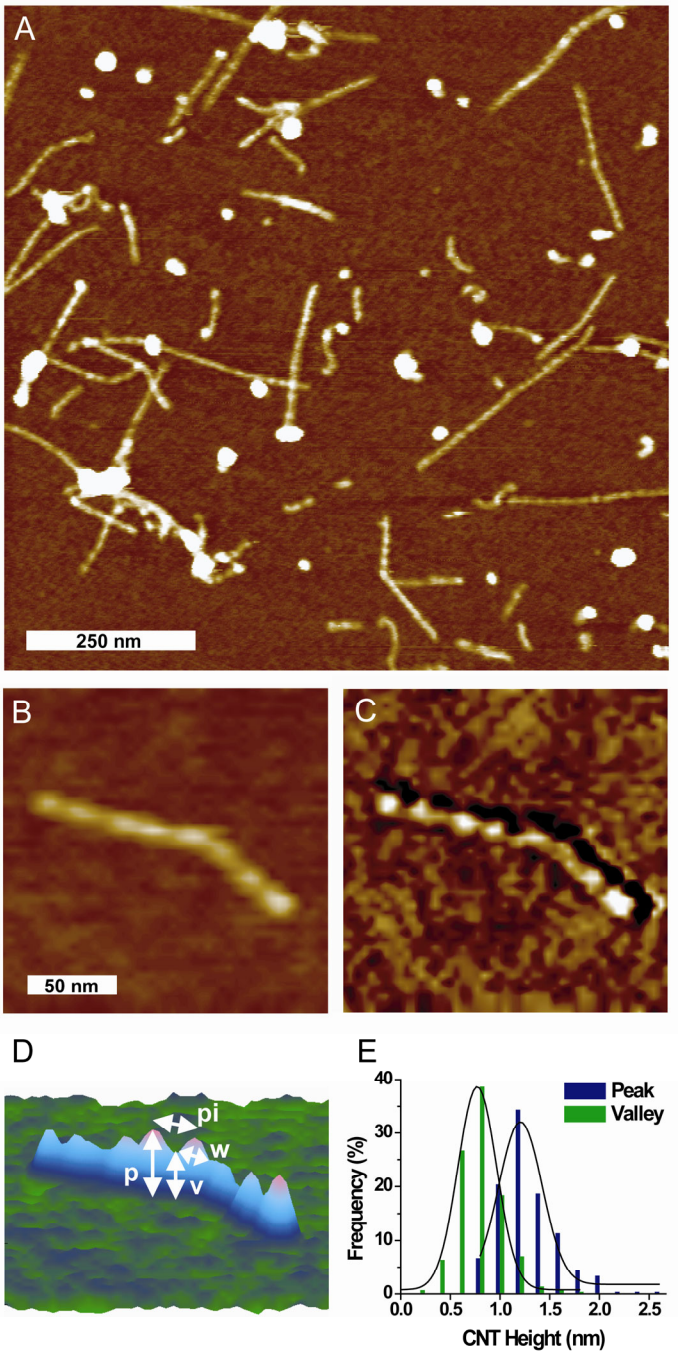


**Figure 3.3 AFM images of CNTs wrapped with $(GT)_{30}$ oligonucleotide.** (A) Height image with 5-nm scale showing several DNA-wrapped nanotubes. (B) Height image with 5-nm scale, (C) phase image with 25° scale, and (D) 3D representation with 1.7-nm scale indicating the peak height (p), valley height (v), peak width (w), and pitch (pi) measurements of one representative CNT–DNA. (E) Distributions of nanotube height measurements at peaks and valleys (n = 300 CNTs).

**Effect of the DNA Sequence.** The $(GT)_{30}$ sequence was studied because of a previous report modeling CNT–$(GT)_{30}$ as a special case, giving rise to a much more uniform AFM surface pattern than CNTs wrapped with other sequences.[6] For comparison to $(GT)_{30}$-wrapped CNTs, we imaged CNTs wrapped with an entirely thymine sequence of the same length, $T_{60}$. Under our AFM conditions, we observed a regular surface pattern for CNT–$T_{60}$. This pattern was indistinguishable from that of CNT–$(GT)_{30}$ and similarly prevalent along the lengths of the CNTs (Figures 3.4, 3.5). The CNT–$T_{60}$ pitch (14 ± 5 nm) and peak width (12 ± 5 nm) along the nanotube were identical to that of CNT–$(GT)_{30}$.

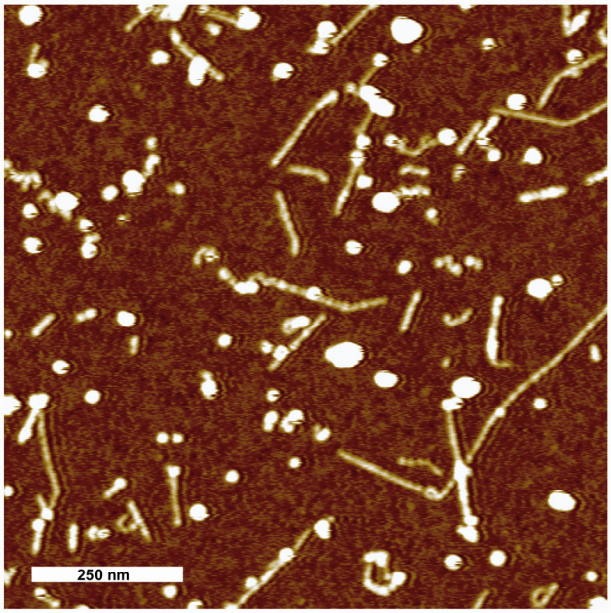


**Figure 3.4 AFM height image of CNTs wrapped with $T_{60}$ oligonucleotide.** Image shows the surface pattern along the length of the CNTs and its prevalence (5-nm scale).

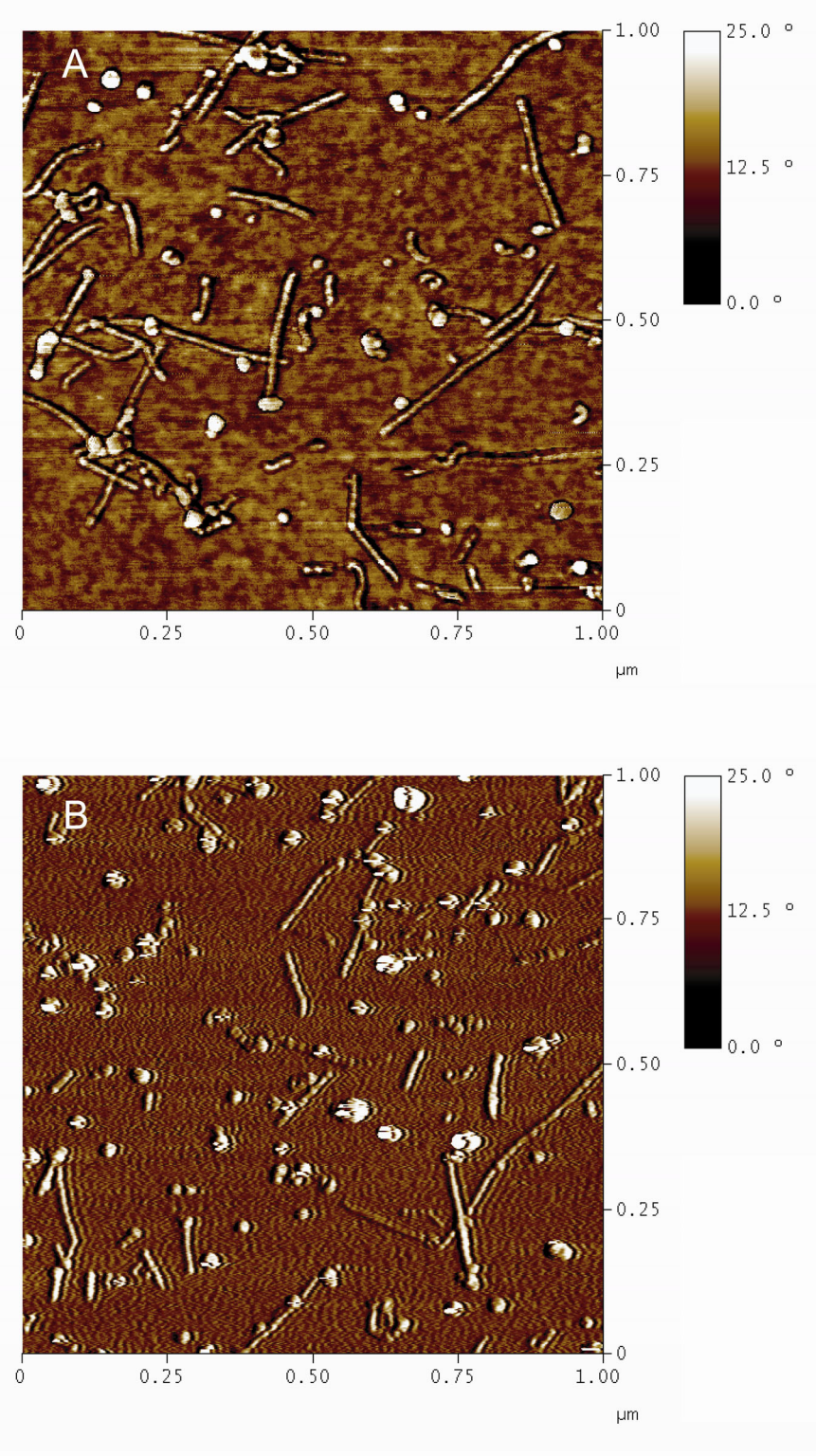


**Figure 3.5 AFM phase images of CNTs wrapped with (A) $(GT)_{30}$ and (B) $T_{60}$ oligonucleotide.**

**Effect of the DNA Length.** CNTs wrapped with 30-, 60-, and 120-mer oligonucleotides of entirely thymine bases were compared to examine the effect of oligonucleotide length on CNT–DNA structure. Images of CNT–$T_{30}$ and CNT–$T_{120}$ revealed a surface pattern similar to that observed for the two 60-mers, $(GT)_{30}$ and $T_{60}$ (Figure 3.6). The peak width and pitch measurements of CNTs wrapped with $T_{30}$, $T_{60}$, $T_{120}$, and $(GT)_{30}$ were all within one standard deviation (Figure 3.6G, H). The pitch (13 ± 5 nm) and peak width (13 ± 4 nm) of CNT–$T_{120}$ were similar to that of the 60-mer-wrapped CNTs, while the pitch (10 ± 4 nm) and peak width (11 ± 4 nm) of CNT–$T_{30}$ were slightly shorter.

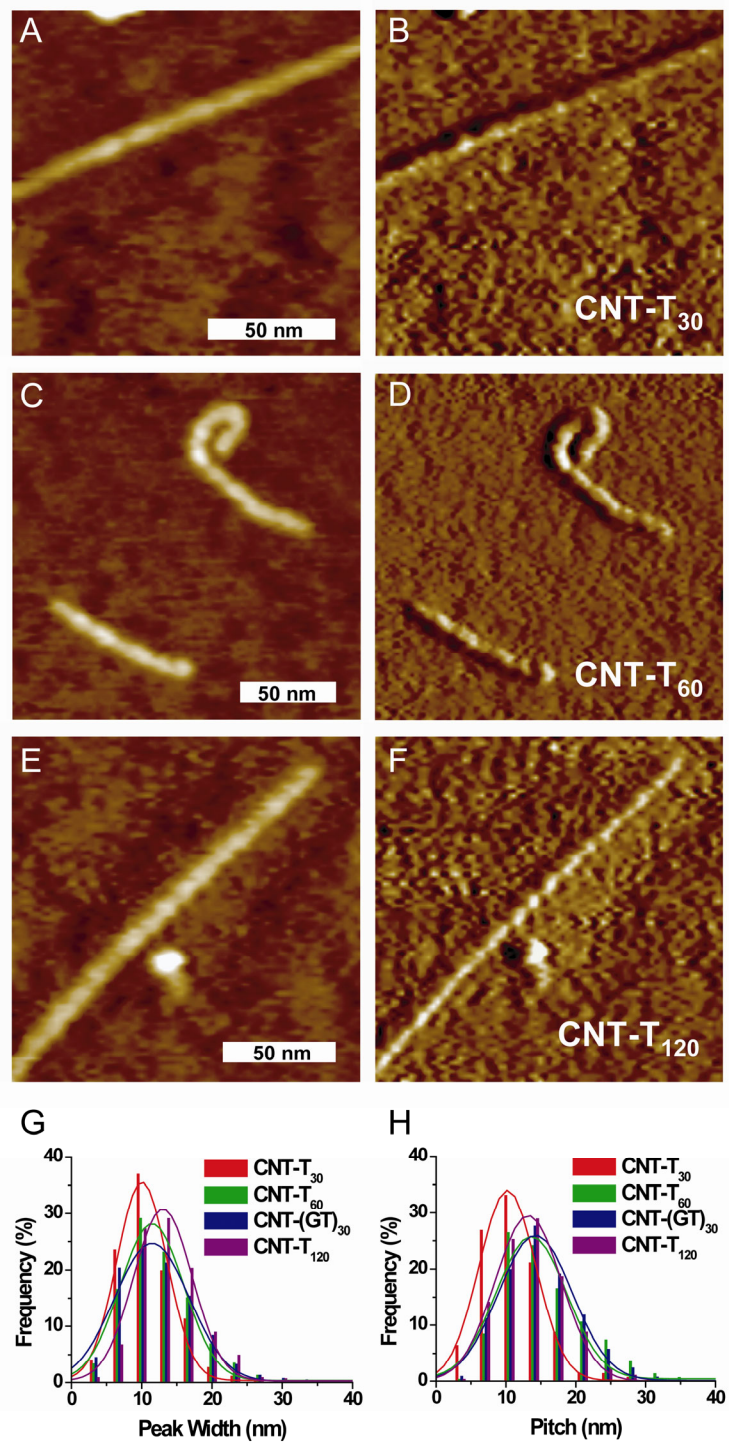


**Figure 3.6 AFM images of CNTs wrapped with oligonucleotides of varying length.** (A–F) Height (left) and phase (right) images of representative CNTs wrapped with thymine oligonucleotide sequences of 30-, 60-, and 120-base length (shown with 5-nm height scales and phase scales of 8°, 25°, and 10°, respectively). (G) Peak width along the CNT surface and (H) pitch (peak-to-peak distance) distributions for CNTs wrapped with $T_{30}$, $T_{60}$, $(GT)_{30}$, and $T_{120}$ oligonucleotides ($n > 500$).

**Quantum Dot Labeling of the Wrapping DNA.** To identify the location of oligonucleotides on CNT–DNA, we sought to label the wrapping DNA in a manner recognizable by AFM. We attached mercaptoacetic acid-stabilized QDs (of CdSe core and ZnS shell) having ~2.4-nm diameter to CNTs wrapped with thiolated oligonucleotide (Figure 3.7).

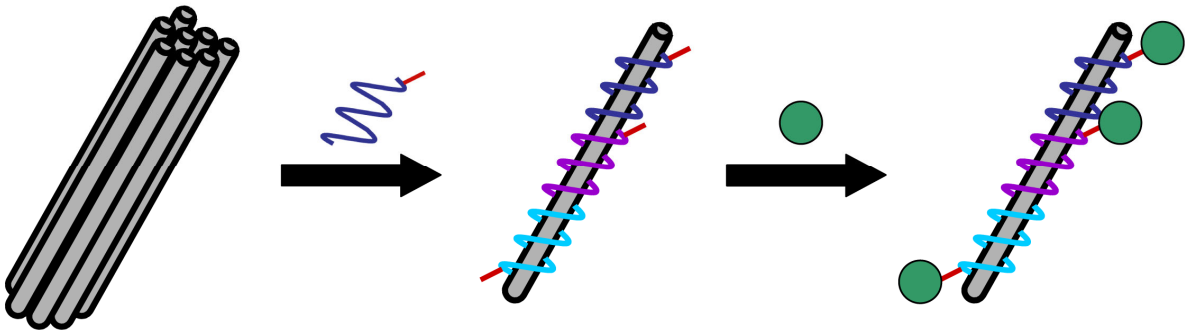

**Figure 3.7 QD labeling procedure to identify the location of DNA on CNT–DNA.** CNTs were individually wrapped with thiolated oligonucleotide and subsequently incubated with QDs that bind to thiol groups on the DNA. Thiol modifications to the oligonucleotide are shown as red tags; QDs are shown as green spheres.

The resulting CNT–DNA–QD conjugates were stable in aqueous solution, and the QDs provided a convenient size-marker in AFM images to identify the location of DNA on CNTs (Figure 3.8). The DNA-bound QDs were observed to be positioned along the regular surface pattern of CNT–DNA, localized on the peaks in height.

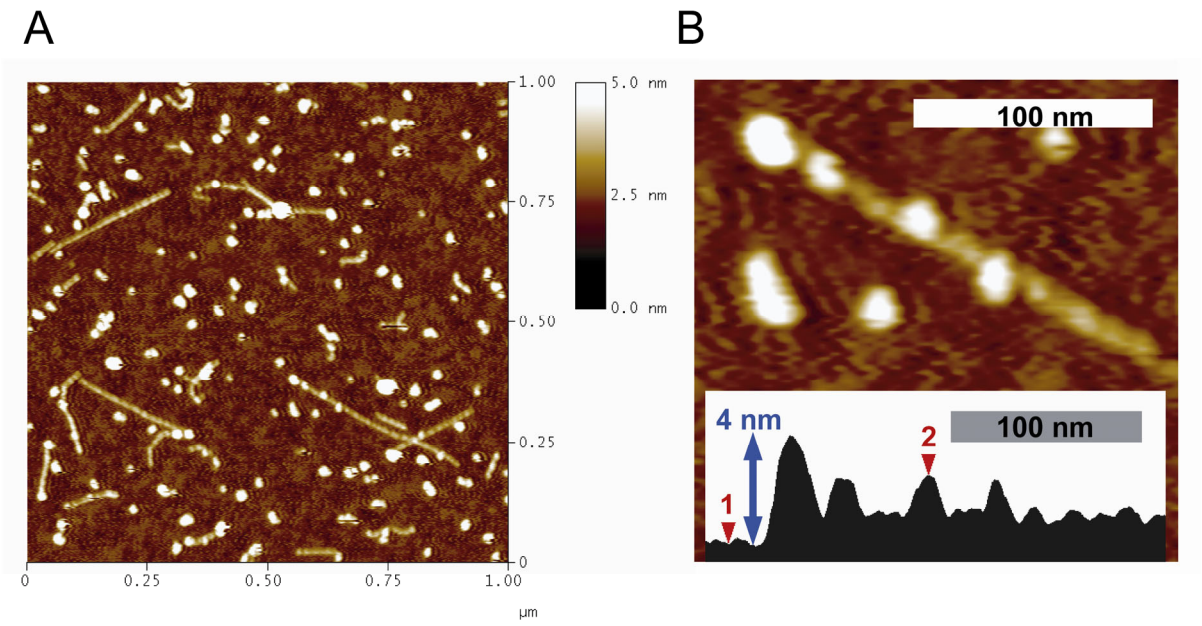


**Figure 3.8 AFM image of QD-labeled CNT–DNA.** (A) Height image of CNTs dissolved with thiolated oligonucleotide (CNT–thiol) then incubated with QDs in solution for 24 h at RT. (B) One representative CNT–thiol labeled with QDs (5-nm height scale). Inset: cross-section of this nanotube, where position 1 indicates the mica substrate and position 2 indicates a QD bound to CNT–DNA.

To ensure that QD binding was selective for the thiol groups on the wrapping DNA, CNTs were wrapped with $(GT)_{30}$ modified to contain zero (CNT–biotin), one (CNT–thiol), or two (CNT–dithiol) thiols per strand then incubated in solution with (or without) QDs (24 h, RT). AFM images were collected, and the number of QD-sized objects (round objects of height > 1 nm) observed per nanotube was counted; this count included both QDs and the carbonaceous impurities that were observed in all CNT–DNA images. The average number of QD-sized objects observed per CNT for each experimental group is shown in Figure 3.9.

The number of objects/CNT for the non-thiolated control (CNT–biotin) in the presence of QDs (0.4 ± 0.1) was *not* significantly different from that found in the absence of QDs (0.4 ± 0.05). However, when one thiol was present per strand of the wrapping DNA (CNT–thiol), the number of objects/CNT in the presence of QDs (0.9 ± 0.3) was significantly

increased compared to that in their absence (0.4 ± 0.1). A significant increase was likewise observed for CNTs wrapped with oligonucleotides containing two thiols per strand (CNT–dithiol, which had 0.4 ± 0.1 objects/CNT in the absence of QDs, but 1.2 ± 0.2 objects/CNT in their presence). Furthermore, significantly more objects were observed per CNT for CNT–dithiol than for CNT–thiol. The data were also analyzed in this manner with respect to the location of objects on the CNT; the significant differences reported above were also true when considering only those objects observed at the nanotube ends or only objects along the CNT sidewalls.

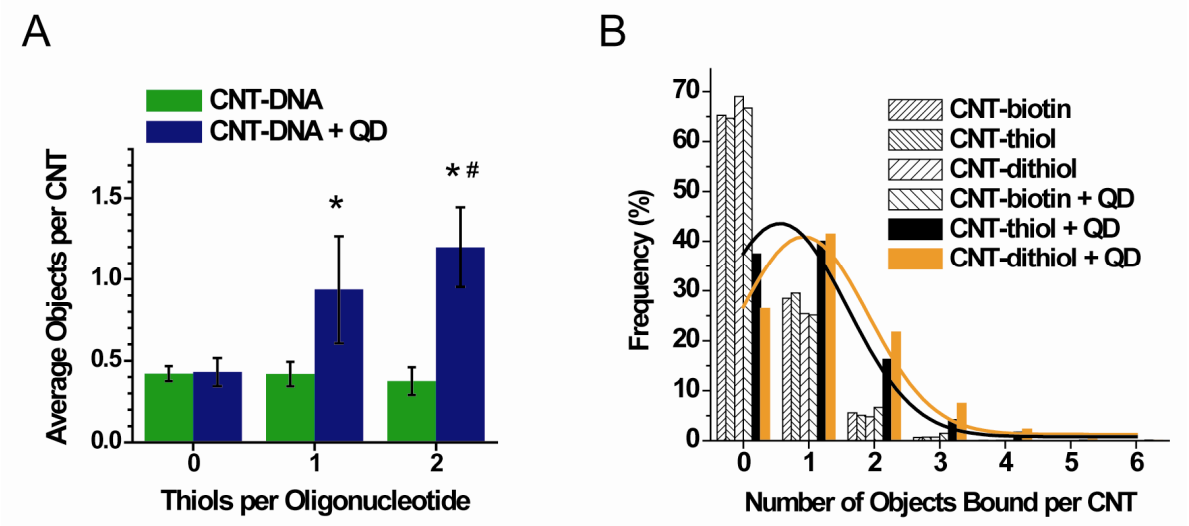


**Figure 3.9 Selective binding of QDs to the DNA on CNT–DNA.** (A) Average number of QD-sized objects observed per nanotube for CNTs wrapped with DNA containing 0 (CNT–biotin), 1 (CNT–thiol), or 2 (CNT–dithiol) thiols per strand (with and without QD incubation). Data are the average of three experiments (n = 500 CNTs per group, per experiment); error bars show the standard deviations of the three experiments. Significant increases compared to 0 thiols (*) and to 1 thiol (#) are indicated for data in the presence of QDs. (B) Distribution of the number of QD-sized objects observed per nanotube for CNT–biotin, CNT–thiol, and CNT–dithiol with and without QD incubation (n = 1500 CNTs per group).

A regular spacing was observed between QDs on the CNT surface (Figure 3.10). For CNTs wrapped with 5′-modified 60-mers, QDs bound near each other on the same nanotube showed a regular spacing of ~40 nm (43 ± 20 nm for the shortest Gaussian population of QD-to-QD distances), suggesting a 40-nm interval along the nanotube between the thiol groups of different oligonucleotides. The QD-to-QD distance on CNTs wrapped with 5′-thiolated 120-mers was ~60 nm (63 ± 26 nm for the shortest Gaussian population of QD-to-QD distances), suggesting a larger spacing between thiol groups of the modified 120-mers.

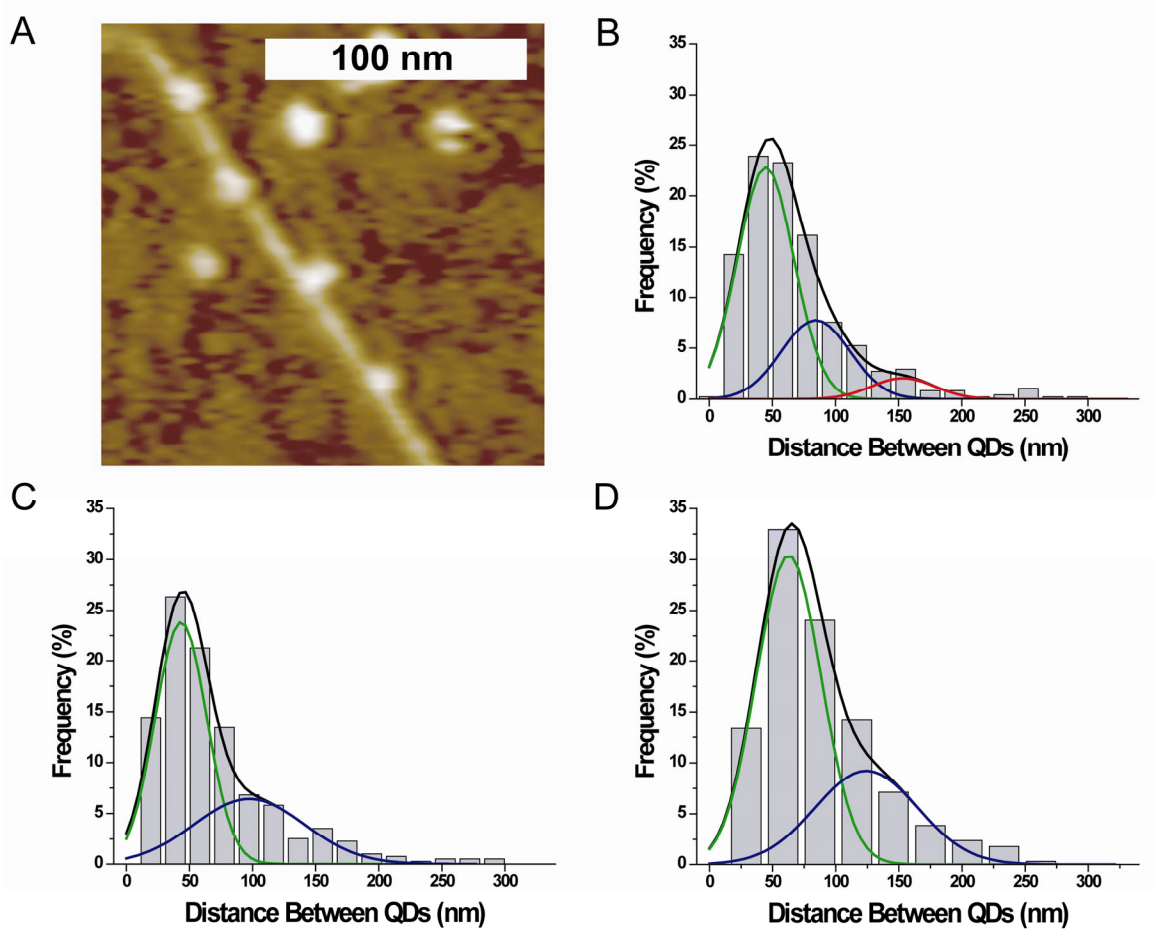


**Figure 3.10 Distance between QDs on CNT–DNA.** (A) Height image of a CNT wrapped with monothiolated 60-mers and incubated with QDs. (B–D) Distributions of the distances between QD-sized objects found on individual CNTs wrapped with (B) dithiolated 60-mers (CNT–dithiol: 45 ± 22, 84 ± 27, 153 ± 25 nm), (C) monothiolated 60-mers (CNT–thiol: 43 ± 20, 97 ± 88 nm), and (D) monothiolated 120-mers (CNT-5′-thiol-$(GT)_{60}$: 63 ± 26, 124 ± 41 nm) after incubation with QDs (n > 300).

**Comparison to Surfactant-Suspended Carbon Nanotubes.** To study CNT structure without the presence of DNA, we suspended CNTs in water containing 1% SDS (which was necessitated by the aggregated state of as-produced CNTs) and imaged the resulting CNT–SDS material via AFM. Like ssDNA, SDS is an amphiphilic molecule capable of dispersing CNTs in water;[16] however, the structure of SDS surfactant on CNTs differed from that of DNA on CNTs (Figures 3.11–3.13).

To investigate whether surfactant was removed from the nanotubes during AFM sample preparation, we compared our method employing brief rinsing of the deposited CNT–SDS to a preparation with extensive (10-fold increased) rinsing. The percentage of uncovered nanotube surface ranged from 5 to 39% in both procedures, and the extent of rinsing did not cause a statistical difference in the mean percentage of uncovered CNT.

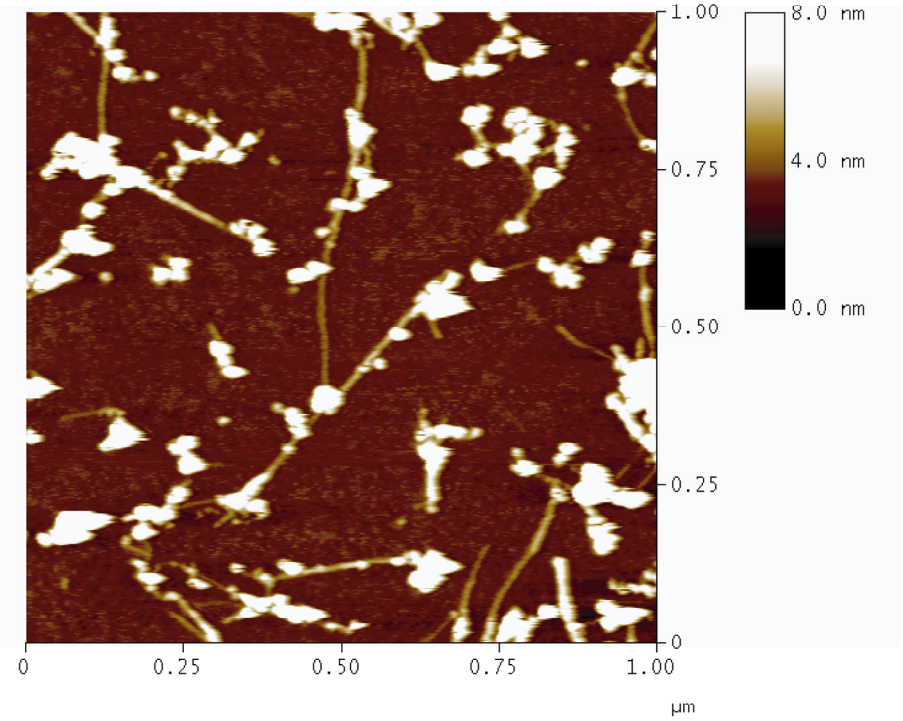


**Figure 3.11 AFM height image of CNTs suspended by SDS (in the absence of DNA).**

While SDS was sometimes ordered into a pattern along the CNT, irregular surface coverage was also observed. Patterned organization of SDS was only observed on short (~100 nm or less) CNTs or segments of CNTs (Figure 3.12A, C) and was less common than irregular organization (Figure 3.12B, D); patterned structure accounted for only ~25% of surfactant coverage on CNTs.

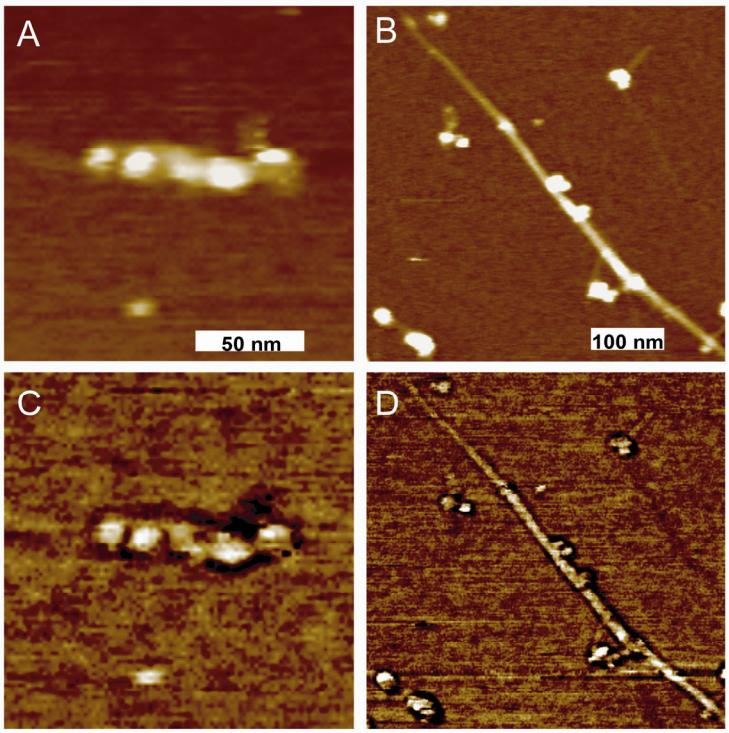


**Figure 3.12 AFM images of the different structures observed for CNT–SDS.** Height (top, 5-nm scale) and phase (bottom, 10° scale) images of CNTs exhibiting (A, C) patterned and (B, D) irregular SDS coverage. These two nanotubes were observed in the same 1-μm AFM image.

The pitch (18 ± 6 nm) and peak width (19 ± 5 nm) of this surfactant pattern were larger than that of CNT–DNA ($n > 600$). The prominent CNT–SDS peaks were taller (3.8 ± 1.0 nm) and more varied in height compared to CNT–DNA, and valley measurements were taller (1.4 ± 0.7 nm) than the bare CNT, indicating the presence of SDS even at the valleys of the pattern ($n = 300$). While no regions of uncovered CNT were observed for CNT–DNA, areas of bare CNT were present on CNT–SDS tubes exhibiting irregular structures (Figures 3.12B, D; 3.13). The CNT height at these uncovered regions was 0.8 ± 0.3 nm ($n = 300$), which agrees with both the valley heights observed for CNT–DNA and the reported diameter of CoMoCAT CNTs.[10]

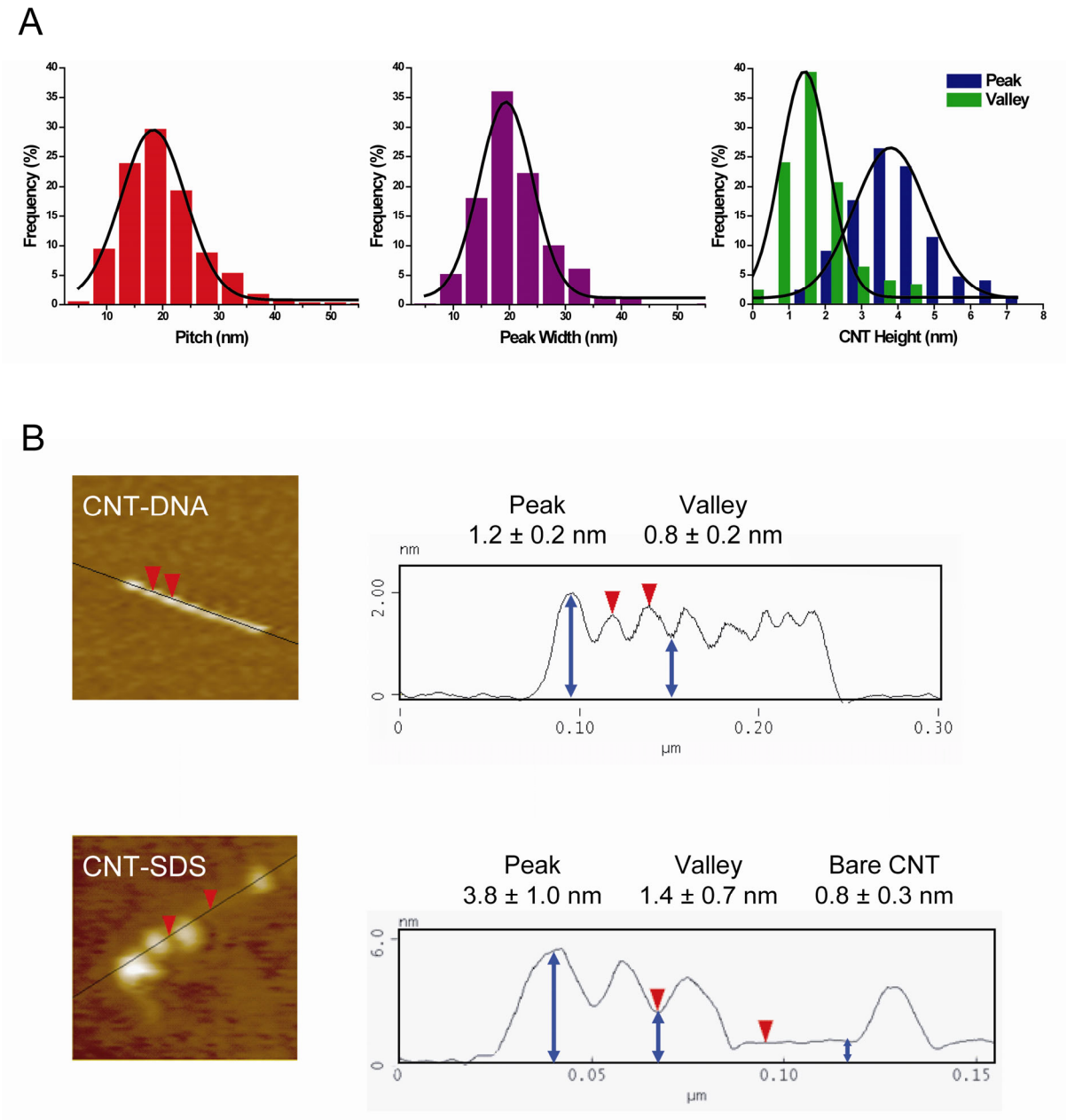


**Figure 3.13 Comparison of CNT–DNA to CNT–SDS.** (A) Distributions of the pitch (18 ± 6 nm, n > 600), peak width (19 ± 5 nm, n > 600), and height at the peaks (3.8 ± 1.0 nm, n = 300) and valleys (1.4 ± 0.7 nm, n = 300) of the surface pattern of CNTs suspended by SDS (without DNA present) that displayed patterned organization. (B) Cross-sections of a typical CNT–DNA and CNT–SDS, contrasting the average (± standard deviation) heights of their surface features.

## 3.5 Discussion

**Location of DNA in DNA-Wrapped Carbon Nanotubes.** Variation in AFM phase images is caused by differing interactions between the sample and the AFM tip. Therefore, the observation of a regular surface pattern along CNT–DNA in phase as well as height images suggests that the pattern is formed by different materials, CNT and DNA. The height at the valleys of the pattern is consistent with unwrapped CoMoCAT CNTs, which are on average 0.81 nm in diameter.[10] The difference between the peak and valley heights of the pattern (~0.4 nm) is attributed to a single layer of ssDNA, in agreement with the predicted height of ~0.5 nm for π-stacked ssDNA on a CNT.[2, 4] These height data suggest that oligonucleotides interact with the CNT sidewalls, forming peaks where they are bound and leaving valleys whose heights reflect the bare nanotube. A single population was observed in the distribution of CNT–DNA peak heights (Figure 3.3E), suggesting that DNA is only present in this single-layer coverage on the CNT surface. Assignment of the regular CNT–DNA surface pattern to the presence of DNA is supported by the absence of the pattern in images of surfactant-suspended CNTs.

This analysis of the origin of the CNT–DNA AFM pattern is corroborated by QD labeling of the DNA. DNA-bound QDs were positioned along the regular surface pattern of the nanotube, localized on the peaks in height. Nonspecific binding of QDs to CNT–DNA was not appreciable, and QDs were observed to bind selectively to thiolated DNA both at the nanotube ends and along the sidewalls, identifying the location of oligonucleotide along the entire CNT. *This observation is the first direct evidence of the oligonucleotide location on DNA-wrapped CNTs and suggests that the AFM surface peaks result from the DNA.* The persistence of the surface pattern along the entire CNT (regardless of the length of the

wrapping DNA) without regions of unwrapped nanotube suggests that the CNT–DNA has nearly complete DNA coverage. The oligonucleotides must be closely arranged along the CNT, with more oligonucleotides needed per CNT for shorter DNA (or for longer CNTs). This close arrangement of DNA strands likely serves to minimize the unfavorable interaction of the hydrophobic CNT surface with the aqueous solution.

These findings have important implications for future applications of the CNT–DNA nanomaterial. For instance, the lack of unwrapped CNT regions may serve to limit nonspecific binding when CNT–DNA is employed in bio-sensing. In schemes seeking to derivatize the DNA, the high coverage of oligonucleotides would allow for a high density of functional moieties per CNT.

**Modeling of DNA-Wrapped Carbon Nanotube Structure.** The Microscope Simulator program[12] was employed to build models of the DNA structure on a CNT and to simulate the height image that would be produced for each model by an AFM tip. CNTs and ssDNA can interact in a stable, organized manner by helical wrapping of ssDNA around CNTs.[1-5, 17] To model this interaction, a CNT (of 0.8-nm diameter) was wrapped with a helical pipe (of 0.5-nm diameter, tangent to the CNT) representing the ssDNA. We considered situations in which each peak in CNT–DNA height comprising the regular AFM pattern could arise from (1) each turn of helically wrapped DNA around the CNT, or (2) each oligonucleotide on the CNT. The evidence needed to evaluate the appropriateness of these models was provided by images of CNTs wrapped with different lengths of DNA.

In the case of each turn of helically wrapped DNA around the CNT generating one peak in the AFM height image, the pitch of the AFM surface pattern is equal to the wrapping pitch of the DNA (and the peak width is the width of each DNA turn on the top of the CNT).

To model this structure, a CNT was helically wrapped by 60-mer oligonucleotides with 14-nm pitch (equivalent to the pitch observed by AFM). A 60-mer at this pitch was calculated to turn ~2.8 times around the CNT, covering a nanotube length of ~40 nm (refer to Experimental Section). This CNT length is considerably less than the average length of CNTs in our sample, implying that several oligonucleotides (3–4 oligonucleotides for a CNT of average length) are bound per CNT in an end-to-end manner. These oligonucleotides must be closely arranged along the CNT to produce the observed AFM pattern, which covers the entire CNT without any unwrapped areas.

Simulation of a CNT covered by two 60-mers positioned end-to-end with 14-nm wrapping pitch generated an AFM image consistent with the regular surface pattern observed experimentally (Figure 3.14A). In this model, wrapping with longer oligonucleotides means more of the CNT is covered per strand, but the same total length of CNT can be covered by wrapping with multiple short oligonucleotides closely arranged along the CNT. This effect can be seen in Figure 3.14A by viewing the two 60-mers composing the DNA wrap as a single 120-mer or as four adjacent 30-mers; each instance produces the same AFM surface pattern. Therefore, the lack of a dramatic effect of oligonucleotide length on the AFM surface pattern (of CNT–$T_{30}$, –$T_{60}$, and –$T_{120}$) supports the assignment of one AFM surface peak to each turn of the wrapped DNA.

This assignment is corroborated by the regular spacing of ~40 nm observed between the centers of QDs bound near one another on CNTs wrapped by monothiolated 60-mers because each 60-mer at 14-nm wrapping pitch was calculated to cover a CNT length of ~40 nm. Our observation of ~60-nm spacing between QDs on CNTs wrapped by thiolated 120-mers is consistent with the expected ~80-nm spacing due to the large variation (± 26 nm)

introduced by wrapping pitch variation and the size of the QDs. Comparison of the QD spacing measurement to the length of a wrapped oligonucleotide assumes oligonucleotide attachment to the center of each QD; variation in the actual position of attachment limits the usefulness of the QD as an exact marker for the end of the oligonucleotide. The larger spacing observed between QDs on CNTs wrapped with 120-mers compared to 60-mers supports the model proposed in Figure 3.14A.

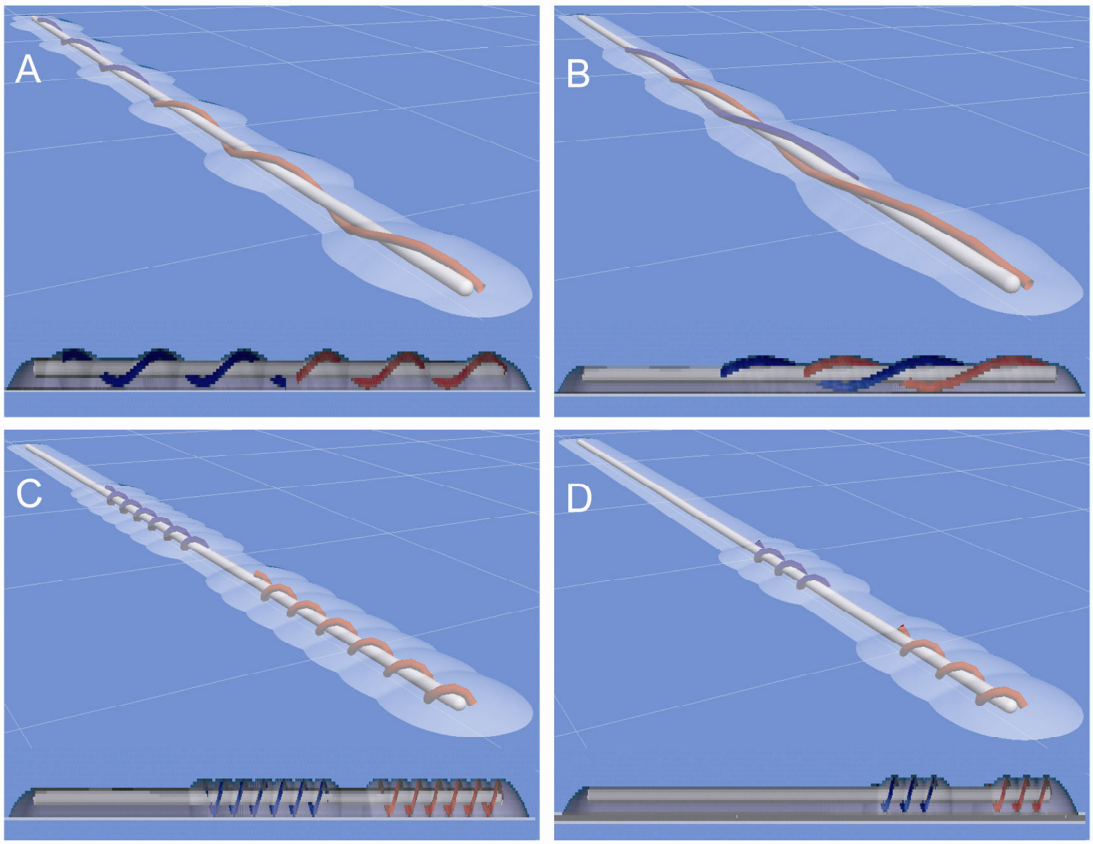


**Figure 3.14 Simulated AFM images of CNT–DNA models.** Models show a CNT of 0.8-nm diameter and 80-nm length. (A) Each turn of the DNA around the CNT (14-nm pitch) generates one surface peak in the AFM image; the DNA is colored to show two 60-mers, but the same image results from wrapping with one 120-mer or four adjacent 30-mers. (B) Each turn of the DNA around the CNT (28-nm pitch) generates one surface peak in the AFM image; the colors indicate two interlaced 60-mers offset from each other by 14 nm. (C) Each oligonucleotide generates one surface peak in the AFM image; the colors indicate two 60-mers at 3.4-nm wrapping pitch. (D) Case shown in C for two 30-mers.

Two interlaced DNA helices with 28-nm wrapping pitch that are offset from each other by 14 nm would also result in an AFM surface pattern with 14-nm pitch (Figure 3.14B). However, our data and recent molecular dynamics simulations revealing the decreased stability of larger DNA wrapping pitches[3] suggest that adjacent oligonucleotides on a CNT do not helically intertwine. The larger wrapping pitch of the DNA in Figure 3.14B results in a less distinct AFM surface pattern than that produced by the non-interlaced model in Figure 3.14A, and instances where the helices are not offset by exactly 14 nm would introduce greater variability in the AFM pitch than we observed experimentally.

An alternate explanation for the CNT–DNA surface pattern observed via AFM is that each height peak results from one bound oligonucleotide, making the pitch equal to the distance between the centers of adjacent oligonucleotides and the peak width equal to the length of one oligonucleotide. This case requires DNA wrapping with too small a pitch for the individual turns to be distinguished by the AFM tip and gaps between oligonucleotides to produce a regular pattern in CNT–DNA height. The model in Figure 3.14C meets these requirements and was constructed with the same wrapping pitch as in a DNA double helix (3.4 nm, allowing a 60-mer to make 6.4 turns around the CNT and cover a CNT length of ~20 nm). This model produces an AFM image with a periodic variation in height. However, the model predicts a dramatic effect of the oligonucleotide length, where the peak width of CNT–$T_{120}$ would be double that of CNT–$T_{60}$ and quadruple that of CNT–$T_{30}$ (and the pitch would also vary); these effects are shown in Figure 3.14C, D. No such length effects were observed experimentally, supporting the wrapping model in Figure 3.14A over that in Figure 3.14C, D.

Overall, our AFM measurements and modeling suggest that the observed pitch of the CNT–DNA surface pattern in AFM images corresponds to the pitch of the wrapping DNA for oligonucleotides closely arranged, but not intertwined, on the CNT surface. To cover a CNT of average length requires 3–4 60-mers bound end-to-end along the CNT. This ratio of oligonucleotide to CNT is supported by calculation of the concentrations of DNA and CNT in our CNT–DNA (refer to Chapter 2).

Since multiple oligonucleotides are present per CNT, the pitch distribution may include not only turn-to-turn measurements of wrapped oligonucleotides, but any distances between two adjacent oligonucleotides. This occurrence may be responsible for the slightly shorter pitch measurement of CNTs wrapped with the shortest oligonucleotide (CNT–$T_{30}$). As the 30-mer can only execute one complete turn around the CNT (1.8 turns versus 2.8 turns for $T_{60}$ and 5.9 turns for $T_{120}$), its pitch measurement would be the most influenced by measurements of the spacing between oligonucleotides. Alternatively, the inability of the 30-mer to make more than one complete turn around the CNT might favor a shorter wrapping pitch to increase the energetic stability of the hybrid (as suggested by molecular dynamics work[3]). It is likely that spacing measurements do not have a substantial impact on AFM pitch measurements due to the narrow pitch distribution (± 4 or 5 nm) observed, which indicates the regularity of the DNA organization along the CNT.

Modeling predicts an optimum DNA wrapping pitch for any given CNT–DNA hybrid, dependent on the physical and electronic characteristics of the CNT.[2] The CoMoCAT CNTs used to prepare our CNT–DNA samples have a narrow distribution of diameters and (*n,m*) types,[10] which is reflected in the narrow distribution we observed for AFM pitch measurements. The DNA wrapping pitch of individual CNT–DNA hybrids can

be determined through measurement of the surface pattern pitch in AFM images. This connection is of practical importance in the development of ion exchange chromatography as a means to separate CNT–DNA according to CNT type,[6, 7] since the DNA wrapping pitch is the primary factor in controlling the separation.[5]

**Surface Pattern on DNA-Wrapped Versus Surfactant-Suspended Carbon Nanotubes.** No significant impact of the oligonucleotide sequence on the structure of CNT–DNA was observed for the 60-mers studied, $(GT)_{30}$ and $T_{60}$. This finding is consistent with a report that CNTs suspended by a random, long ssDNA sequence exhibited periodic wrapping structure[17] and with molecular dynamics results indicating that the forces driving both the DNA-to-CNT adhesion and the helical wrapping are sequence-independent.[3] However, although the wrapping oligonucleotide sequence does not affect the CNT–DNA hybrid structure observed via AFM, it does play a role in determining CNT–DNA properties. Notably, CNTs wrapped with different DNA sequences vary in their ability to be sorted (according to electronic character and diameter) by ion exchange chromatography.[6] Sorting via this technique is attributed to differences in the effective linear charge density (which is sensitive to CNT electronic character and diameter) of CNT–DNA hybrids formed from different (*n,m*) types of CNTs.[5, 6] CNTs wrapped with oligonucleotides of alternating GT sequence produce the best separation (including better separation compared to T sequences),[6] but our AFM observations suggest that this difference in properties is not the result of a difference in DNA wrapping structure. Others have suggested that the varying success of different wrapping sequences in sorting CNT–DNA may result from sequence-dependent effects that do not impact CNT–DNA structure (such as solvation or interactions between nucleotides).[3]

The uniformity of the CNT–DNA pattern contrasts with the variety of the structures observed for CNT–SDS. While conditions such as the solution surfactant concentration and temperature are expected to affect CNT–SDS organization, nanotubes from the same solutions displayed different surfactant structures (Figure 3.12). The representative CNT in Figure 3.12B, D bears irregularly adsorbed masses of surfactant, along with smooth surfactant layers of varying height. These smooth layers suggest an organization based upon either cylindrical micelle encapsulation of the CNT[16, 18] or wrapping by a hemicylindrical micelle.[19] In contrast, the pattern observed for nanotubes such as that in Figure 3.12A, C suggests a single-file adsorption of surfactant aggregates. While these types of CNT–SDS displayed more consistent organization, the irregular structures predominated.

Surfactants offer advantages in CNT separation procedures due to their low cost, diverse properties, and reversible adsorption to CNTs. An effective technique for sorting surfactant-dispersed CNTs according to CNT electronic type and diameter is density-gradient ultracentrifugation.[20] However, effective separation is dependent upon the formation of consistent surfactant structures that only vary (in orientation, packing density, hydration, etc.) according to the properties of each individual CNT. Therefore, careful choice of surfactant and preparation of suspensions to give individually dispersed CNTs with consistent surfactant organization are essential to successful CNT sorting. The inconsistent structures we observed for CNT–SDS may explain their poor separation performance[20] in density differentiation experiments compared to CNTs dispersed with bile salts. In contrast to the CNT–SDS structure, the uniform organization of CNT–DNA suggests an advantage of DNA wrapping in CNT sorting strategies.

**DNA-Wrapped Carbon Nanotube–Quantum Dot Conjugates.** The significant increase observed in the number of objects per CNT upon QD incubation only when thiols were present on the wrapping DNA suggests that QD binding to CNT–DNA occurs selectively at the thiol groups. The co-incubation of QDs and CNTs wrapped by thiolated DNA did not noticeably affect nanotube solubility; no CNT precipitation was observed over a period of several weeks. In contrast, attempts to label CNTs wrapped by biotinylated DNA with streptavidin (by adding a protein solution to CNT–biotin) resulted in immediate nanotube aggregation, with the degree of aggregation dependent upon the concentration of streptavidin added. In QD labeling experiments, on the other hand, we found oligonucleotides capable of interacting with both a QD and a CNT simultaneously. QD binding is assumed to occur when the thiolated terminus of the CNT-bound oligonucleotide binds to the QD ZnS shell and acts as a functionalized capping ligand, linking the QD to the CNT.

To compare the number of available thiol groups to the number of bound QDs, we calculated the approximate number of QDs bound per CNT (by subtracting the average number of QD-sized objects per CNT without QD incubation from that with QD incubation). This calculation gives a reasonable representation of the actual number of QDs/CNT due to the constant background of ~0.4 objects/CNT observed for all of the control groups (Figure 3.9A). After incubation with QDs, the non-thiolated (CNT–biotin) control had approximately zero (0.01) QDs/CNT, while CNT–thiol had 0.5 QDs/CNT, and CNT–dithiol had 0.8 QDs/CNT. Although 3–4 oligonucleotides were calculated to cover a CNT of average length, CNTs wrapped with monothiolated oligonucleotides had an average of only 0.5 QDs/CNT; therefore, at the concentrations of CNT–DNA and QDs used for AFM

imaging (an excess of QDs), we did not observe QDs bound to every thiolated oligonucleotide strand. This may result from the thiol groups of some wrapped oligonucleotides not being fully accessible to QDs in solution.

Both QDs and CNTs are envisioned for future applications such as biological imaging and sensing.[21-24] QDs and single-walled CNTs have been combined through covalent methods[25] and noncovalent strategies such as electrostatic interactions[26] and π-stacking.[27] Our QD labeling experiments demonstrate a new method for binding QDs to CNTs and suggest the advantage of modifying the noncovalently wrapped ssDNA of CNT–DNA to selectively attach QDs in a manner that avoids covalent modification of the CNT surface.

### 3.6 Conclusions

Measurements and modeling of the regular AFM pattern observed along CNT–DNA suggest that the hybrids are composed of oligonucleotides closely arranged end-to-end in a single layer along the entire nanotube surface, with each turn of the wrapped DNA generating one surface peak in the AFM images. Supporting this structural model, no significant impact of the oligonucleotide length was observed on the regular pitch of the surface pattern or on the width of the peaks along the CNT. QD labeling of CNTs wrapped with thiolated DNA identified the presence of DNA at the ends and along the entire sidewalls of the CNTs. This result and the prevalence of the CNT–DNA surface pattern imply nearly complete coverage of CNTs with DNA. The distance observed between QDs on a CNT was consistent with the CNT length calculated to be covered by one oligonucleotide wrapped at 14-nm pitch, further supporting our model. The stable CNT–DNA–QD conjugates may prove to be a useful material due to the tunable fluorescence of QDs, and the use of QDs to

label the DNA demonstrates the value of wrapping CNTs with modified oligonucleotides, which can confer desirable properties without covalently functionalizing (and thus altering the electronic properties of) the CNT. We observed no structural difference in the DNA wrapping pattern of CNTs solubilized with an alternating guanine–thymine DNA sequence versus an entirely thymine sequence, while the structure of CNT–DNA was found to be very different from that of CNTs suspended with SDS. Our findings of the DNA location and wrapping structure are expected to benefit the separation of CNT mixtures into homogenous samples, which is a vital step in the majority of the envisioned applications for CNTs.

## 3.7 References


1. Zheng, M.; Jagota, A.; Semke, E. D.; Diner, B. A.; McLean, R. S.; Lustig, S. R.; Richardson, R. E.; Tassi, N. G. *Nat. Mater.* **2003**, *2*, 338-342.

2. Manohar, S.; Tang, T.; Jagota, A. *J. Phys. Chem. C* **2007**, *111*, 17835-17845.

3. Johnson, R. R.; Johnson, A. T. C.; Klein, M. L. *Nano Lett.* **2008**, *8*, 69-75.

4. Enyashin, A. N.; Gemming, S.; Seifert, G. *Nanotechnology* **2007**, *18*, 245702-245712.

5. Lustig, S. R.; Jagota, A.; Khripin, C.; Zheng, M. *J. Phys. Chem. B* **2005**, *109*, 2559-2566.

6. Zheng, M.; Jagota, A.; Strano, M. S.; Santos, A. P.; Barone, P.; Chou, S. G.; Diner, B. A.; Dresselhaus, M. S.; McLean, R. S.; Onoa, G. B.; Samsonidze, G. G.; Semke, E. D.; Usrey, M.; Walls, D. J. *Science* **2003**, *302*, 1545-1548.

7. Zheng, M.; Semke, E. D. *J. Am. Chem. Soc.* **2007**, *129*, 6084-6085.

8. Bustamante, C.; Rivetti, C. *Annu. Rev. Biophys. Biomol. Struct.* **1996**, *25*, 395-429.

9. Park, S.-H.; Sposito, G. *Phys. Rev. Lett.* **2002**, *89*, 085501/1-3.

10. Bachilo, S. M.; Balzano, L.; Herrera, J. E.; Pompeo, F.; Resasco, D. E.; Weisman, R. B. *J. Am. Chem. Soc.* **2003**, *125*, 11186-11187.

11. Patolsky, F.; Gill, R.; Weizmann, Y.; Mokari, T.; Banin, U.; Willner, I. *J. Am. Chem. Soc.* **2003**, *125*, 13918-13919.

12. Varadhan, G.; Robinett, W.; Erie, D.; Taylor II, R. M. *SPIE* **2002**, *4665*, 116-124.

13. Sarma, R. H., ed. *Nucleic Acid Geometry and Dynamics*; Pergamon Press: Elmsford, 1980.

14. Bachilo, S. M.; Strano, M. S.; Kittrell, C.; Hauge, R. H.; Smalley, R. E.; Weisman, R. B. *Science* **2002**, *298*, 2361-2366.

15. Huang, X.; McLean, R. S.; Zheng, M. *Anal. Chem.* **2005**, *77*, 6225-6228.

16. O'Connell, M. J.; Bachilo, S. M.; Huffman, C. B.; Moore, V. C.; Strano, M. S.; Haroz, E. H.; Rialon, K. L.; Boul, P. J.; Noon, W. H.; Kittrell, C.; Ma, J.; Hauge, R. H.; Weisman, R. B.; Smalley, R. E. *Science* **2002**, *297*, 593-596.

17. Gigliotti, B.; Sakizzie, B.; Bethune, D. S.; Shelby, R. M.; Cha, J. N. *Nano Lett.* **2006**, *6*, 159-164.

18. Matarredona, O.; Rhoads, H.; Li, Z.; Harwell, J. H.; Balzano, L.; Resasco, D. E. *J. Phys. Chem. B* **2003**, *107*, 13357-13367.

19. Richard, C.; Balavoine, F.; Schultz, P.; Ebbesen, T. W.; Mioskowski, C. *Science* **2003**, *300*, 775-778.

20. Arnold, M. S.; Green, A. A.; Hulvat, J. F.; Stupp, S. I.; Hersam, M. C. *Nat. Nanotechnol.* **2006**, *1*, 60-65.

21. Barone, P.; Baik, S.; Heller, D. A.; Strano, M. S. *Nat. Mater.* **2005**, *4*, 86-92.

22. Heller, D. A.; Baik, S.; Eurell, T. E.; Strano, M. S. *Adv. Mater.* **2005**, *17*, 2793-2799.

23. Kam, N. W. S.; O'Connell, M.; Wisdom, J. A.; Dai, H. *Proc. Natl. Acad. Sci. USA* **2005**, *102*, 11600-11605.

24. Michalet, X.; Pinaud, F. F.; Bentolila, L. A.; Tsay, J. M.; Doose, S.; Li, J. J.; Sundaresan, G.; Wu, A. M.; Gambhir, S. S.; Weiss, S. *Science* **2005**, *307*, 538-544.

25. Banerjee, S.; Wong, S. S. *Nano Lett.* **2002**, *2*, 195-200.

26. Chaudhary, S.; Kim, J. H.; Singh, K. V.; Ozkan, M. *Nano Lett.* **2004**, *4*, 2415-2419.

27. Li, Q.; Sun, B.; Kinloch, I. A.; Zhi, D.; Sirringhaus, H.; Windle, A. H. *Chem. Mater.* **2006**, *18*, 164-168.

# Chapter 4

# Electrochemistry of DNA-Wrapped Carbon Nanotubes

## 4.1 Abstract

As part of the ongoing effort to describe electron transfer reactions of carbon nanotubes (CNTs), we studied the solution oxidation of DNA-wrapped carbon nanotubes in an electrochemical–chemical system. During metal-mediated cyclic voltammetry, oxidation of the solubilized CNTs by tris(2,2′-bipyridine)ruthenium(III) and similar electrogenerated oxidants completes a catalytic cycle that increases metal oxidative peak current compared to a voltammogram of the metal complex alone. We observed a greater increase in current at higher nanotube concentration, slower experimental scan rate, and higher metal redox potential. These observations were shown via digital simulation to be consistent with CNT oxidation involving rate constants on the order of $10^3$, $10^4$, and $10^5$ $M^{-1}s^{-1}$, which reflect the varying redox potentials of different valence band electrons within one CNT chiral type and within the distribution of CNT types present in our sample. The lowest observed CNT oxidation potential was between 460 and 645 mV vs. Ag/AgCl and, above this potential, the number of transferred electrons increased exponentially with the redox potential of the metal mediator. While an Os(III) oxidant with 645-mV redox potential oxidized CNTs by ~200 electrons per nanotube, a Ru(III) oxidant with 1080-mV redox potential oxidized CNTs by ~2000 electrons per nanotube. These findings suggest stronger oxidants shift the Fermi level deeper into the CNT valence band.

## 4.2 Introduction

**Cyclic Voltammetry.** The potential at which a molecule undergoes reduction or oxidation is its redox potential. This characteristic is often reported as the formal potential measured under particular conditions, $E^{0'}$ (which is equal to the standard potential, $E^0$, only when each chemical is present in its standard state, e.g., 1 M solutions). Since many molecules have more than two charge states, each redox potential is designated for a particular redox couple (i.e., the reduced and oxidized forms that are interconverted at that potential).

The oxidation or reduction of an analyte molecule can be studied through the electrochemical technique of cyclic voltammetry (CV). In the present work, CV is performed on aqueous solutions with sodium phosphate buffer serving as supporting electrolyte in a three-electrode cell. These electrodes are a semiconducting tin-doped indium oxide (ITO) coating on glass (as the working electrode), a Pt wire (as the auxiliary electrode), and a silver–silver chloride electrode (as the reference electrode). The potential between the working and reference electrodes is monitored by a potentiostat and controlled by passage of current between the auxiliary and working electrodes. In a CV experiment, the potential is scanned at a constant rate over a specified potential range, and the current versus potential is measured. Unless otherwise designated, all potentials in this work are reported versus the Ag/AgCl reference electrode.

To record a cyclic voltammogram (CV) of the reduced form of a redox couple, CV is performed by starting at a potential well negative (> ~250 mV) of its $E^{0'}$ and sweeping to a potential positive of $E^{0'}$. This oxidative sweep is illustrated for CV of the transition metal complex tris(2,2′-bipyridine)ruthenium(II), $Ru(bpy)_3^{2+}$, in Figure 4.1 (red). The potential is

then scanned in the reverse direction to perform the reductive sweep (blue). Peaks in current result from the oxidation of $Ru(bpy)_3^{2+}$ on the oxidative sweep and subsequent reduction of electrogenerated $Ru(bpy)_3^{3+}$ on the reductive sweep. For reversible redox couples, the peak separation is 57 mV (at 298.2 K) and the average of the oxidative and reductive peak potentials is the half-wave redox potential ($E_{1/2}$).[1] The $E_{1/2}$ calculated for the nearly reversible $Ru(bpy)_3^{3+/2+}$ couple is equal to its $E^{0'}$, assuming equivalent diffusion coefficients for the $Ru(bpy)_3^{2+}$ and $Ru(bpy)_3^{3+}$ species.[1]

CV for the $Ru(bpy)_3^{3+/2+}$ couple is an example of *direct* electrochemistry, where the electrons lost by $Ru(bpy)_3^{2+}$ and gained by $Ru(bpy)_3^{3+}$ are exchanged with the working electrode. The half-reactions $Ru(bpy)_3^{2+} \rightarrow Ru(bpy)_3^{3+} + e^-$ and $Ru(bpy)_3^{3+} + e^- \rightarrow Ru(bpy)_3^{2+}$ are *heterogeneous* electron transfer (ET) reactions designated "E" reactions in electrochemical notation. *Indirect* electrochemistry occurs when the electrode generates an oxidized or reduced species (in an E reaction) that can then participate in *homogeneous* chemical ET reactions denoted "C" reactions.

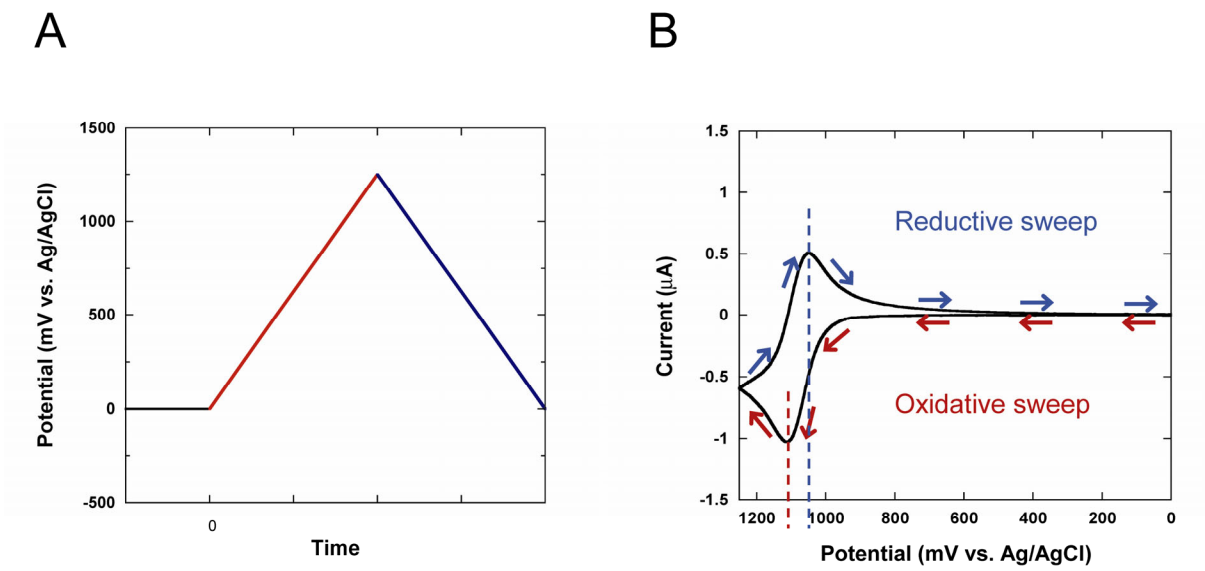


**Figure 4.1 The cyclic voltammetry experiment.** (A) The applied potential is swept at a constant rate in an oxidative direction (red) followed by a reductive direction (blue). (B) Cyclic voltammogram of $Ru(bpy)_3^{2+}$ in 100 mM sodium phosphate buffer, pH 7.0, showing the oxidative (~-1 μA) and reductive (~0.5 μA) peaks in current. The average of the two peak potentials (shown by the dashed red and blue lines) is the half-wave potential ($E_{1/2}$), which is ~1080 mV for $Ru(bpy)_3^{3+/2+}$.

**Metal-Mediated Electrochemistry.** The classical catalytic mechanism, denoted EC′ (1–2), is a useful means of studying the ET behavior of a redox couple whose direct electrochemistry is unobservable due to the experimental conditions.[2, 3] For instance, the direct oxidation of guanine (G) in DNA (to initially form a singly oxidized species, Gox) is kinetically slow at the ITO electrode and thus unobservable under typical experimental conditions. However, G can be oxidized in solution by electrogenerated $Ru(bpy)_3^{3+}$ (2) because $Ru(bpy)_3^{3+}$ is a better oxidant than Gox, i.e., $E_{1/2}(Ru(bpy)_3^{3+/2+}) > E_{1/2}(Gox/G)$.

(1) $Ru(bpy)_3^{2+} \rightarrow Ru(bpy)_3^{3+} + e^-$

(2) $Ru(bpy)_3^{3+} + G \rightarrow Ru(bpy)_3^{2+} + Gox$

Rather than a direct loss of guanine electrons to the electrode, the $Ru(bpy)_3^{3+/2+}$ couple mediates the oxidation of guanine, essentially acting as an electron shuttle between guanine in solution and the electrode surface (Figure 4.2B). The $Ru(bpy)_3^{2+}$ initially present in solution is regenerated in reaction 2, completing a catalytic cycle, and can then be reoxidized by reaction 1. The cycle can turn over many times during the oxidative sweep, resulting in an increase in the observed oxidative current beyond what is observed for a simple E process in the absence of G (Figure 4.2A). The extent of catalysis in the presence of G compared to the CV for the $Ru(bpy)_3^{3+/2+}$ couple alone is, among other factors, dependent upon the rate of ET in reaction 2. The kinetics of this reaction are described by known equations for the EC′ reaction[1] and can be modeled by the digital simulation program DigiSim. This simulator is a powerful tool for constructing the CV expected from any combination of E and C reactions over a wide range of input parameters, making it possible to observe the effects of any factor influencing the EC′ mechanism and to extract mechanistic and kinetic information about ET processes experimentally observed in CV.[4]

A variety of transition metal complexes ($M^{3+/2+}$) similar to $Ru(bpy)_3^{3+/2+}$ can be employed in this EC′ scheme as metal mediators. By incorporating 4,4′-dimethyl-2,2′-bipyridine (dmb) ligands and varying the metal identity from ruthenium(III/II) to other low-spin, $d^5/d^6$ complexes of iron(III/II) or osmium(III/II), the mediator redox potential can be tuned.[3, 5, 6] The complexes used in the present study, $Os(dmb)_3^{2+}$, $Os(bpy)_3^{2+}$, $Fe(dmb)_3^{2+}$, $Fe(bpy)_3^{2+}$, $Ru(dmb)_3^{2+}$, $Ru(bpy)_2(dmb)^{2+}$, and $Ru(bpy)_3^{2+}$, each undergo nearly reversible heterogeneous ET at an ITO electrode, with redox potentials varying from 460 to 1080 mV (as measured in this work, Table 4.1).

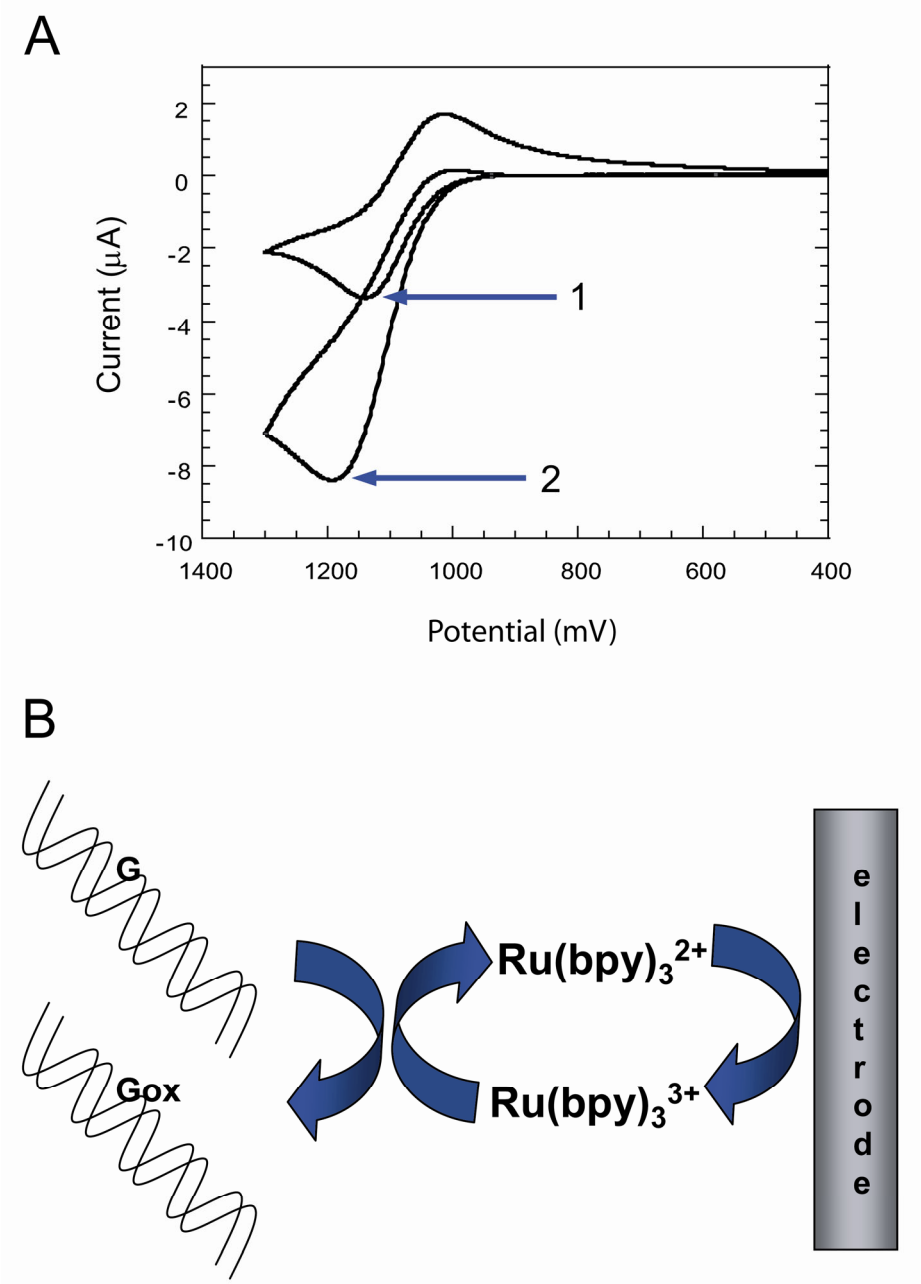


**Figure 4.2 Metal-mediated electrochemistry.** (A) Cyclic voltammograms and (B) scheme showing the metal-mediated oxidation of guanine-containing DNA. As the potential is swept from ~950 to 1300 mV, the ITO working electrode is sufficiently positively biased to oxidize $Ru(bpy)_3^{2+}$ at its surface to $Ru(bpy)_3^{3+}$. This oxidized metal complex can in turn oxidize DNA guanine (G) nucleobases in solution, producing oxidized guanine (Gox), re-generating $Ru(bpy)_3^{2+}$, and completing a catalytic cycle. This $Ru(bpy)_3^{2+}$ is oxidized again at the electrode, generating more oxidative current. The catalytic cycle can turn over many times during the oxidative CV sweep, depending on diffusion and ET rates and the CV scan rate, resulting in an enhanced oxidative current when DNA is present (2), relative to the oxidative peak current observed in the absence of DNA (1).

**Table 4.1 Extinction Coefficients, Redox Potentials, and Experimental Cyclic Voltammetry Potentials for Metal Mediators**

| | Metal(II) Extinction Coefficient ($M^{-1}cm^{-1}$) | Redox Potential (mV vs. Ag/AgCl) | Maximum CV Potential[a] (mV vs. Ag/AgCl) |
|---|---|---|---|
| $Os(dmb)_3^{3+/2+}$ | $\varepsilon_{496} = 13{,}000$ [7] | 460 | 750 |
| $Os(bpy)_3^{3+/2+}$ | $\varepsilon_{490} = 12{,}900$ [8] | 645 | 850 |
| $Fe(dmb)_3^{3+/2+}$ | $\varepsilon_{529} = 8{,}400$ [9] | 700 | 900 |
| $Fe(bpy)_3^{3+/2+}$ | $\varepsilon_{522} = 8{,}600$ [9] | 870 | 1050 |
| $Ru(dmb)_3^{3+/2+}$ | $\varepsilon_{458} = 17{,}000$ [10] | 905 | 1100 |
| $Ru(bpy)_2(dmb)^{3+/2+}$ | $\varepsilon_{454} = 16{,}000$ [10] | 1020 | 1200 |
| $Ru(bpy)_3^{3+/2+}$ | $\varepsilon_{452} = 14{,}600$ [10] | 1080 | 1250 |

[a] Initial and final CV potentials were 0 mV in all experiments.

**Electron Transfer in Carbon Nanotubes.** CNT electronic structure can be described by a rigid band model, and the one-dimensional nature of nanotubes creates a high density of electronic states called a van Hove singularity at the band edges (Figure 4.3). In the absence of external effects, the Fermi level (the energy at which it is equally probable for an electron or a hole to exist) of a CNT should be at a point halfway between the first valence ($v_1$) and conduction ($c_1$) van Hove singularities. The Fermi level can be shifted by an oxidizing/reducing agent or a positively/negatively biased electrode to an extent dependent upon the redox potential of the oxidant/reductant or the potential of the electrode.[11-16] If the Fermi level is shifted into the CNT valence or conduction band, the band is depleted (oxidized) or filled (reduced), respectively (Figure 4.3). Therefore, the energies of $v_1$ and $c_1$ define the redox potentials for the first valence and conduction band electrons, respectively.[14, 15, 17] These energies vary for CNTs of different chirality, giving rise to different redox potentials for different types of CNTs: CNTs with smaller energy gaps between $v_1$ and $c_1$ are easier to oxidize and reduce compared to CNTs with larger bandgap energy.[13, 16, 18, 19] Since CNT electronic bands encompass a range of energies, electrons within a single CNT type also have a range of redox potentials.

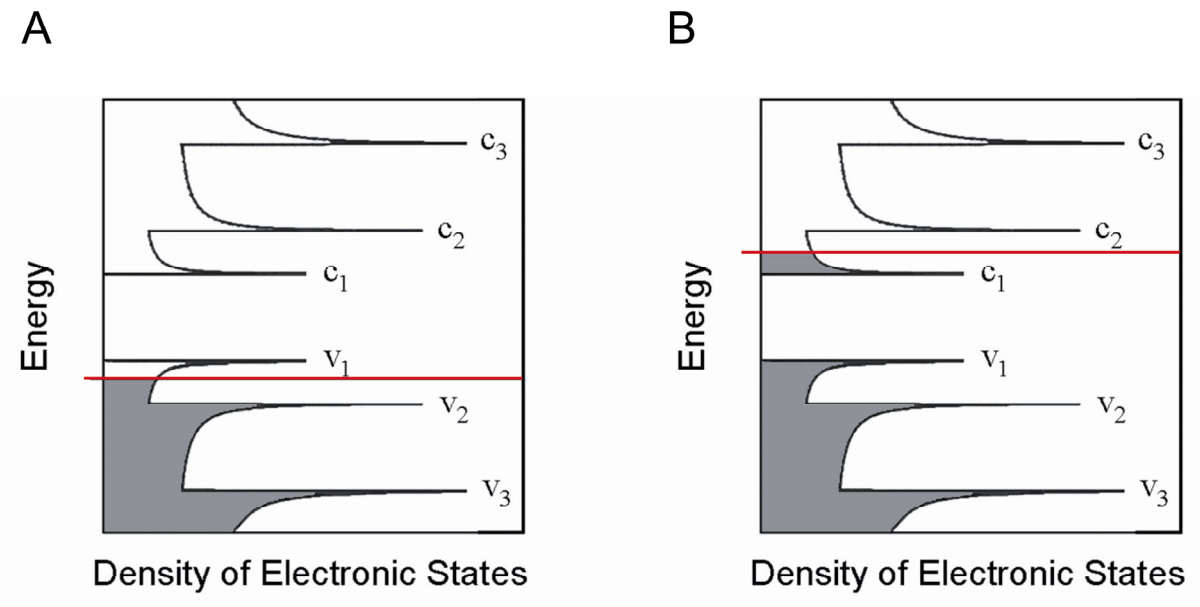


**Figure 4.3 Effect of oxidation and reduction on CNT electronic band structure.** Diagrams show the density of electronic states for one semiconducting CNT type, showing (A) oxidation (or p-doping) and (B) reduction (or n-doping). The red line represents the CNT Fermi level, which is shifted during oxidation/reduction to a degree dependent upon the redox potential of the oxidizing or reducing agent (for chemical redox) or the electrode potential (for electrochemical redox). Shading indicates states filled with electrons, and van Hove singularities are labeled in the valence ($v_n$) and conduction ($c_n$) bands.

ET has a profound effect on CNT electronic and optical properties. Both oxidation and reduction decrease CNT absorption and fluorescence, alter resonance Raman spectra, and increase the number of charge carriers (holes for oxidation; electrons for reduction), which results in increased CNT conductance.[11, 13, 16, 17, 20] CNTs in solid films can be reversibly charge-doped by solution and gaseous electron acceptors (p-doping) and donors (n-doping) adsorbed on the nanotube surface, increasing the film conductance.[21-23] Solubilized CNTs (including those wrapped with single-stranded DNA, CNT–DNA) can undergo reversible redox chemistry with oxidants and reductants, depleting and filling CNT electronic bands in a bandgap-selective manner (Chapter 2).[16, 18, 24] While the extent of ET caused by these chemical means depends on the redox potential of the oxidizing/reducing

agent, electrochemistry can be used to precisely tune the level of CNT oxidation or reduction.[12, 25, 26] Spectra of CNT films demonstrate reversible depletion of the CNT valence band and filling of the conduction band under an applied oxidative and reductive potential, respectively, with intercalation of supporting electrolyte to balance the charge generated in the CNTs.[11, 17, 20, 27] Most electrochemical studies of CNT ET have employed CNTs as the working electrode (a role for which they have considerable promise[25, 28-30]), while measurements of CNTs in solution are hindered by the poor solubility of some CNT suspensions, which are unstable in the supporting electrolyte required for electrochemistry. Here, we used stable solutions of CNT–DNA to investigate the ET of soluble CNTs in an aqueous environment.

CNT–DNA can be reversibly oxidized by solution redox agents with $E_{1/2}$ as low as 645 mV vs. Ag/AgCl. However, we found no evidence of a similar reversible depletion and filling of CNT electronic bands at an electrode. Therefore, we employed metal mediators in an electrochemical–chemical system (analogous to that described above for the oxidation of guanine).[31] This indirect electrochemical technique allowed us to use CV and the quantitative analysis afforded by digital simulation to describe the solution redox chemistry of CNT–DNA. We found that stronger metal oxidants remove more CNT electrons, with rate constants reflecting the varying redox potentials for different valence band electrons within one CNT type and within the distribution of CNT types present in CNT–DNA. This insight into CNT electron transfer may prove useful in efforts to controllably tune CNT optical–electronic properties and to develop CNT transistors, devices for charge storage, and chemical sensors.

## 4.3 Experimental Section

**General.** In-house distilled water was purified by a Milli-Q Plus system (Millipore; Bedford, MA). CNT–DNA solutions were prepared with $T_{60}$ deoxyribooligonucleotide and their concentrations determined from absorbance spectra collected with a Shimadzu UV-3600 UV–VIS–NIR spectrophotometer with baseline correction for the buffered solution (as described in Chapter 2). Transition metal complexes of Fe(II), Ru(II), and Os(II) were synthesized and isolated as chloride salts via methods adapted from the literature,[7, 32] and their concentrations in solution were determined using known molar extinction coefficients (Table 4.1) and a Cary 300-Bio UV–visible spectrophotometer with baseline correction for the buffered solution. All solutions were prepared in 100 mM sodium phosphate buffer, pH 7.0, unless otherwise noted.

**Electrodes.** Electrochemical measurements were made with a three-electrode cell assembly[33] consisting of a Ag/AgCl reference electrode filled with 3 M KCl (Cypress Systems, Inc.; Lawrence, KS), platinum wire auxiliary electrode (Sigma-Aldrich; St. Louis, MO), and tin-doped indium oxide (ITO) working electrode (Applied Films Corporation; Longmont, CO). ITO electrodes (15×15 mm) were cut from glass plates coated with ITO by the University of North Carolina at Chapel Hill Chemistry Department glass shop, washed with isopropanol (~400 mL per 20 plates) while lying in a Buchner funnel, and then sonicated in a water-bath sonicator (Fisher Scientific; Suwanee, GA) for 15-minute periods in water then isopropanol then water twice more, with water rinsing between each step. During all cleaning steps, a voltmeter was used to ensure that the ITO-coated side of the plates faced the cleaning solutions. Following cleaning, the electrodes were allowed to dry at room temperature and stored in a dish covered with plastic wrap. Conversion of literature-

reported potentials versus the normal hydrogen electrode (NHE) was performed by assuming a potential of 200 mV versus NHE for the Ag/AgCl reference electrode. Unless otherwise designated, all potentials are reported versus Ag/AgCl.

**Cyclic Voltammetry.** Voltammograms were collected using a CH Instruments 600 series potentiostat. For each CV, a new cleaned ITO electrode with 0.32 $cm^2$ exposed surface area was preconditioned by five consecutive CVs at 25 mV $s^{-1}$ in 100 μL of 100 mM sodium phosphate buffer, pH 7.0. A CV of metal ($M^{2+}$) with or without CNT–DNA (also in 100 mM sodium phosphate buffer, pH 7.0) was then collected at 25, 300, or 1000 mV $s^{-1}$ over a potential range that would encompass the metal mediator faradaic peaks (Table 4.1). Experiments were performed in triplicate or quadruplicate, and an average of these CVs was used for the figures of this work and in digital simulation. CVs of $M^{2+}$ in the absence of CNT–DNA were background-corrected by subtracting a CV of the buffer alone; CVs of $M^{2+}$ in the presence of CNT–DNA were corrected by subtracting a CV of CNT–DNA without $M^{2+}$. CVs were also collected of $M^{2+}$ in the presence of *DNA* as a control experiment. The concentration of DNA in these CVs was the same as that estimated to be present in CVs of metals with CNT–DNA (using calculation method 1 described in the Experimental Section of Chapter 2), and CVs were background-corrected by subtraction of a DNA-only CV.

**Digital Simulation.** Voltammograms were digitally simulated using the DigiSim program (v.3.03b; Bioanalytical Systems; West Lafayette, IN). In all simulations, the temperature was 298.2 K and the working electrode was a planar electrode with 0.32 $cm^2$ surface area. The program used semi-infinite diffusion, Butler-Volmer heterogeneous kinetics with $\alpha\lambda^{-1}$ = 0.5 eV, pre-equilibration, and default values for the model parameters.

Other important simulation parameters and mechanisms (where forward arrows represent reversible reactions) are described in the Discussion.

**Size-Exclusion Chromatography.** For some CV experiments, CNT–DNA was first purified on a CNT-1000 size-exclusion column purchased from Sepax Technologies, Inc. (Newark, DE). This column had an inner diameter of 4.6 mm, length of 250 mm, and packing material of specially coated 5-μm silica particles with 1000-angstrom pore size. CNT–DNA (150 μL) was loaded onto the column with an autosampler and eluted at 250 μL minute$^{-1}$ with 100 mM sodium phosphate buffer, pH 7.0, using a Shimadzu HPLC system with absorbance detection at 280 nm. Eluted fractions were collected every 30 s and their absorbance spectra then measured in the range of 200–1300 nm (Figure 4.4). Spectra of early fractions are consistent with an increased CNT length compared to later fractions.[34] Similar results were obtained in three trials.

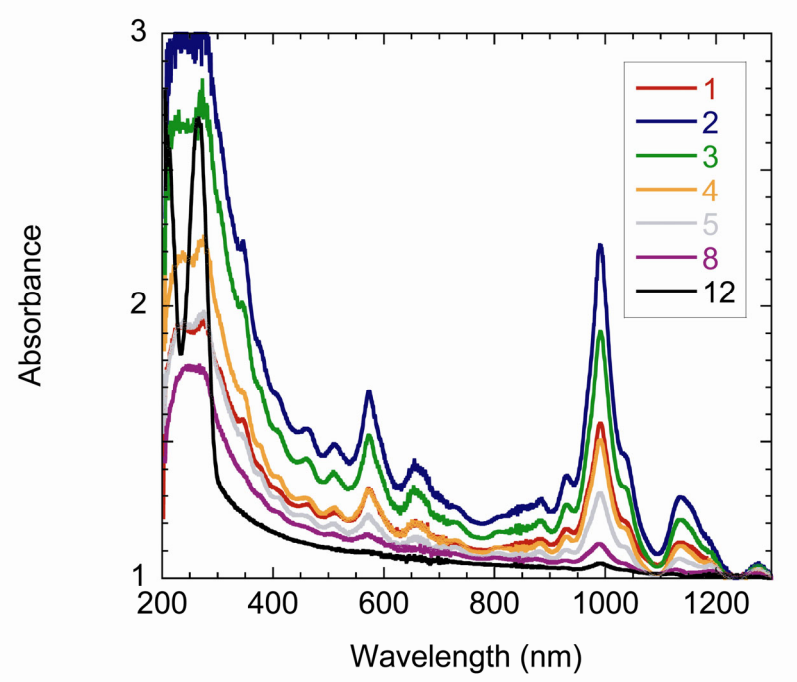


**Figure 4.4 Absorbance spectra of CNT–DNA fractions after size-exclusion chromatography.** Spectra of CNT–DNA in 100 mM sodium phosphate buffer, pH 7.0, are normalized at 1300 nm (in lieu of the 1600–1800 nm region), permitting a comparison of approximate CNT length with relative elution time (given by the fraction number in the legend), which is sufficient to demonstrate increased absorption and therefore longer CNTs in fractions 2–3, compared to later fractions.[34] Fraction 2 was used for the $Ru(bpy)_3^{3+/2+}$-mediated CV shown in Figure 4.9.

**Reaction of DNA-Wrapped Carbon Nanotubes with Tris(bipyridine)osmium(III).** In a non-electrochemical experiment, CNT–DNA was reacted with $Os(bpy)_3^{3+}$. To synthesize this Os(III) oxidant, $[Os(bpy)_3](PF_6)_2$ was stirred in dichloromethane under Ar and bubbled with $Cl_2$ for 30 minutes. The reaction mixture was purged of $Cl_2$ and vacuum filtered and the solid product washed with dichloromethane then diethyl ether to isolate $[Os(bpy)_3](PF_6)_2Cl$. This solid was dissolved minimally in acetonitrile, and an acetonitrile solution of bis(triphenylphosphoranylidene)-ammonium chloride was added dropwise to precipitate the complex as $[Os(bpy)_3]Cl_3$, which was isolated by vacuum filtration, washed with acetonitrile, and washed with diethyl ether. Solution

concentrations of $[Os(bpy)_3]Cl_3$ were determined by absorbance measurement with $\varepsilon_{316}$ = 41,200 $M^{-1}$ $cm^{-1}$.[35]

To observe the reaction of CNT–DNA with $[Os(bpy)_3]Cl_3$, an absorbance spectrum of 20 μM Os(III) oxidant was collected before and after the addition of CNT–DNA (6.0 μg $mL^{-1}$ ≈ 35 nM CNT, final concentration upon dilution with the oxidant solution) in 100 mM sodium phosphate buffer, pH 7.0. Spectra containing $Os(bpy)_3^{3+}$ were collected immediately after dissolving the solid $[Os(bpy)_3]Cl_3$ in buffer, as $Os(bpy)_3^{3+}$ is quickly reduced in neutral solution.

## 4.4 Results

**Metal-Mediated Electrochemical Oxidation of DNA-Wrapped Carbon Nanotubes.** We observed an increase in oxidative CV current for $Ru(bpy)_3^{3+/2+}$ in the presence of CNT–$T_{60}$ compared to its absence (Figure 4.5).[31] Similar results were obtained for solutions purged of oxygen and for CVs collected with a higher (800 mV) initial potential. No such current enhancement was observed for $Ru(bpy)_3^{3+/2+}$ in the absence of CNT–DNA but presence of *DNA*. In the absence of $Ru(bpy)_3^{3+/2+}$, CNT–DNA exhibited no current except for an irreversible oxidation at ~1100 mV.

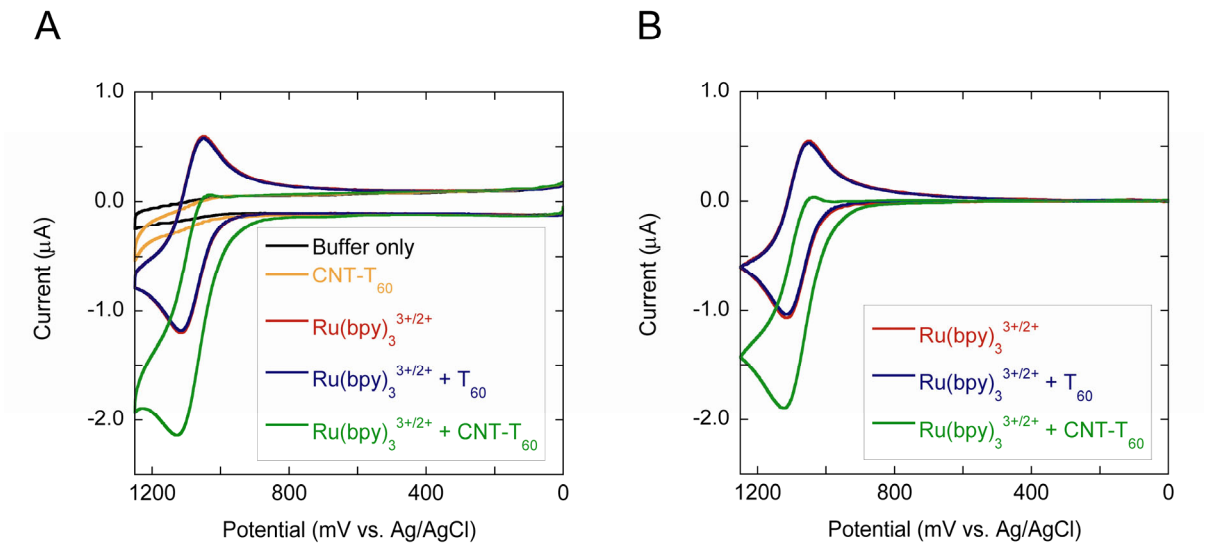


**Figure 4.5 Metal-mediated oxidation of CNT–DNA.** (A) Cyclic voltammograms with no background correction are shown for solutions in sodium phosphate buffer (100 mM, pH 7.0) collected at 25 mV $s^{-1}$. The CV of $Ru(bpy)_3^{3+/2+}$ in the presence of CNT–$T_{60}$ contains 25 μM metal mediator and 10 μg $mL^{-1}$ ≈ 59 nM CNT with ~1.1 μM $T_{60}$. Control experiments show CNT–$T_{60}$ (10 μg $mL^{-1}$ ≈ 59 nM CNT with ~1.1 μM $T_{60}$) alone, $Ru(bpy)_3^{3+/2+}$ (25 μM) alone, and $Ru(bpy)_3^{3+/2+}$ (25 μM) with $T_{60}$ (1.1 μM). (B) Cyclic voltammograms resulting from background correction of those shown in A, demonstrating the increased oxidative peak current of $Ru(bpy)_3^{3+/2+}$ in the presence of CNT–DNA, but not in the presence of DNA alone.

***Effect of Nanotube and Metal Concentrations.*** The oxidative current enhancement observed for 25 μM $Ru(bpy)_3^{3+/2+}$ in the presence of CNT–DNA increased with increasing CNT–DNA concentration (Figure 4.6A). When the CNT–DNA concentration was held constant, the extent of oxidative current enhancement decreased with increasing concentration of $Ru(bpy)_3^{3+/2+}$ (Figure 4.6B–D).

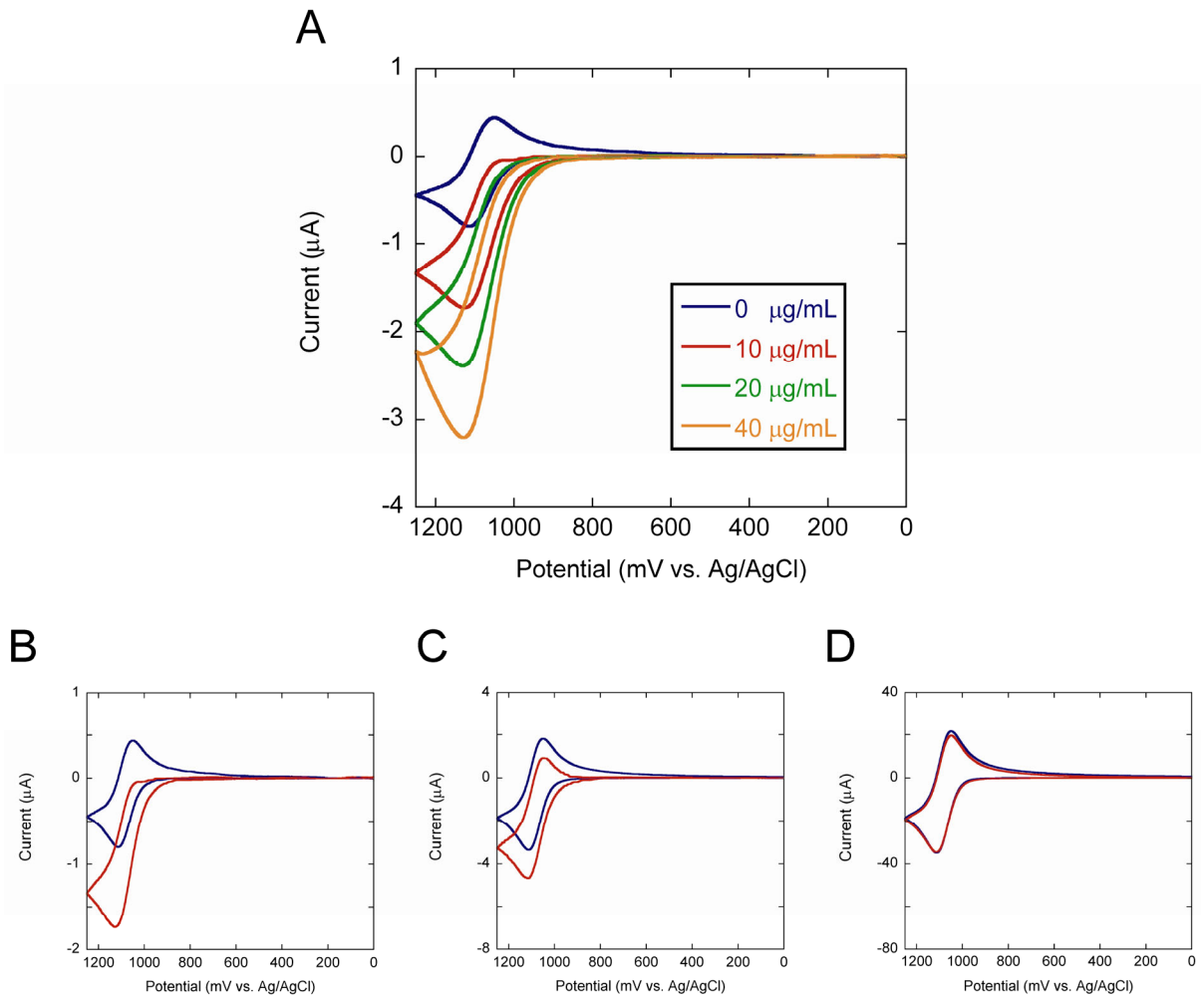


**Figure 4.6 Concentration dependence of metal-mediated CNT–DNA oxidation.** (A) Cyclic voltammograms of $Ru(bpy)_3^{3+/2+}$ (25 μM) alone and with increasing concentrations of CNT–$T_{60}$ (10 μg $mL^{-1}$ ≈ 59 nM, 20 μg $mL^{-1}$ ≈ 118 nM, and 40 μg $mL^{-1}$ ≈ 235 nM CNT). For a constant CNT–DNA concentration (10 μg $mL^{-1}$ ≈ 59 nM), CVs are shown for (B) 25, (C) 100, and (D) 1000 μM $Ru(bpy)_3^{3+/2+}$ in the absence (blue) and presence (red) of CNT–$T_{60}$. Data were collected in 100 mM sodium phosphate buffer, pH 7.0, at 25 mV $s^{-1}$.

***Effect of Metal Redox Potential.*** Increased metal oxidative peak current in the presence of CNT–DNA was also observed for several metal complexes similar in structure to $Ru(bpy)_3^{3+/2+}$ yet having different redox potentials. While CV of a metal complex with 460-mV redox potential, $Os(dmb)_3^{3+/2+}$, showed no difference in the presence of CNT–DNA compared to its absence, CV of six metals with higher redox potentials exhibited increased

oxidative peak current in the presence of CNT–DNA. The extent of this current enhancement relative to the current of the metal-only CV increased with increasing metal redox potential (Figure 4.7).

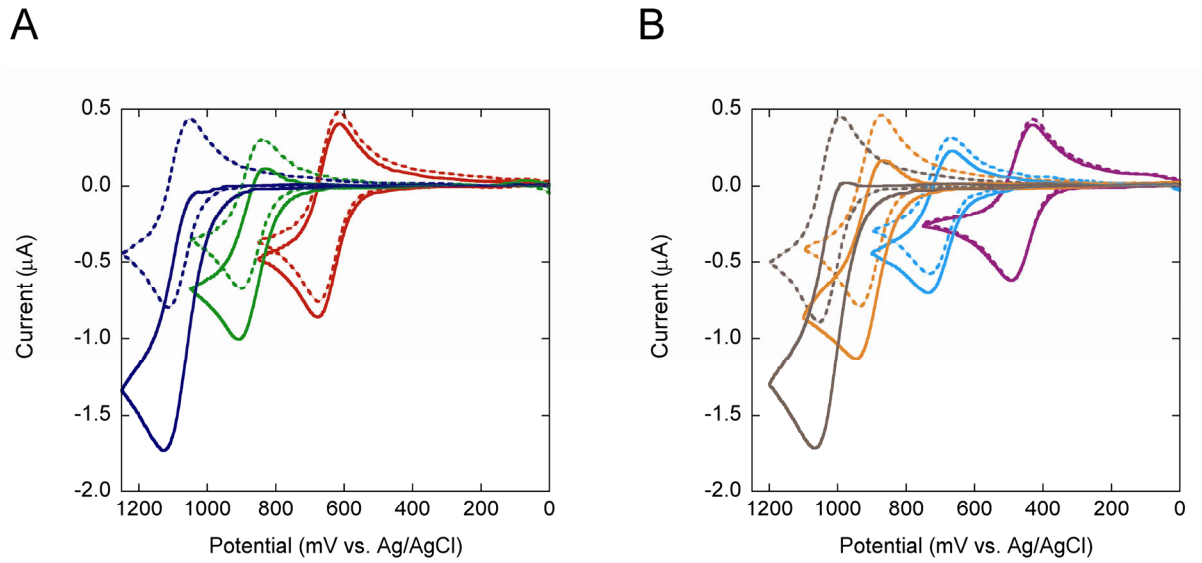


**Figure 4.7 Dependence of metal-mediated CNT–DNA oxidation on metal redox potential.** Cyclic voltammograms of metal mediators (25 μM) alone (dotted) and with CNT–$T_{60}$ (solid; 10 μg $mL^{-1}$ ≈ 59 nM CNT) in 100 mM sodium phosphate buffer, pH 7.0, collected at 25 mV $s^{-1}$. (A) Metal redox potential increases in the order: $Os(bpy)_3^{3+/2+}$ (red) < $Fe(bpy)_3^{3+/2+}$ (green) < $Ru(bpy)_3^{3+/2+}$ (blue). (B) Metal redox potential of dmb-containing complexes (shown separately for clarity) increases in the order: $Os(dmb)_3^{3+/2+}$ (purple) < $Fe(dmb)_3^{3+/2+}$ (light blue) < $Ru(dmb)_3^{3+/2+}$ (orange) < $Ru(bpy)_2(dmb)^{3+/2+}$ (brown).

***Effect of Scan Rate.*** CVs were collected for each metal mediator with and without CNT–DNA at three different scan rates. Regardless of scan rate, experimentally observed values of metal oxidative and reductive peak potentials, their difference (the peak separation), and their average ($E_{1/2}$) were all constant. The effect of metal redox potential shown in Figure 4.7 was observed at all scan rates, with a greater difference between the current observed with and without CNT–DNA evident at slower scan rate.

The effect of scan rate on metal CV current in the presence and absence of CNT–DNA is shown in Figure 4.8 as the current/(scan rate)$^{1/2}$ versus the applied potential; this y-axis was chosen because the current of a reversible, diffusion-controlled, heterogeneous ET process is directly related to the square root of scan rate.[1] The observation of nearly identical metal-only voltammograms at different scan rates in Figure 4.8A indicates a reversible, diffusion-controlled ET between the metal mediator and the electrode. Metal CV current in the presence of CNT–DNA, however, is not proportional to the square root of scan rate (Figure 4.8B). This result is an effect of the chemistry (that occurs following the heterogeneous ET) responsible for the current enhancement observed relative to CV of metals without CNT–DNA (Figure 4.7).

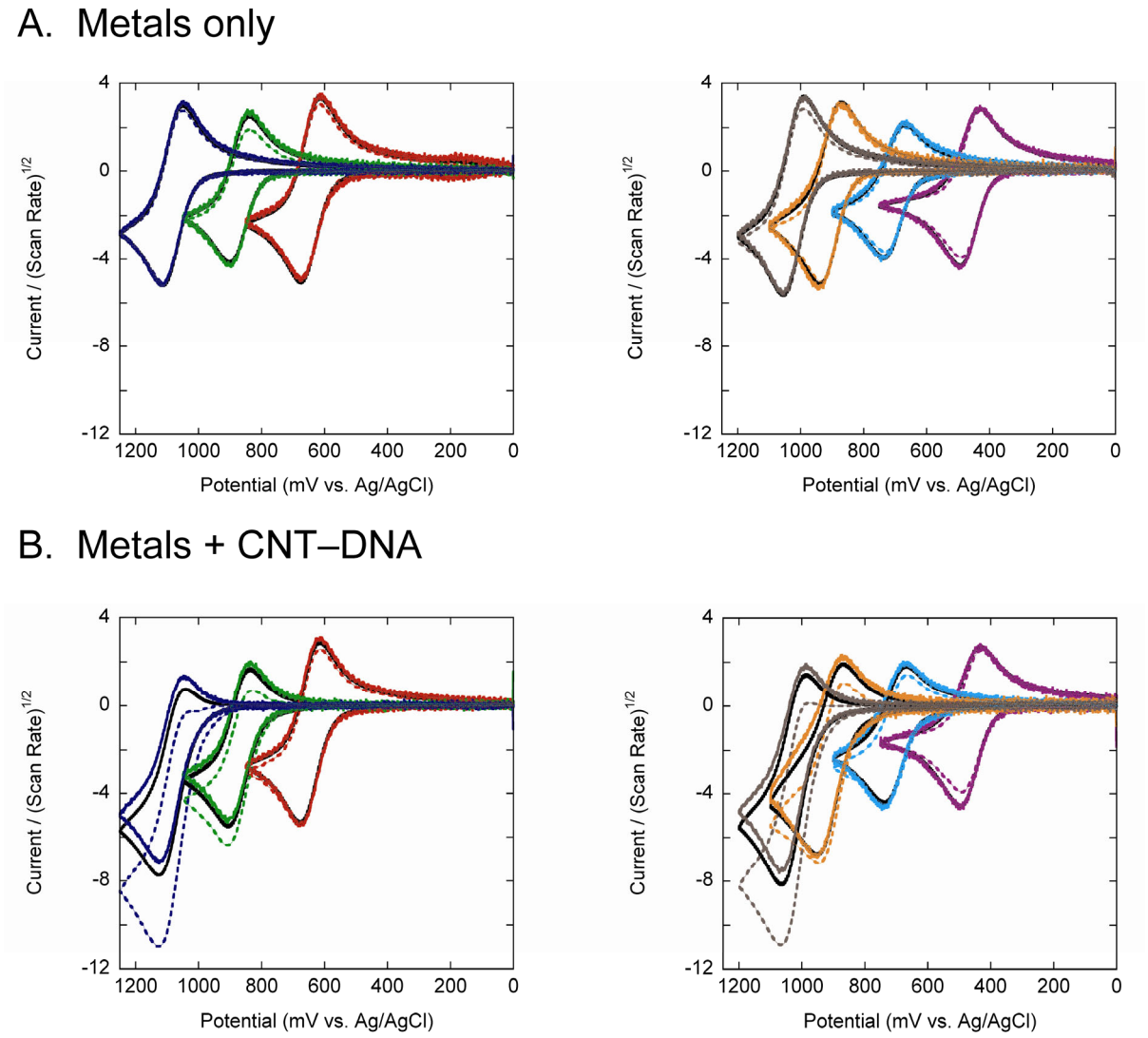


**Figure 4.8 Scan rate dependence of metal-mediated CNT–DNA oxidation.** Cyclic voltammograms of metal mediators (25 μM) (A) alone and (B) in the presence of CNT–$T_{60}$ (10 μg $mL^{-1}$ ≈ 59 nM CNT) in 100 mM sodium phosphate buffer, pH 7.0, collected at 25 (dotted), 300 (black), and 1000 (solid) mV $s^{-1}$. For clarity, the seven metal mediators are separated into two plots; $Ru(bpy)_3^{3+/2+}$ (blue), $Fe(bpy)_3^{3+/2+}$ (green), $Os(bpy)_3^{3+/2+}$ (red), $Ru(bpy)_2(dmb)^{3+/2+}$ (brown), $Ru(dmb)_3^{3+/2+}$ (orange), $Fe(dmb)_3^{3+/2+}$ (light blue), and $Os(dmb)_3^{3+/2+}$ (purple).

**Origin of the Increased Metal Mediator Oxidative Peak Current.** The two potential contaminates of our CNT–DNA solutions are carbonaceous impurities (such as amorphous carbon, nanotube or graphite fragments, and carbon nanoparticles) and metal catalyst particles. To address the impact of either of these contaminates in our metal-mediated electrochemistry, we examined the metal-mediated CV of CNT–DNA solutions after purification by size-exclusion chromatography (SEC) and also employed absorbance spectroscopy to determine whether or not CNTs are oxidized by $Os(bpy)_3^{3+}$.

***Electrochemistry of DNA-Wrapped Carbon Nanotubes after Size-Exclusion Chromatography.*** Since CNTs bind strongly to conventional packing materials, a packing material for SEC columns has been developed specifically for use with CNTs.[36] These columns sort CNTs according to length and effectively separate CNTs from small carbonaceous impurities.[34, 36] We used SEC columns to remove carbonaceous impurities from CNT–DNA solutions prior to metal-mediated CV experiments. CV of $Ru(bpy)_3^{2+}$ with this SEC-purified CNT–DNA demonstrated the increase in oxidative current (relative to CV in the absence of CNT–DNA) that was observed with our non-purified CNT–DNA (Figure 4.9). The change in average CNT length following SEC purification alters the intensity of CNT absorbance, preventing precise determination of the solution concentration of SEC-purified CNT–DNA;[34] however, we observed that similar concentrations of CNT–DNA with and without SEC purification (Figure 4.9B) caused similar increases in CV oxidative current (Figure 4.9A).

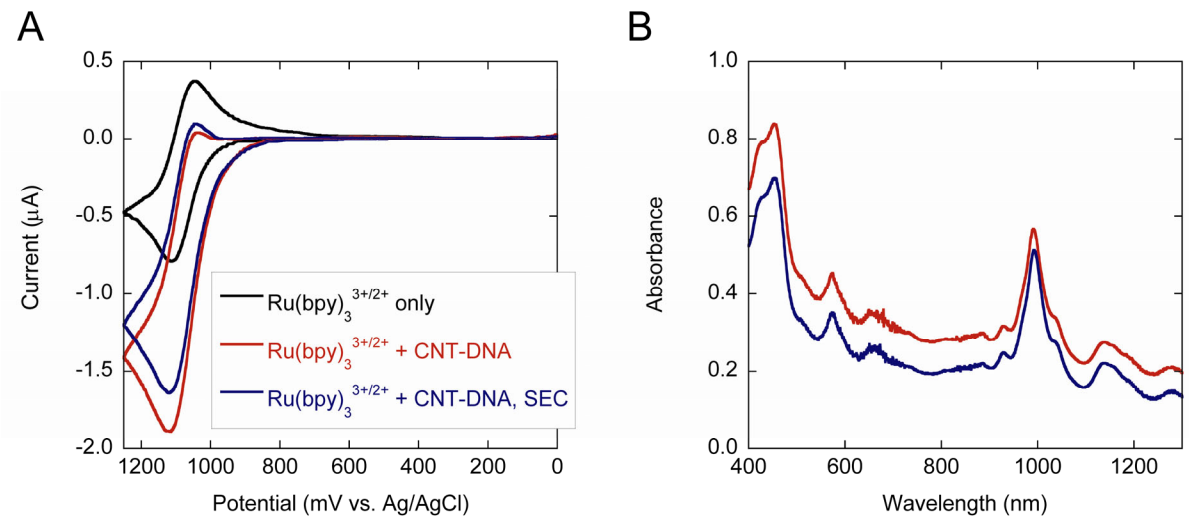


**Figure 4.9 Metal-mediated oxidation of CNT–DNA purified by size-exclusion chromatography.** (A) Cyclic voltammograms of $Ru(bpy)_3^{3+/2+}$ (23 μM) in 100 mM sodium phosphate buffer, pH 7.0, with CNT–$T_{60}$ before and after purification by SEC, showing no significant change in $Ru(bpy)_3^{3+/2+}$-mediated oxidation after the removal of carbonaceous impurities. (B) Absorbance spectra of the experimental solutions whose CVs are shown in A, showing similar concentrations of $Ru(bpy)_3^{2+}$ (contributing to the absorbance in the 400–500 nm range) and CNT–DNA. The CV before SEC appears to have been collected for a solution with a slightly higher concentration of CNT–DNA compared to the CV after SEC, which is reflected in the slightly increased oxidative peak current in A (changes in absorbance due to changes in the distribution of CNT lengths isolated in the SEC fraction prevented exact concentration determination).

***Reaction of DNA-Wrapped Carbon Nanotubes with Tris(bipyridine)osmium(III).*** To determine whether the CNTs in our CNT–DNA solutions are oxidized by the $M^{3+}$ oxidants generated in metal-mediated electrochemistry, we added a solid salt of $Os(bpy)_3^{3+}$ to CNT–DNA solutions and monitored the absorbance spectrum. CNT and $Os(bpy)_3^{3+}$ absorption peaks were observed to immediately decrease and $Os(bpy)_3^{2+}$ peaks to concomitantly increase (Figure 4.10) (the bleached CNT absorptions then reappeared over time, consistent with our observations for the chemical oxidation of CNT–DNA by $IrCl_6^{2-}$ described in Chapter 2).

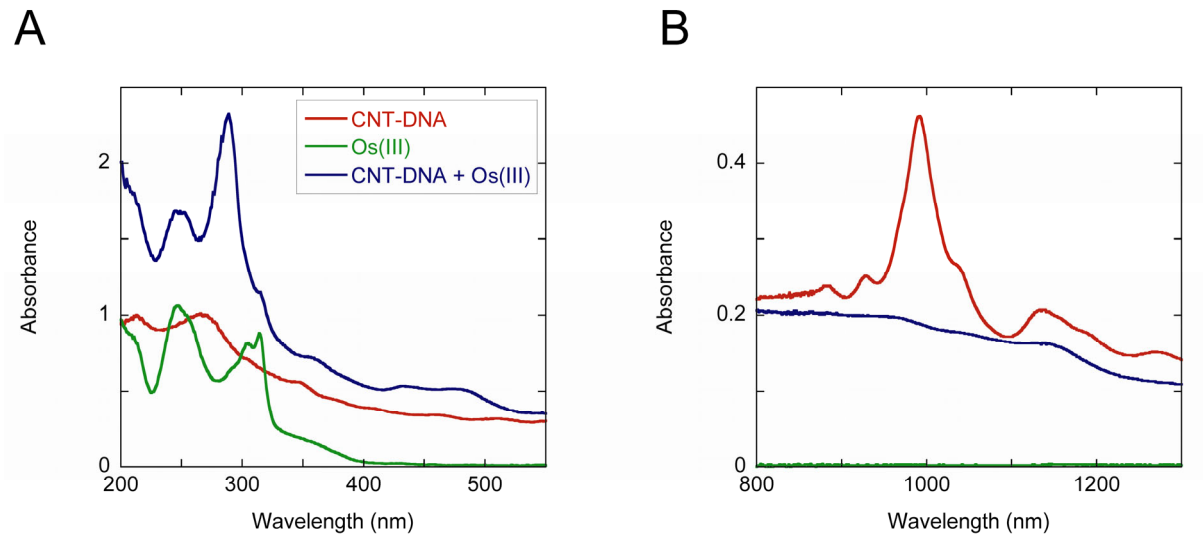


**Figure 4.10 Chemical oxidation of CNT–DNA by tris(bipyridine)osmium(III).** Absorbance spectra of Os(III) oxidant (initially 20 μM, green) before and ~30 s after the addition of CNT–$T_{60}$ (6.0 μg $mL^{-1}$ ≈ 35 nM CNT, final concentration, blue), compared to an equal concentration of CNT–DNA in the absence of oxidant (red). All solutions are in 100 mM sodium phosphate buffer at pH 7.0. After combining CNT–DNA with Os(III), (A) the Os(III) absorption at 316 nm is decreased, Os(II) absorptions at 287 and 420–520 nm appear, and (B) CNT–DNA absorbance is decreased.

## 4.5 Discussion

**Origin of the Increased Metal Mediator Oxidative Peak Current.** CNT–DNA material prepared from CoMoCAT CNTs by tip-sonication and centrifugation with oligonucleotides (as our samples are prepared) shows no evidence of Co or Mo catalyst and has few carbonaceous impurities.[34] We investigated the possible influence of any remaining impurities on CNT–DNA electrochemistry. When CNT–DNA solutions were purified of carbonaceous particles by SEC, they exhibited similar oxidative current enhancement in metal-mediated CV as CNT–DNA solutions without SEC purification, suggesting that carbonaceous impurities do not play a significant role in our electrochemical experiments.

Residual metal catalyst particles might not be removed by SEC and have been reported to enhance the properties of electrodes modified with CNT bundles. For example,

the decreased overpotentials needed to oxidize hydrazine or reduce hydrogen peroxide result from metal catalyst particles contaminating the CNTs.[37-39] This involvement of metal particles is likely limited to particular applications of CNT-modified electrodes, as there is strong evidence for ET involving the CNTs themselves. In particular, work on single nanotubes containing no contaminants has demonstrated rapid ET with outer-sphere redox agents.[25] Absorbance spectra of CNT–DNA after the addition of $Os(bpy)_3^{3+}$ suggest that the oxidative current enhancement of metal mediator CVs in the presence of CNT–DNA is further evidence of ET involving the CNTs rather than metal particles. CNT $E_{11}$ absorption peaks (800–1300 nm) directly reflect the electronic population of the first valence band of various CNT chiral types; therefore, the spectral bleach of these absorptions caused by the addition of $M^{3+}$ is a direct observation of the oxidation of CNTs by $M^{3+}$ in solution. This evidence for the $M^{3+} + CNT \rightarrow M^{2+} + CNT^{+}$ reaction clearly demonstrates that CNTs, rather than any carbonaceous impurities or residual metal catalyst particles, are the reactive species in our metal-mediated electrochemical experiments.

The observation of CNT–DNA chemical oxidation by $M^{3+}$, in addition to our electrochemical findings of increased metal oxidative CV current in the presence of CNT–DNA and the lack of direct CNT–DNA oxidative current in the same potential range, all suggest a catalytic (EC′) mechanism in which CNT–DNA is oxidized in solution by electrogenerated $M^{3+}$. This homogeneous ET between the mediator and CNT–DNA completes a catalytic cycle responsible for the increased oxidative peak current observed for metals in the presence of CNT–DNA (Figure 4.11).

The lack of metal current enhancement in the presence of $T_{60}$ without CNT (Figure 4.5) (along with the spectral evidence of reaction between $M^{3+}$ and CNT discussed above)

suggests that the CNT, rather than the wrapping DNA, is the oxidized species. The $T_{60}$ sequence was in fact chosen because its oxidation potential is higher than that of $Ru(bpy)_3^{3+/2+}$ (and the other metal mediator couples employed in this work),[40] preventing DNA oxidation and allowing us to study the oxidation of the CNTs. CV of CNTs wrapped with a DNA sequence containing the more easily oxidized guanine nucleobase, on the other hand, resulted in increased oxidative current compared to CNT–$T_{60}$ (data not shown), suggesting both the guanine and the CNT participate in the catalytic cycle.

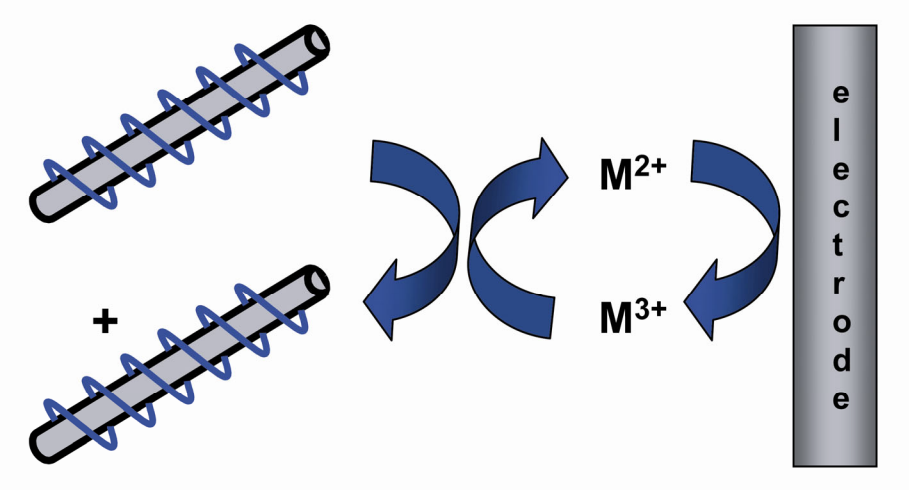


**Figure 4.11 Catalytic cycle responsible for metal-mediated oxidation of CNT–DNA.** During CV of $M^{2+}$ (e.g., $Ru(bpy)_3^{2+}$) with CNT–$T_{60}$, an EC′ mechanism occurs in which $M^{3+}$ formed at a sufficiently positively biased electrode can react with CNT–DNA in solution to oxidize CNT–DNA and reduce $M^{3+}$. The resulting $M^{2+}$ can again be oxidized at the electrode, resulting in increased peak current for the $M^{2+} \rightarrow M^{3+} + e^-$ oxidative wave.

Our observations of increased metal current enhancement with higher CNT–DNA concentration and at slower scan rate (where there is more CNT–DNA reductant and more time for the catalytic cycle to turn over, respectively) are consistent with the EC′ mechanism. We also observed enhanced metal oxidative peak current, and thus increased catalysis, with higher metal redox potential. While the metal mediator with the lowest redox potential,

$Os(dmb)_3^{3+/2+}$, exhibited no current enhancement in the presence of CNT–DNA and thus did not oxidize CNT–DNA, the other six metals catalytically oxidized CNT–DNA to an extent dependent upon the oxidizing strength of their $M^{3+}$ form. To describe this homogenous ET quantitatively and further investigate the solution redox chemistry of CNT–DNA, CVs of CNT–DNA with the six metal mediators were analyzed via digital simulation.

**Digital Simulation of Metal Voltammograms in the Absence of DNA-Wrapped Carbon Nanotubes.** Simulation of metal mediator CVs in the absence of CNT–DNA provided information necessary for simulating metal CVs in the presence of CNT–DNA. The CV of a metal complex oxidized and reduced at an electrode surface via a simple E mechanism (3) at a given CV scan rate can be predicted from the metal heterogeneous ET rate constant, redox potential, diffusion coefficient, and bulk concentration. Using these parameters, a CV was constructed in the DigiSim digital simulation program with the intent of reproducing the experimentally obtained CV for each metal complex. In general, the value of any unknown parameter in a simulation was determined by altering it until the shape of the simulated CV fit the shape of the experimental CV (details are discussed below).

(3) $M^{2+} \rightarrow M^{3+} + e^-$

***Heterogeneous Rate Constants.*** Simulation with a fast rate constant for ET between the metal and the electrode ($1 \times 10^4$ cm $s^{-1}$) described all the metal mediators in this study, indicating their nearly reversible ET at ITO.

***Metal Mediator Redox Potentials.*** The simulated redox potential was simply chosen so that the simulated CV aligned with the experimental CV relative to the applied potential

(x-axis of the voltammogram). This redox potential is an $E_{1/2}$ value (i.e., it can be calculated as the average of the oxidative and reductive peak potentials), which is expected to closely approximate $E^{0'}$ for our experimental conditions because the $M^{3+}$ and $M^{2+}$ species are expected to diffuse at similar rates.

***Metal Mediator Concentration and Diffusion.*** The peak current ($i_p$) of a reversible metal CV under diffusion control depends (4) on both its diffusion coefficient (D) and its concentration in the bulk solution ($C^*$) (as well as the stoichiometric number of electrons transferred, n; electrode area, A; and scan rate, ν).[1] The metal concentration (25 μM, unless otherwise specified) was input into the simulations and the metal diffusion coefficient was altered to match the experimental peak current.

(4) $$i_P = (2.69 \times 10^5)\, n^{3/2}\, A\, D^{1/2}\, C^*\, \nu^{1/2}$$

***Simulation Mechanism.*** Each metal mediator was simulated with a simple E mechanism (3) in the manner described above. This approach was tested by applying the same values of each parameter to simulate data at three different CV scan rates, which produced simulated CVs that closely matched the experimental CVs (Figure 4.12). This result supports the validity of the E mechanism for simulation of metal CVs and suggests that the parameters used to construct the simulations (Table 4.2) closely describe the electrochemical behavior of the metal mediators. Therefore, the parameters obtained by simulating metals in the absence of CNT–DNA were next incorporated into simulations for metals in the presence of CNT–DNA.

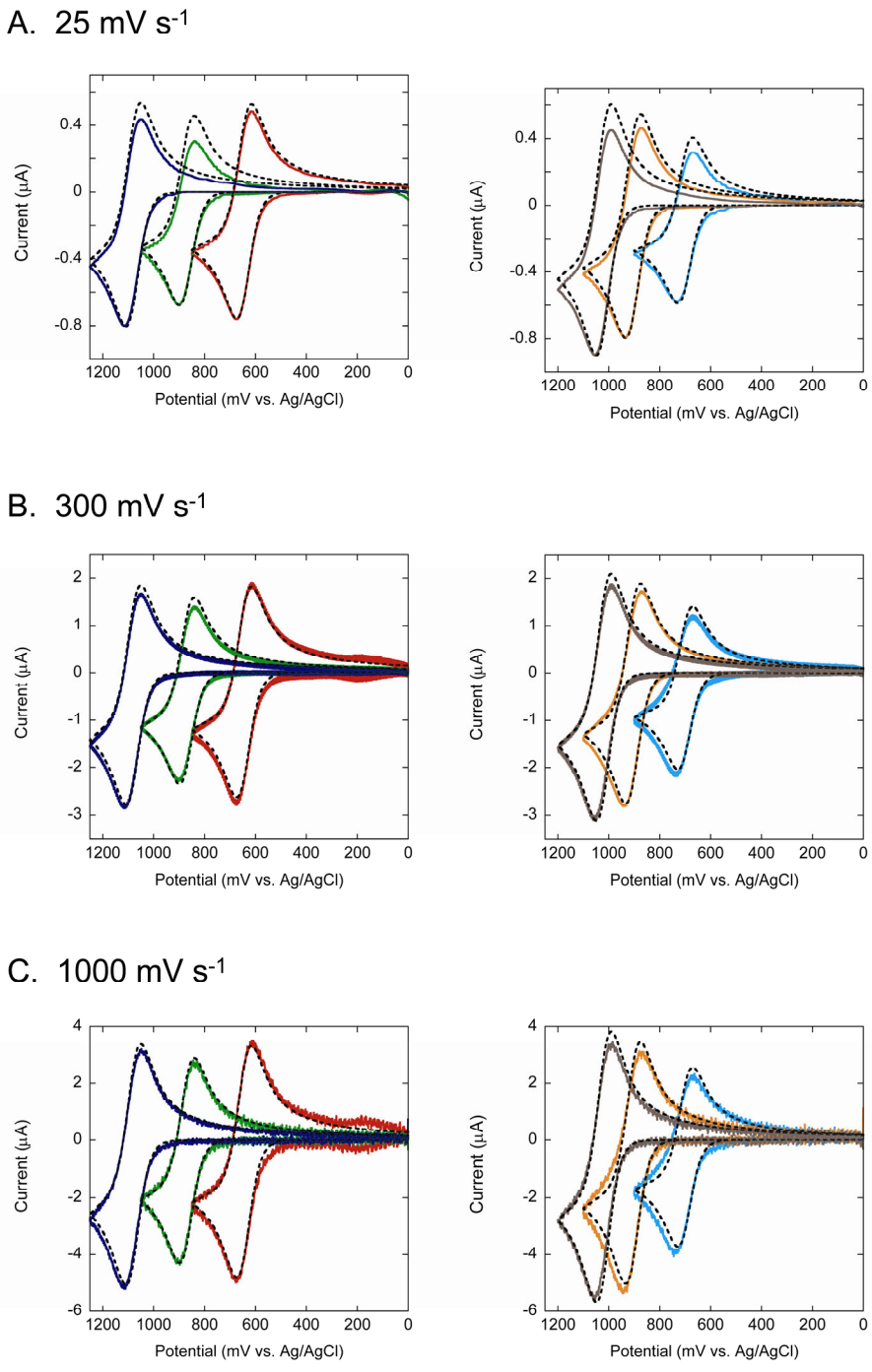


**Figure 4.12 Digital simulation of metal mediator CVs in the absence of CNT–DNA.** Experimental CVs of metals (25 μM) in 100 mM sodium phosphate buffer, pH 7.0, collected at (A) 25, (B) 300, and (C) 1000 mV $s^{-1}$ are shown in color. Dotted black lines show simulations employing an E mechanism with the same parameters at all scan rates (Table 4.2). For clarity, the six metal mediators are separated into two plots; $Ru(bpy)_3^{3+/2+}$ (blue), $Fe(bpy)_3^{3+/2+}$ (green), $Os(bpy)_3^{3+/2+}$ (red), $Ru(bpy)_2(dmb)^{3+/2+}$ (brown), $Ru(dmb)_3^{3+/2+}$ (orange), and $Fe(dmb)_3^{3+/2+}$ (light blue). $Os(dmb)_3^{3+/2+}$ is not shown because it did not oxidize CNT–DNA and thus required no simulation.

**Table 4.2 Digital Simulation Parameters Describing Cyclic Voltammetry of Metal Mediators in the Absence of CNT–DNA[a]**

| | Redox Potential (mV vs. Ag/AgCl) | Heterogeneous ET rate constant ($cm\ s^{-1}$) | Diffusion Coefficient ($cm^2\ s^{-1}$) | Bulk Concentration (μM) |
|---|---|---|---|---|
| $Os(bpy)_3^{3+/2+}$ | 645 | $1 \times 10^4$ | $5.0 \times 10^{-6}$ | 25 |
| $Fe(dmb)_3^{3+/2+}$ | 700 | $1 \times 10^4$ | $3.0 \times 10^{-6}$ | 25 |
| $Fe(bpy)_3^{3+/2+}$ | 870 | $1 \times 10^4$ | $4.0 \times 10^{-6}$ | 25 |
| $Ru(dmb)_3^{3+/2+}$ | 905 | $1 \times 10^4$ | $5.5 \times 10^{-6}$ | 25 |
| $Ru(bpy)_2(dmb)^{3+/2+}$ | 1020 | $1 \times 10^4$ | $7.0 \times 10^{-6}$ | 25 |
| $Ru(bpy)_3^{3+/2+}$ | 1080 | $1 \times 10^4$ | $5.6 \times 10^{-6}$ | 25 |

[a] Employing an E mechanism.

**Digital Simulation of Metal-Mediated Electrochemical Oxidation of DNA-Wrapped Carbon Nanotubes.** Digital simulation was employed to describe the experimental CVs of metal mediators with CNT–DNA using a classical catalytic mechanism (depicted in Figure 4.11). This EC′ mechanism involves the $M^{3+/2+}$ and $CNT^{+/0}$ redox couples, which each have a heterogeneous ET rate constant ($k_1$ and $k_2$, respectively) for oxidation at the ITO electrode (via 5 and 6, respectively), as well as a homogeneous ET rate constant ($k_1'$) for reaction with each other in solution (7). For this solution reaction to be favorable in the forward direction and produce the observed catalytic effect, the redox

potential of CNT–DNA must be lower than that of the $M^{3+/2+}$ couple (8).[1] Our CV data for CNT–DNA with different metal mediators suggest this to be the case for all mediators except $Os(dmb)_3^{3+/2+}$ (which exhibited no catalysis). Catalysis was observed with $Os(bpy)_3^{3+/2+}$ and metals of higher redox potential, placing the lowest observed $CNT^{+/0}$ redox potential in the 460–645 mV range, which is consistent with previous reports of $E_{1/2}$ for CNT first-valence band electrons.[18, 41]

(5) $M^{2+} \rightarrow M^{3+} + e^-, \quad k_1$

(6) $CNT_1 \rightarrow CNT_1^+ + e^-, \quad k_2$

(7) $M^{3+} + CNT_1 \rightarrow M^{2+} + CNT_1^+, \quad k_1'$

(8) $\Delta G = -nF\left\{ E_{1/2}\left(M^{3+/2+}\right) - E_{1/2}\left(CNT^{+/0}\right) \right\}$

Since $E_{1/2}(CNT^{+/0}) < E_{1/2}(M^{3+/2+})$, we would not observe metal-mediated catalysis for the six metals if CNT–DNA was oxidized at the electrode where thermodynamics predicts. CNT–DNA must instead remain unoxidized at the higher applied potential needed to electrogenerate the $M^{3+}$ (5) for its participation in reaction 7. This requirement is a necessary component of the classical EC′ mechanism and is demonstrated for our system by the lack of oxidative current in CV of CNT–DNA alone (below the irreversible oxidation at ~1100 mV) (Figure 4.5). This observation is consistent with slow ET kinetics for the direct oxidation of CNT–DNA (6) at ITO, resulting in no appreciable heterogeneous oxidation of CNT–DNA during the CV and allowing the observed catalysis in CVs of metal with CNT–DNA to occur. Since direct oxidation of CNT–DNA is too slow to generate oxidized CNT under our experimental conditions, $k_2$ (6) was set to zero in all simulations (and will be omitted from

the discussions below). The parameters obtained from simulating the metal mediators in the absence of CNT–DNA (Table 4.2) were employed to describe the behavior of each metal in simulations with CNT–DNA; parameters pertaining to the CNT–DNA are discussed below.

***Diffusion of DNA-Wrapped Carbon Nanotubes.*** To determine the rate of CNT–DNA diffusion, the CNT–DNA was modeled as a rigid rod in solution. Rigid-rod behavior has been demonstrated experimentally for CNT–DNA[42] and can be described mathematically for dilute solutions (9).[43, 44] The diffusion coefficient (D) depends on the ratio (ρ) of rod length (L) to diameter, temperature (T), native solvent viscosity (η), and Boltzmann's constant (k).

$$D = \frac{k\,T}{3\,\pi\,\eta\,L}\left[\ln\rho + 0.312 + 0.565\rho^{-1} - 0.100\rho^{-2}\right] \quad (9)$$

This equation demonstrates that the diffusion coefficient of CNT–DNA is much less sensitive to diameter than to length. For CNT–DNA with 0.8-nm diameter (as in our sample), and 144-nm length (which is the average length in our sample; refer to Chapter 3), $D = 1.9 \times 10^{-7}$ cm$^2$ s$^{-1}$. Within one standard deviation of CNT–DNA lengths in our sample, the diffusion coefficient is expected to vary from $6.2 \times 10^{-7}$ cm$^2$ s$^{-1}$ (32-nm length) to $1.2 \times 10^{-7}$ cm$^2$ s$^{-1}$ (256-nm length). Using mechanisms discussed below, we investigated the impact of this diversity by incorporating two or three CNT–DNA populations, each with a different diffusion coefficient. However, the simulation parameters, as well as the quality of the simulated fit to the experimental data, were not considerably different compared to simulations in which all CNT–DNA diffused at the same rate. Therefore, a CNT–DNA diffusion coefficient of $1 \times 10^{-7}$ cm$^2$ s$^{-1}$ was used for the purposes of digital simulation.

***Concentration of DNA-Wrapped Carbon Nanotubes.*** The molar concentration of CNT–DNA in solution was approximated from the known mass concentration using the average molecular weight of CNTs in our sample (refer to the Experimental Section of Chapter 2). The concentration of CNT–DNA used in simulations is further discussed below.

***Homogeneous Rate Constants.*** Digital simulation of the extent of metal mediator oxidative current enhancement observed in experimental CVs yielded the rate constants for ET between the mediator and the CNT–DNA. Details are discussed below.

***Homogeneous Equilibrium Constants.*** The equilibrium constant (K) for the homogeneous ET from CNT–DNA to $M^{3+}$ reflects the thermodynamic driving force of the reaction and therefore increases with increasing metal redox potential (10).[1] When the $E_{1/2}$ of CNT–DNA was taken as 600 mV vs. Ag/AgCl, which is the reported redox potential of electrons in the first valence band of (6,5) CNTs,[18] K was calculated to range from $10^4$ to $10^8$ for reaction with the stronger metal oxidants, but was only 6 for $Os(bpy)_3^{3+/2+}$ and 49 for $Fe(dmb)_3^{3+/2+}$. Simulations with these latter two values resulted in a slight increase in reductive current that did not match experimental CVs; however, K values calculated when the $E_{1/2}$ of CNT–DNA was taken as 500 mV were increased and better simulated the experimental data. In practice, a value of $K = 1 \times 10^4$ was sufficiently large to reflect the forward direction of the homogeneous reaction with *any* of the metal mediators, and inputting larger equilibrium constants as metal redox potential increased had no effect on the resulting simulations. Therefore, a homogeneous equilibrium constant of $1 \times 10^4$ was used in simulations with all metal mediators.

$$(10) \qquad K = \exp\left[\frac{n F \left\{ E_{1/2}\left(M^{3+/2+}\right) - E_{1/2}\left(CNT^{+/0}\right) \right\}}{R T}\right]$$

***Simulation Mechanism.*** CVs of metal mediators in the presence of CNT–DNA were simulated using the EC′ catalytic mechanism (5, 7) and parameters described above. Simulation of CVs collected with 25 μM $Ru(bpy)_3^{2+}$ and ~59 nM CNT–DNA in which $CNT_1$ = 59 nM (and $k_1'$ had any value) did *not* fit the experimental data (Figure 4.13A). The concentration of CNT–DNA is several orders of magnitude lower than the concentration of metal, which means that even very fast homogeneous ET has a negligible effect on the metal CV, producing a simulation that resembles the experimental CV in the absence of CNT–DNA. This simulation clearly demonstrates that *more than one electron is available per CNT–DNA* to reduce the electrogenerated $M^{3+}$, consistent with a previous report.[18]

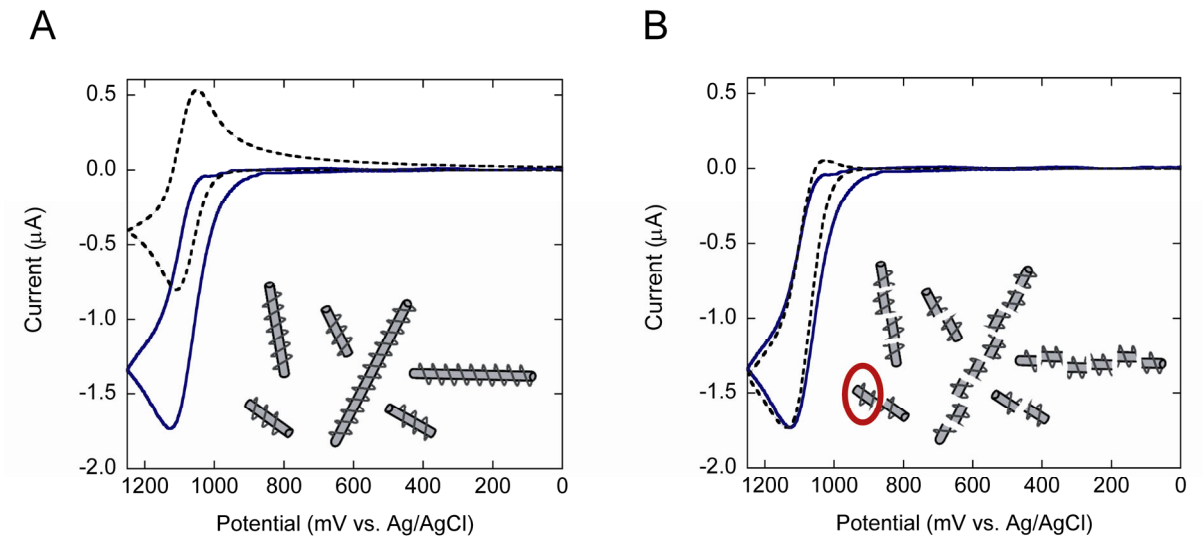


**Figure 4.13 Digital simulation of metal-mediated CNT–DNA oxidation by one versus multiple electrons per CNT.** An experimental CV of $Ru(bpy)_3^{3+/2+}$ (25 μM) with CNT–$T_{60}$ (10 μg $mL^{-1}$ ≈ 59 nM CNT) in 100 mM sodium phosphate buffer, pH 7.0, collected at 25 mV $s^{-1}$ is shown in blue. Simulations (dotted black lines) employing an EC′ mechanism with (A) 59 nM ($k_1'$ = any value) and (B) 138 μM $CNT_1$ ($k_1' = 1 \times 10^4$ $M^{-1}$ $s^{-1}$) demonstrate the availability of more than one electron per CNT–DNA. The increased concentration of $CNT_1$ necessary to simulate the data represents a concentration of redox-active sites available in the CNT–DNA (depicted in inset images; one redox site is circled in red). Instead of a molar concentration of CNT–DNA calculated from an average CNT–DNA length (A), a concentration of identically sized pieces of CNT–DNA (redox sites) was input into simulations (B).

Our simulations of metal-mediated CNT–DNA oxidation therefore need to account for the loss of multiple electrons per CNT–DNA to $M^{3+}$. Simplistically, each CNT–DNA can be conceptualized as a collection of independent *redox-active sites*, each of which provides one electron to the metal mediator. This formalism is analogous to the treatment of conductive polymers with multiple ET sites per chain[45] and allowed us to simulate our metal-mediated CV. Simulation with a higher value of $CNT_1$ produced a CV that closely resembled the experimentally observed CV (Figure 4.13B), suggesting ~2000 redox sites per CNT–DNA are oxidized by $Ru(bpy)_3^{3+}$ (a result elaborated upon below). An additional advantage of simulating with a molar concentration of identically sized redox sites, rather

than the molar concentration of CNT–DNA, is that no assumption of an average CNT–DNA molecular weight is required (depicted by the inset representations of whole CNT–DNA versus redox sites in Figure 4.13).

Using this EC′ mechanism in which $CNT_1$ has a concentration equal to the concentration of CNT–DNA redox-active sites (and $k_1'$ is the rate constant for homogeneous ET), we attempted to simulate CVs of 25 μM $Ru(bpy)_3^{2+}$ in the presence of ~59 nM CNT–DNA collected at different scan rates. However, data at varying scan rate revealed a limitation of this mechanism: the simulation parameters that fit data at slow scan rate did not fit data at faster scan rate (Figure 4.14). Instead, simulations that described data at faster scan rate required a faster homogeneous ET rate constant. This result suggests there are different rate constants for the loss of different CNT–DNA electrons. Simulating with a single rate constant in a simple EC′ mechanism forces $k_1'$ to serve as an *average* rate constant; this will appear to be larger at faster scan rate because the experiment outruns slower ET processes.

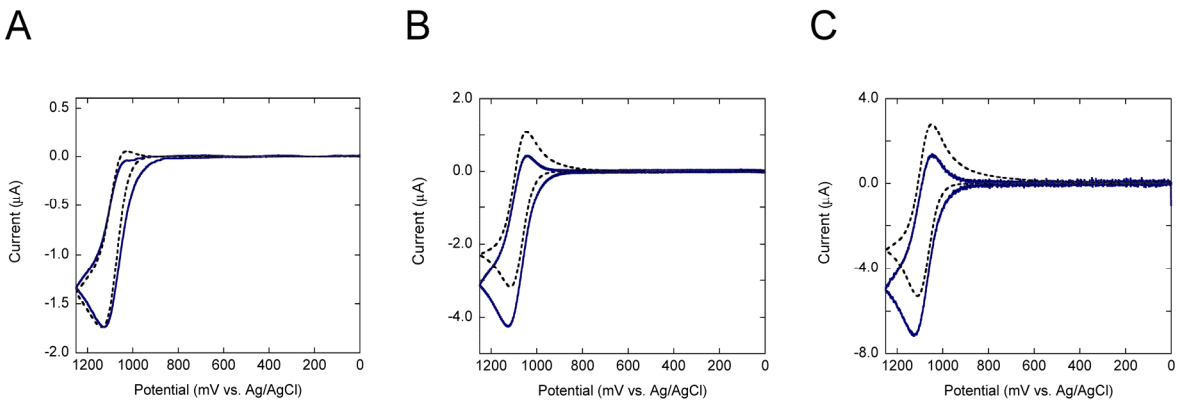


**Figure 4.14 Attempted digital simulation of metal-mediated CNT–DNA oxidation with an EC′ mechanism.** Experimental CVs of $Ru(bpy)_3^{3+/2+}$ (25 μM) with CNT–$T_{60}$ (10 μg $mL^{-1}$ ≈ 59 nM CNT) in 100 mM sodium phosphate buffer, pH 7.0, collected at (A) 25, (B) 300, and (C) 1000 mV $s^{-1}$ are shown in blue. Simulations employing an EC′ mechanism (dotted black lines) with identical parameters at each scan rate (chosen to fit the data in A: $CNT_1$ = 138 μM, $k_1' = 1 \times 10^4$ $M^{-1}$ $s^{-1}$) do not fit the data at faster scan rate.

***Three Singly Oxidized Populations of Redox-Active Sites.*** It is unsurprising that a simple EC′ mechanism with one homogeneous rate constant is insufficient to describe the ET of CNT–DNA, given both the heterogeneity of CNT chiral types present in our sample and the dispersion of $CNT^{+/0}$ redox potentials for valence electrons in each type of CNT. This diversity of CNT–DNA redox potentials causes variation in the favorability of CNT–DNA oxidation by any given metal mediator (8), which in turn is expected to vary the homogeneous ET rate constant (11).[1]

$$(11) \qquad k_1' \; \alpha \; \exp\left\{\frac{-(\lambda + \Delta G^\circ)^2}{4RT\lambda}\right\}$$

We therefore modified the catalytic mechanism to allow for ET with three different rate constants. This $EC_1'C_2'C_3'$ mechanism splits the total CNT–DNA redox sites into three

populations ($CNT_1$, $CNT_2$, and $CNT_3$), representing electrons that are removed at a faster, intermediate, and slower rate (with rate constants $k_1'$, $k_2'$, or $k_3'$, respectively, in reactions 13, 14, and 15). Simulation with these three redox-site populations was established after an attempt to simulate with only two rate constants revealed the same difficulty in fitting the experimental data at all scan rates as we observed for simulation with a single rate constant.

(12) $M^{2+} \rightarrow M^{3+} + e^-$

(13) $M^{3+} + CNT_1 \rightarrow M^{2+} + CNT_1^+, \quad k_1'$

(14) $M^{3+} + CNT_2 \rightarrow M^{2+} + CNT_2^+, \quad k_2'$

(15) $M^{3+} + CNT_3 \rightarrow M^{2+} + CNT_3^+, \quad k_3'$

Using this $EC_1'C_2'C_3'$ mechanism (12–15), we simulated CV data for CNT–DNA in the presence of different metal mediators. The experimentally observed increase in catalytic current with increasing metal redox potential suggests that stronger metal oxidants either remove electrons faster than weaker oxidants or actually remove more electrons than weaker oxidants. To model *faster ET* at higher metal redox potential, simulations were attempted with fixed concentrations of redox sites ($CNT_1$, $CNT_2$, and $CNT_3$) and varying ET rate constants ($k_1'$, $k_2'$, and $k_3'$) (Figure 4.15B). To model the loss of *more electrons* from CNT–DNA at higher metal redox potential, simulations had varying concentrations of redox sites and fixed ET rate constants (Figure 4.15C). The model with varying ET rate constants failed to fit the experimental data (regardless of the values chosen for the rate constants), while the model with varying redox site concentrations well-described the data for all metal mediators. Simulation of CNT–DNA CVs with different metal mediators required increased

concentrations of CNT–DNA redox sites as the metal redox potential increased, suggesting *more electrons are available from CNT–DNA to stronger metal oxidants*.

Analysis of data collected at varying scan rate can often reveal a faulty or incomplete simulation mechanism because faster scan rate can outrun ET reactions and different electrochemical processes have different scan rate dependencies. Unlike the simple EC′ mechanism, simulations employing three different rate constants for the oxidation of CNT–DNA in the $EC_1'C_2'C_3'$ mechanism were consistent with all experimental data. The same simulation parameters for CNT–DNA oxidation by a given metal mediator fit the experimental data collected at three CV scan rates (Figure 4.16; Table 4.3). Additionally, experimental data with varying concentrations of metal mediator or CNT–DNA were well-described by the same mechanism and parameters (Figure 4.17). The good agreement between simulated and experimental CVs collected under different conditions supports the $EC_1'C_2'C_3'$ mechanism as a description for the metal-mediated oxidation of CNT–DNA.

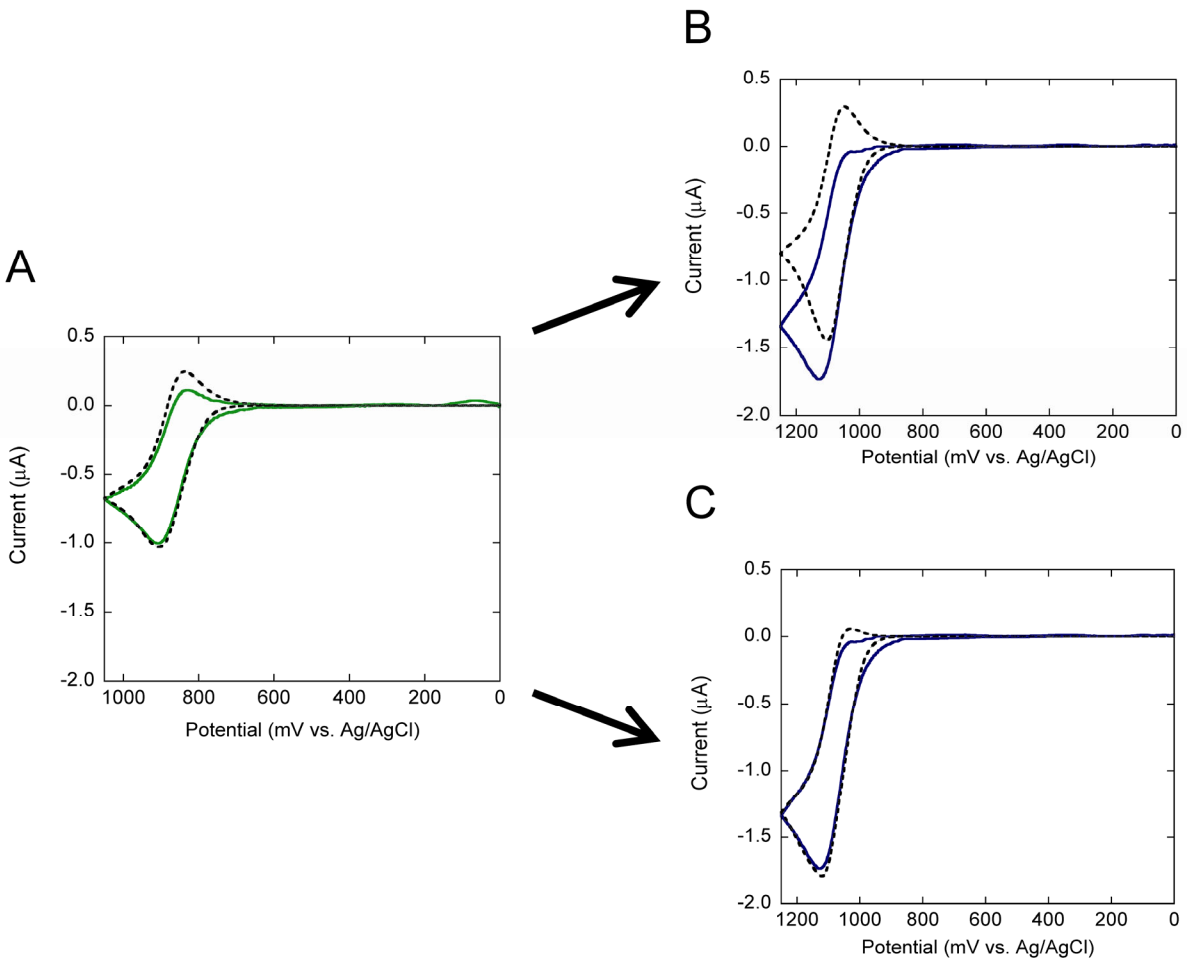


**Figure 4.15 Digital simulation of CNT–DNA oxidation mediated by different metals with either different ET rate constants or different concentrations of redox sites.** (A) An experimental CV of $Fe(bpy)_3^{3+/2+}$ (25 μM) with CNT–$T_{60}$ (10 μg $mL^{-1}$ ≈ 59 nM CNT) can be simulated using an $EC_1'C_2'C_3'$ mechanism ($k_1' = 5.0 \times 10^5$, $k_2' = 3.0 \times 10^4$, and $k_3' = 8.0 \times 10^3$ $M^{-1}s^{-1}$; $CNT_1$ = 12, $CNT_2$ = 8, and $CNT_3$ = 25 μM). (B) Attempts to simulate an experimental CV of $Ru(bpy)_3^{3+/2+}$ (25 μM) with CNT–$T_{60}$ (10 μg $mL^{-1}$ ≈ 59 nM CNT) by increasing the homogeneous rate constants in A failed to describe the experimental CV ($k_1' = 1.0 \times 10^6$, $k_2' = 5.0 \times 10^5$, and $k_3' = 1.0 \times 10^5$ $M^{-1}s^{-1}$; $CNT_1$ = 12, $CNT_2$ = 8, and $CNT_3$ = 25 μM; further increases in rate constants did not improve the simulation fit to the data). (C) In contrast, simulation of $Ru(bpy)_3^{3+/2+}$ with CNT–$T_{60}$ by increasing the concentrations of redox sites in A well-described the experimental data ($k_1' = 5.0 \times 10^5$, $k_2' = 3.0 \times 10^4$, and $k_3' = 8.0 \times 10^3$ $M^{-1}s^{-1}$; $CNT_1$ = 30, $CNT_2$ = 21, and $CNT_3$ = 90 μM). Experimental CVs in 100 mM sodium phosphate buffer, pH 7.0, collected at 25 mV $s^{-1}$ are shown in color; simulations are dotted black lines.

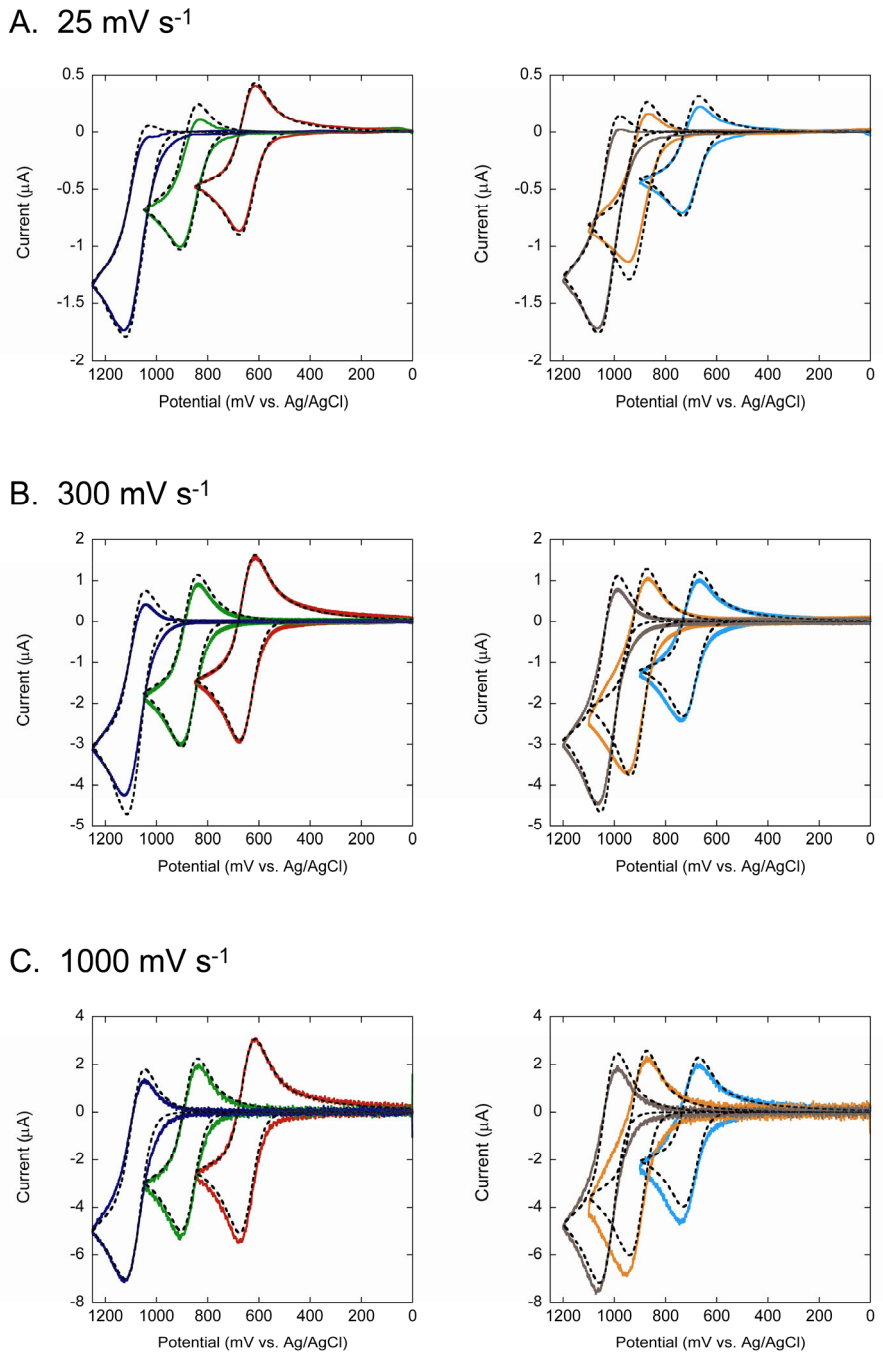


**Figure 4.16 Digital simulation of metal-mediated CNT–DNA oxidation with an $EC_1'C_2'C_3'$ mechanism.** Experimental CVs of metal mediators (25 µM) with CNT–$T_{60}$ (10 µg $mL^{-1}$ ≈ 59 nM CNT) in 100 mM sodium phosphate buffer, pH 7.0, collected at (A) 25, (B) 300, and (C) 1000 mV $s^{-1}$ are shown in color. Simulations employing an $EC_1'C_2'C_3'$ mechanism (dotted black lines) have identical parameters at each scan rate (Table 4.3). For clarity, data with the six metal mediators are separated into two plots; $Ru(bpy)_3^{3+/2+}$ (blue), $Fe(bpy)_3^{3+/2+}$ (green), $Os(bpy)_3^{3+/2+}$ (red), $Ru(bpy)_2(dmb)^{3+/2+}$ (brown), $Ru(dmb)_3^{3+/2+}$ (orange), and $Fe(dmb)_3^{3+/2+}$ (light blue). $Os(dmb)_3^{3+/2+}$ is not shown because it did not oxidize CNT–DNA and thus required no simulation.

**Table 4.3 Digital Simulation Parameters of an $EC_1'C_2'C_3'$ Mechanism Describing Metal-Mediated CNT–DNA Oxidation[a]**

| | Redox Potential (mV vs. Ag/AgCl) | Bulk Concentration of $CNT_1$ (μM) | Bulk Concentration of $CNT_2$ (μM) | Bulk Concentration of $CNT_3$ (μM) | Total Bulk Concentration of Redox Sites (μM) |
|---|---|---|---|---|---|
| $Os(bpy)_3^{3+/2+}$ | 645 | 4 | 2 | 8 | 14 |
| $Fe(dmb)_3^{3+/2+}$ | 700 | 5 | 4 | 10 | 19 |
| $Fe(bpy)_3^{3+/2+}$ | 870 | 12 | 8 | 25 | 45 |
| $Ru(dmb)_3^{3+/2+}$ | 905 | 15 | 10 | 30 | 55 |
| $Ru(bpy)_2(dmb)^{3+/2+}$ | 1020 | 20 | 15 | 70 | 105 |
| $Ru(bpy)_3^{3+/2+}$ | 1080 | 30 | 21 | 90 | 141 |

[a] Redox site concentrations are reported for simulations fit to CVs of 25 μM metal mediators with 10 μg $mL^{-1}$ ≈ 59 nM CNT–$T_{60}$. Homogeneous rate constants of $k_1' = 5.0 \times 10^5$, $k_2' = 3.0 \times 10^4$, and $k_3' = 8.0 \times 10^3$ $M^{-1}s^{-1}$ were held constant for reaction with $CNT_1$, $CNT_2$, and $CNT_3$ (respectively) with all metals.

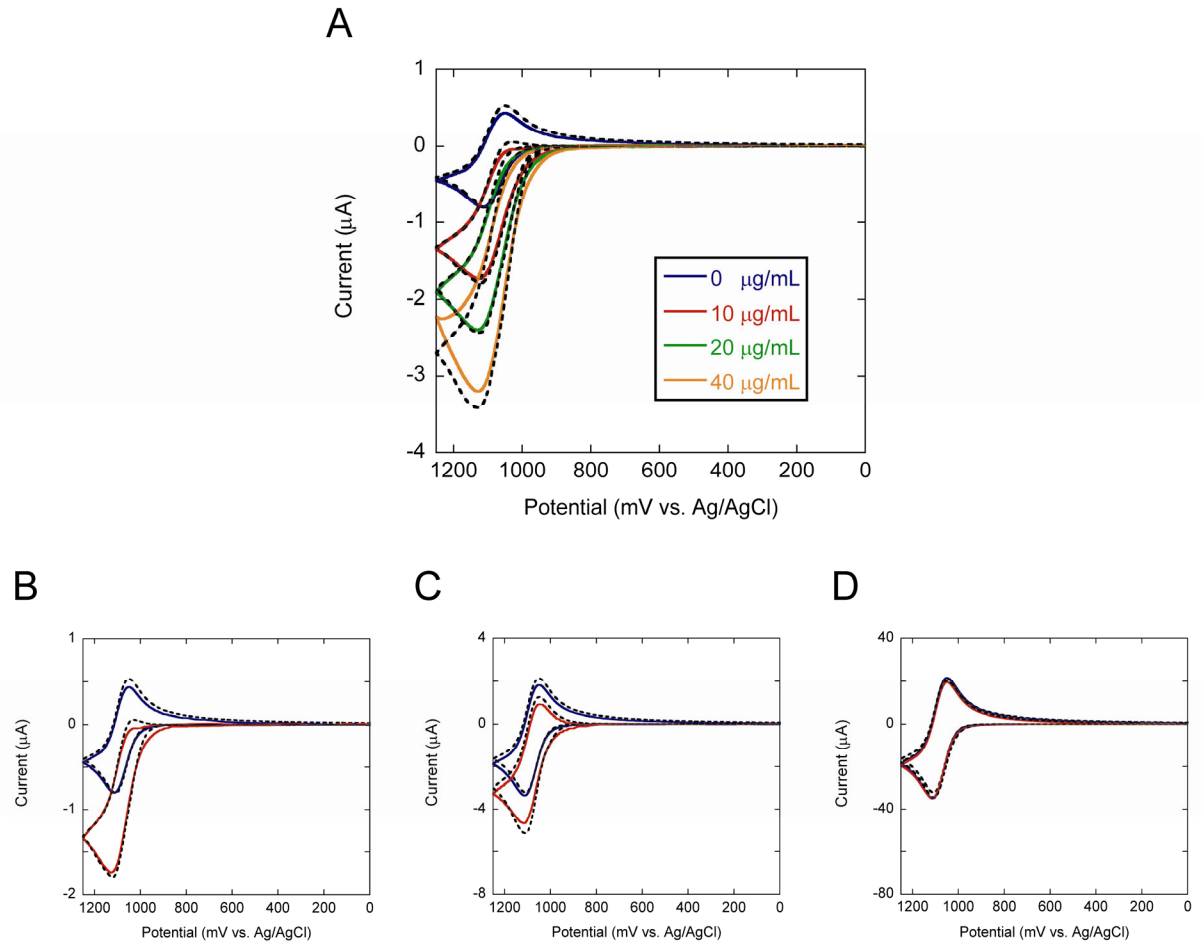


**Figure 4.17 Digital simulation of metal-mediated CNT–DNA oxidation at varying concentrations of CNT–DNA and metal.** (A) CVs of $Ru(bpy)_3^{3+/2+}$ (25 μM) alone and with increasing concentrations of CNT–$T_{60}$ (10 μg $mL^{-1}$ ≈ 59 nM, 20 μg $mL^{-1}$ ≈ 118 nM, and 40 μg $mL^{-1}$ ≈ 235 nM CNT). For a constant CNT–DNA concentration (10 μg $mL^{-1}$ ≈ 59 nM), CVs were collected at (B) 25, (C) 100, and (D) 1000 μM $Ru(bpy)_3^{3+/2+}$ in the absence (blue) and presence (red) of CNT–$T_{60}$. Experimental CVs collected in 100 mM sodium phosphate buffer, pH 7.0, at 25 mV $s^{-1}$ are shown in color; simulations with an $EC_1'C_2'C_3'$ mechanism using the same parameters under all conditions are dotted black lines. Simulation parameters are the same as those in Table 4.3 except the concentrations of redox sites were doubled and quadrupled for data with 20 and 40 μg $mL^{-1}$ CNT–DNA, respectively.

Experimental data for all six metal mediators, at all scan rates, were well-described by the same three rate constants ($k_1' = 5.0 \times 10^5$, $k_2' = 3.0 \times 10^4$, and $k_3' = 8.0 \times 10^3$ $M^{-1}s^{-1}$; Figure 4.16). These values best fit the experimental data, but simulation with increased or decreased rate constants suggests that three rate constants on the order of $10^3$, $10^4$, and $10^5$ can describe the experimental CVs. At faster scan rate, ET with the $10^3$ and $10^4$ rate constants is largely outrun by the experiment; however, these slower processes are critical to simulating the data at slower scan rate. While there is likely a large distribution of ET rate constants for the various electrons in CNT–DNA, employing three rate constants appears sufficient to describe the ET occurring in metal-mediated CV. Their values represent averages for ET with different electrons in the valence bands of the various CNT types present in CNT–DNA, offering a representation of CNT–DNA solution ET.

These rate constants might be expected to increase with increasing metal redox potential (8, 11); however, the redox site concentrations did not appreciably change when the rate constants were varied to best fit each metal mediator, and no trend was observed with metal redox potential. These results suggest that the primary influence of metal redox potential is on the concentration of CNT–DNA redox sites, i.e., the concentration of electrons available to the metal oxidant, which was found to increase exponentially with increasing metal redox potential. No assumptions were made regarding the proportion of CNT–DNA redox sites that should react at each ET rate constant, yet simulation revealed an exponential increase in all three electron populations ($CNT_1$, $CNT_2$, and $CNT_3$), suggesting the number of electrons that can be removed from one CNT–DNA increases exponentially as the oxidizing power of the metal mediator increases (Figure 4.18). The simulations suggest the total number of redox sites per CNT–DNA ranges from ~200 to 2000 as the metal redox potential

increases from 645 mV ($Os(bpy)_3^{3+/2+}$) to 1080 mV ($Ru(bpy)_3^{3+/2+}$). The size of these redox sites ranges from ~6 to 0.6 angstroms of length along a 0.8-nm-diameter CNT, with each site containing a range of ~60 to 6 carbon atoms (Table 4.4). These calculations suggest $Os(bpy)_3^{3+}$ can remove one electron per ~60 CNT carbon atoms, while the stronger $Ru(bpy)_3^{3+}$ oxidant can remove one electron per ~6 carbons of CNT. This considerable CNT–DNA oxidation is discussed below in terms of the CNT electronic band structure and compared to other evidence for the extent of CNT–DNA oxidation.

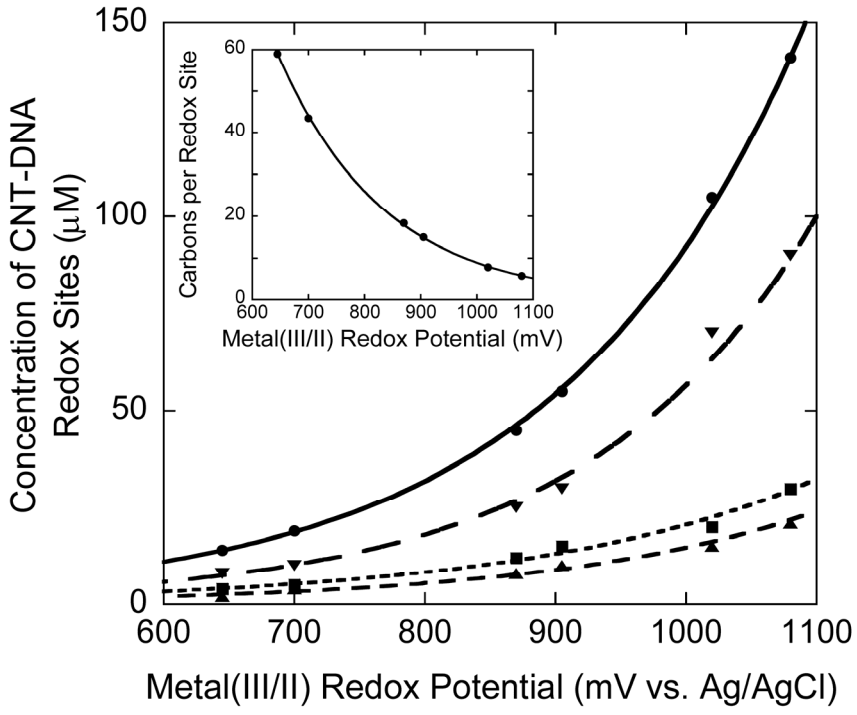


**Figure 4.18 Concentration of CNT–DNA electrons available to different metal mediators.** The concentration of CNT–$T_{60}$ redox sites (i.e., available electrons) in 10 μg $mL^{-1}$ ≈ 59 nM CNT–DNA (determined by $EC_1'C_2'C_3'$ simulation, Table 4.3) increased exponentially with the redox potential of the metal oxidant. This increase was observed for the concentration of $CNT_1$ (squares), $CNT_2$ (triangles), $CNT_3$ (inverted triangles), and the total redox sites available for ET at any rate (circles). Inset data show the number of carbon atoms per redox site, calculated from the total redox sites accessible to each metal mediator; an exponential relationship describes the data with the equation: Carbons per redox site = $1821 \times e^{-0.0053(\text{metal redox potential})}$ ($R^2 = 0.999$).

**Table 4.4 Extent of CNT–DNA Oxidation during Metal-Mediated Cyclic Voltammetry**

| | Metal Redox Potential (mV vs. Ag/AgCl) | Number of Redox Sites per CNT–DNA[a] | CNT Length Corresponding to One Redox Site[b] (angstroms) | Number of Carbon Atoms Per Redox Site[c] |
|---|---|---|---|---|
| $Os(bpy)_3^{3+/2+}$ | 645 | 237 | 6.1 | 59 |
| $Fe(dmb)_3^{3+/2+}$ | 700 | 322 | 4.5 | 44 |
| $Fe(bpy)_3^{3+/2+}$ | 870 | 763 | 1.9 | 18 |
| $Ru(dmb)_3^{3+/2+}$ | 905 | 932 | 1.5 | 15 |
| $Ru(bpy)_2(dmb)^{3+/2+}$ | 1020 | 1780 | 0.8 | 8 |
| $Ru(bpy)_3^{3+/2+}$ | 1080 | 2390 | 0.6 | 6 |

[a] Calculated from the total bulk concentration of redox sites in ~59 nM CNT–DNA determined by simulations with an $EC_1'C_2'C_3'$ mechanism (Table 4.3).

[b] Length along the CNT; calculated for a CNT of average length (144 nm).

[c] Calculated by assuming ~14,000 carbons in a 144-nm CNT (see Experimental Section of Chapter 2).

***Effect of Metal Redox Potential.*** Our conclusion that more CNT–DNA redox sites become available as the metal mediator redox potential increases reflects the electronic structure of the CNT valence band. The lack of CNT–DNA oxidation by $Os(dmb)_3^{3+/2+}$ suggests its redox potential of 460 mV is within the bandgap of most CNTs in our CNT–DNA (where there are no electronic states). In contrast, the observation of CNT–DNA oxidation by $Os(bpy)_3^{3+/2+}$ suggests its redox potential of 645 mV is beyond the first valence van Hove singularity for at least some CNTs in our CNT–DNA. This finding is consistent with previous reports of $E_{1/2} \approx 580$ or 600 mV for first-valence band electrons (of the major CNT type in our sample)[18, 41] and is supported by our spectroscopic observations for the chemical oxidation of CNT–DNA by $Os(bpy)_3^{3+}$, which show the removal of first-valence electrons for all CNT chiral types present in our sample (Figure 4.10). Spectroscopy also shows the removal of first-valence and some second-valence CNT electrons by an oxidant such as $IrCl_6^{2-}$ or $Fe(dmb)_3^{3+}$ with a redox potential of 700 mV (Figure 2.6; this result is further discussed below). From these observations, we can compare the approximate position of the CNT Fermi level upon reaction with each metal oxidant (Figure 4.19). The Fermi level is shifted further into the valence band as the metal redox potential increases, demonstrating the increased number of valence electrons removed from a CNT as the redox potential of the metal oxidant increases. This trend is expected to continue for the other metal mediators studied, since we observed more metal-mediated CNT–DNA oxidation as the redox potential of the metal increased. Our conclusion from CV simulation that more electrons are removed by stronger metal oxidants is therefore an expected consequence of CNT band structure.

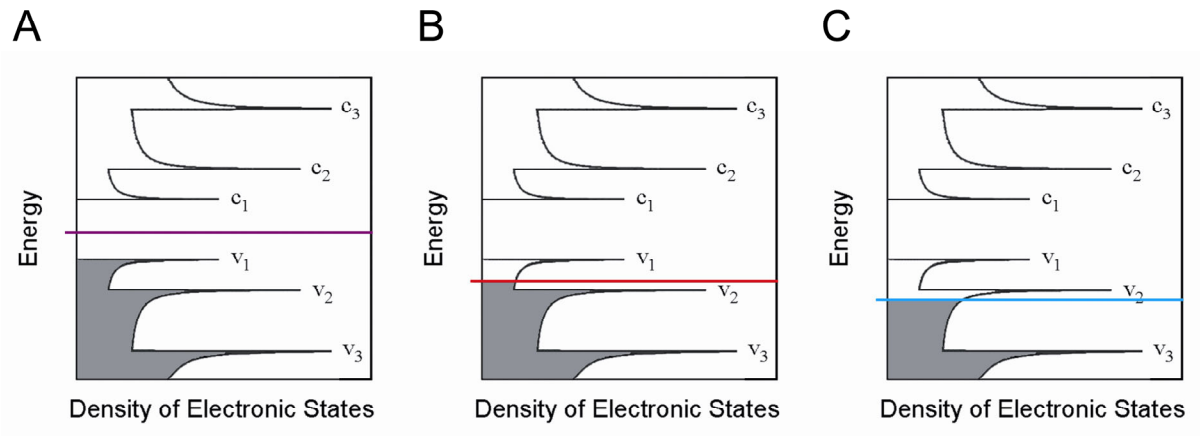


**Figure 4.19 Effect of metal redox potential on the CNT density of electronic states.** The approximate position of the CNT Fermi level (colored lines) for the predominant CNT chiral type in our CNT–$T_{60}$ during oxidation by (A) $Os(dmb)_3^{3+/2+}$ ($E_{1/2}$ = 460 mV), (B) $Os(bpy)_3^{3+/2+}$ (645 mV), and (C) $Fe(dmb)_3^{3+/2+}$ (700 mV) based on observations from CV and absorbance spectroscopy. Shading shows states filled with electrons; $c_1$, $v_1$, etc., designate van Hove singularities in the conduction and valence bands. The band nature of CNT electrons explains the observation from CV simulations that more electrons are available to metal mediators of higher redox potential.

For a single CNT chiral type, the number of available valence electrons does not increase smoothly as oxidant redox potential increases because electronic states are concentrated at particular energies (the van Hove singularities $v_1$, $c_1$, etc., in Figure 4.19). These energies effectively define the redox potentials of the majority of electrons in each valence band.[14, 15, 17] Since the van Hove singularity energies vary with the structure of each CNT, the presence of many CNT types in our CNT–DNA creates a distribution of van Hove singularities and thus redox potentials. This distribution is related to the energy distribution of CNT $E_{11}$ and $E_{22}$ absorptions (representing excitation of electrons in the first and second valence van Hove singularities, respectively), which are observed to nearly continuously overlap in the 400–1300 nm region of absorbance spectra (Figure 2.4). Our finding of a smooth increase in the number of available electrons with increasing metal redox potential (in the 645–1080 mV range; Figure 4.18) is consistent with a fairly continuous distribution of

redox potentials for CNT electrons. The observation of a direct, exponential relationship between the number of available electrons in CNT–DNA and the metal redox potential suggests an exponential increase in the number of electrons available deeper into the valence bands of the CNTs present.

***Comparison to Solution Redox Titration.*** The number of CNT–DNA electrons available to an oxidant can be directly quantified through a spectrophotometric redox titration of CNT–DNA.[18] Since $Ru(bpy)_3^{3+}$ and other $M^{3+}$ oxidants generated in our electrochemical experiments are unstable in neutral solution, we used the more stable $IrCl_6^{2-}$ oxidant for redox titration, which has $E_{1/2}(Ir^{4+/3+})$ = 700 mV vs. Ag/AgCl. A CNT–DNA solution of known absorbance was titrated with a known concentration of $IrCl_6^{2-}$ to determine the $IrCl_6^{2-}$ concentration required for complete reaction (details are described in Chapter 2). Since $IrCl_6^{2-}$ is a one-electron oxidant, the $IrCl_6^{2-}$ concentration needed to reach the endpoint is equal to the total concentration of CNT–DNA electrons removed by $IrCl_6^{2-}$. This value is expected to closely approximate the CNT–DNA electrons available to $Fe(dmb)_3^{3+}$, which also has a one-electron reduction potential of 700 mV.

The titration therefore provides a direct conversion between the CNT–DNA solution absorbance and the molar concentration of electrons available to a chemical oxidant with a one-electron redox potential of 700 mV. Without making any assumptions about CNT length or molecular weight, the titration shows removal of ~39 μM electrons per absorbance unit of CNT–DNA (at 990 nm, measured with 1-cm path length), while simulation of $Fe(dmb)_3^{3+/2+}$-mediated CV suggests removal of ~25 μM electrons per absorbance unit of CNT–DNA (calculated from Table 4.3). When an average molecular weight of 170,000 g $mol^{-1}$ is assumed for CNT–DNA, the redox titration suggests the availability of ~500 electrons per

CNT–DNA and $Fe(dmb)_3^{3+/2+}$-mediated CV suggests ~322 electrons per CNT–DNA. The similarity of these results, despite differences between the two types of experiments and the complexity of the simulation mechanism, supports our method of CV simulation.

***Comparison to Polycyclic Aromatic Hydrocarbons and Previous Reports.*** Another useful comparison is between the CNT–DNA redox sites and polycyclic aromatic hydrocarbons of the same size. Simulation suggests that $Fe(bpy)_3^{3+}$ can remove one electron from every 18 carbons of nanotube. This 18-carbon redox site is similar to tetracene ($C_{18}H_{12}$), which has a one-electron oxidation potential of 770 mV in acetonitrile vs. SCE[46] (the saturated calomel electrode). This value can be directly compared to the $Fe(bpy)_3^{3+/2+}$ redox potential of ~1070 mV vs. NHE in aqueous solution because a similarity has been demonstrated between aqueous potentials vs. NHE and acetonitrile potentials vs. SCE for polypyridine metal complexes.[47] The higher redox potential of $Fe(bpy)_3^{3+/2+}$ compared to tetracene suggests $Fe(bpy)_3^{3+}$ is a strong enough oxidant to remove one electron per 18 nanotube carbons. $Fe(dmb)_3^{3+}$ ($E_{1/2}$ = 900 mV vs. NHE) and $Os(bpy)_3^{3+}$ ($E_{1/2}$ = 845 mV vs. NHE) are also strong enough oxidants to oxidize tetracene. They should therefore be able to remove one electron from the predicted 44- and 59-carbon CNT–DNA redox sites, respectively (Table 4.4), which have a greater number of atoms to participate in delocalization and thus lower redox potentials than tetracene. These comparisons suggest that simulations for the metals of lower redox potential predict a reasonable extent of CNT–DNA oxidation.

Analogously, the removal of one electron per six nanotube carbons by $Ru(bpy)_3^{3+/2+}$ ($E_{1/2}$ = 1280 mV vs. NHE) can be compared to the one-electron oxidation potential of benzene ($C_6H_6$, $E_{1/2}$ = 2300 mV vs. SCE[46]). Not unexpectedly, $Ru(bpy)_3^{3+}$ falls short of the

ability to oxidize benzene by about one volt. However, the six-carbon CNT–DNA redox site predicted by simulations to be accessible to $Ru(bpy)_3^{3+/2+}$ is not an isolated benzene molecule but rather part of a highly delocalized system containing tens of thousands of $sp^2$-hybridized carbon atoms. This extent of delocalization will somewhat reduce the redox potential for oxidation of a 6-carbon CNT–DNA redox site compared to that of benzene. It should also be recognized that a six-carbon redox site in CNT–DNA does not suggest one oxidized site for every aromatic ring in the CNT, since the fused rings that comprise the nanotube share carbon atoms. Oxidation of a piece of CNT the size of coronene ($C_{24}H_{12}$) by $Ru(bpy)_3^{3+}$ would generate four delocalized holes, paired with phosphate anions of the supporting electrolyte. Additionally, the error in the determination of CNT–DNA redox-site sizes is difficult to quantify, as it mainly stems from the assumptions made during digital simulation. A redox site containing 10 carbons may be within the error of our determination and would be significantly easier for $Ru(bpy)_3^{3+}$ to oxidize (for comparison, naphthalene, $C_{10}H_8$, is oxidized with $E_{1/2}$ = 1540 mV vs. SCE[46]).

Others have observed chemical *reduction* of CNTs suspended in ethanol by one electron per 32 carbon atoms.[48] Films of CNT bundles have been reduced upon electrochemical charging by approximately one electron per four CNT carbon atoms,[49] while chemical redox with organic radical anions can reduce the films by one electron per six carbon atoms.[50] In both cases, the extent of CNT charging was determined by measuring the ratio of carbons to $Li^+$ ions that were intercalated into the CNT bundles to balance the charge.[50] *Oxidation* of CNT films by thionyl chloride removes one electron per ~60 carbons,[23] and oxidation by sulfuric acid has shown one electron can be removed from every ~6–20 carbon atoms,[51] which is consistent with our results for CNT–DNA. Like these

examples of charge-doping, our observation of extensive CNT–DNA oxidation by electrogenerated metal oxidants suggests that the tube ends cannot be the only site for the solution oxidation of CNTs. Instead, the CNT sidewalls also participate in ET (with a probable role for surface defect sites), consistent with studies of single-nanotube transistors.[25]

Some of the oxidized CNT–DNA generated during metal-mediated CV is expected to be spontaneously reduced, as we observed following CNT–DNA oxidation by $Os(bpy)_3^{3+}$ and $IrCl_6^{2-}$, while irreversible oxidative damage is likely at high positive potential, upon continuous electrolysis, or after repeated CV cycles. Future studies should address the stability of CNT–DNA to cycles of oxidation and reduction and investigate the extent and type of resulting surface functionalization. It may also prove informative to evaluate the metal-mediated oxidation of CNT–DNA enriched in one CNT chiral type and to replace the DNA with a surfactant such as sodium cholate.

## 4.6 Conclusions

Metal-mediated cyclic voltammetry has revealed the oxidation of CNT–DNA in solution by $Ru(bpy)_3^{3+}$ and similar electrogenerated oxidants. These oxidants bleach CNT absorption and show no reaction with DNA in the absence of CNT–DNA, demonstrating that the site of oxidation is the nanotube. Homogeneous ET between a metal mediator and CNT–DNA completes a catalytic cycle that gives rise to increased oxidative peak current compared to CV of the metal alone. We observed an increase in this current enhancement at higher CNT–DNA concentration, slower CV scan rate, and higher metal redox potential. These observations were shown via digital simulation to be consistent with a catalytic mechanism in which the metal oxidant removes electrons from CNT–DNA with rate constants on the

order of $10^3$, $10^4$, and $10^5$ $M^{-1}s^{-1}$. These rate constants reflect the varying redox potentials, and thus varying ease of oxidation, for different valence band electrons within one CNT chiral type and within the distribution of CNT types present in our CNT–DNA.

Metal mediators were shown to catalytically oxidize CNT–DNA to an extent dependent upon their $M^{3+/2+}$ redox potential. The lowest observed $CNT^{+/0}$ redox potential was within the range of 460–645 mV vs. Ag/AgCl, consistent with previous reports for oxidation of CNT first-valence band electrons.[18, 41] Above this potential, the number of electrons removed from CNT–DNA by a metal oxidant increased exponentially with the redox potential of the metal mediator, suggesting more electrons are accessible to stronger metal oxidants. This finding is consistent with the electronic band structure of CNTs; a stronger oxidant shifts the Fermi level deeper into the CNT valence band.

To quantify the number of electrons available per CNT–DNA to a given metal oxidant, we treated a CNT as a collection of redox-active sites, each of which provides one electron to the metal mediator. This approach well-described data for all metal mediators and also fit the data under conditions of varying metal and CNT–DNA concentration and varying CV scan rate, supporting the validity of the simulation mechanism and allowing us to approximate the size of the CNT redox site accessible to each metal oxidant. $Os(bpy)_3^{3+/2+}$ (with 645-mV redox potential) oxidized CNT–DNA by ~200 electrons per nanotube, amounting to one electron from every ~60 carbon atoms. $Fe(bpy)_3^{3+/2+}$ (with 870-mV redox potential) removed ~800 electrons per nanotube, or one electron from every ~18 carbon atoms. The extent of CNT–DNA oxidation observed with these metals is consistent with the results of a solution redox titration and the redox potentials of polycyclic aromatic hydrocarbons.

The strongest metal oxidant, $Ru(bpy)_3^{3+}$ (with 1080-mV redox potential), oxidized CNT–DNA by ~2000 electrons per nanotube, which is one electron from every ~6 carbon atoms. This extensive oxidation suggests a piece of CNT the size of coronene ($C_{24}H_{12}$) would be oxidized by four electrons, with the resulting holes delocalized over tens of thousands of $sp^2$-hybridized carbon atoms and paired with anions of the supporting electrolyte. Oxidized CNT–DNA generated during metal-mediated CV is expected to be susceptible to irreversible damage and otherwise spontaneously reduced (as we observed spectroscopically following chemical CNT–DNA oxidation).

There is an ongoing effort to describe the ET of CNTs, which has relevance to the controlled tuning of CNT electronic and optical properties, selective reaction of CNTs according to electronic type, and development of transistors, devices for charge storage, and chemical sensors. Our use of an electrochemical–chemical system to study CNT oxidation is a unique approach to the study of nanotube ET and has allowed for a qualitative and quantitative description of ET from CNTs in solution. Significantly, the extent of CNT oxidation observed in reactions with strong, electrogenerated metal oxidants suggests electrons can be removed from CNT sidewalls as well as tube ends.

## 4.7 References


1. Bard, A. J.; Faulkner, L. R. *Electrochemical Methods: Fundamentals and Applications*; John Wiley and Sons, Inc.: New York, 2001.

2. Johnston, D. H.; Cheng, C.-C.; Campbell, K. J.; Thorp, H. H. *Inorg. Chem.* **1994**, *33*, 6388-6390.

3. Johnston, D. H.; Glasgow, K. C.; Thorp, H. H. *J. Am. Chem. Soc.* **1995**, *117*, 8933-8938.

4. Rudolph, M.; Reddy, D. P.; Feldberg, S. W. *Anal. Chem.* **1994**, *66*, 589A-600A.

5. Weatherly, S. C.; Yang, I. V.; Thorp, H. H. *J. Am. Chem. Soc.* **2001**, *123*, 1236-1237.

6. Fecenko, C. J.; Thorp, H. H.; Meyer, T. J. *J. Am. Chem. Soc.* **2007**, *129*, 15098-15099.

7. Yang, I. V. *Oxidation of DNA by ruthenium polypyridyls. Thesis dissertation.*; The University of North Carolina at Chapel Hill: Chapel Hill, NC, 2000.

8. Lumpkin, R. S. *Analysis of Processes Controlling Excited State Decay in Polypyridyl Complexes of Ru(II) and Os(II). Thesis dissertation.*; The University of North Carolina at Chapel Hill: Chapel Hill, NC, 1987.

9. Ford-Smith, M. H.; Sutin, N. *J. Am. Chem. Soc.* **1961**, *83*, 1830-1834.

10. Juris, A.; Balzani, V.; Barigelletti, F.; Campagna, S.; Belser, P.; Zelewsky, A. v. *Coord. Chem. Rev.* **1988**, *84*, 85-277.

11. Kavan, L.; Rapta, P.; Dunsch, L.; Bronikowski, M. J.; Willis, P.; Smalley, R. E. *J. Phys. Chem. B* **2001**, *105*, 10764-10771.

12. Heller, I.; Kong, J.; Williams, K. A.; Dekker, C.; Lemay, S. G. *J. Am. Chem. Soc.* **2006**, *128*, 7353-7359.

13. Paolucci, D.; Franco, M. M.; Iurlo, M.; Marcaccio, M.; Prato, M.; Zerbetto, F.; Penicaud, A.; Paolucci, F. *J. Am. Chem. Soc.* **2008**, *130*, 7393-7399.

14. Kavan, L.; Frank, O.; Green, A. A.; Hersam, M. C.; Koltai, J.; Zolyomi, V.; Kurti, J.; Dunsch, L. *J. Phys. Chem. C* **2008**, *112*, 14179-14187.

15. Petit, P.; Mathis, C.; Journet, C.; Bernier, P. *Chem. Phys. Lett.* **1999**, *305*, 370-374.

16. O'Connell, M.; Eibergen, E. E.; Doorn, S. K. *Nat. Mater.* **2005**, *4*, 412-418.

17. Kazaoui, S.; Minami, N.; Matsuda, N. *Appl. Phys. Lett.* **2001**, *78*, 3433-3435.

18. Zheng, M.; Diner, B. A. *J. Am. Chem. Soc.* **2004**, *126*, 15490-15494.

19. Okazaki, K.-I.; Nakato, Y.; Murakoshi, K. *Phys. Rev. B* **2003**, *68*, 035434-1/5.

20. Kavan, L.; Rapta, P.; Dunsch, L. *Chem. Phys. Lett.* **2000**, *328*, 363-368.

21. Jacquemin, R.; Kazaoui, S.; Yu, D.; Hassanien, A.; Minami, N.; Kataura, H.; Achiba, Y. *Synth. Met.* **2000**, *115*, 283-287.

22. Collins, P. G.; Bradley, K.; Ishigami, M.; Zettl, A. *Science* **2000**, *287*, 1801-1804.

23. Blackburn, J. L.; Barnes, T. M.; Beard, M. C.; Kim, Y.-H.; Tenent, R. C.; McDonald, T. J.; To, B.; Coutts, T. J.; Heben, M. J. *ACS Nano* **2008**, *2*, 1266-1274.

24. Li, L.-J.; Nicholas, R. J. *Nanotechnology* **2004**, *15*, 1844-1847.

25. Heller, I.; Kong, J.; Heering, H. A.; Williams, K. A.; Lemay, S. G.; Dekker, C. *Nano Lett.* **2005**, *5*, 137-142.

26. Boussaad, S.; Diner, B. A.; Fan, J. *J. Am. Chem. Soc.* **2008**, *130*, 3780-3787.

27. Tarabek, J.; Kavan, L.; Dunsch, L.; Kalbac, M. *J. Phys. Chem. C* **2008**, *112*, 13856-13861.

28. Gooding, J. J.; Wibowo, R.; Liu, J.; Yang, W.; Losic, D.; Orbons, S.; Mearns, F. J.; Shapter, J. G.; Hibbert, D. B. *J. Am. Chem. Soc.* **2003**, *125*, 9006-9007.

29. Wang, J. *Electroanal.* **2005**, *17*, 7-14.

30. Gooding, J. J. *Electrochim. Acta* **2005**, *50*, 3049-3060.

31. Napier, M. E.; Hull, D. O.; Thorp, H. H. *J. Am. Chem. Soc.* **2005**, *127*, 11952-11953.

32. Kalyanasundaram, K. *Coord. Chem. Rev.* **1982**, *46*, 159-244.

33. Willit, J. L.; Bowden, E. F. *J. Phys. Chem. B* **1990**, *94*, 8241-8246.

34. Fagan, J. A.; Simpson, J. R.; Bauer, B. J.; Lacerda, S. H.; Becker, M. L.; Chun, J.; Migler, K. B.; Walker, A. R.; Hobbie, E. K. *J. Am. Chem. Soc.* **2007**, *129*, 10607-10612.

35. Demadis, K. D.; Dattelbaum, D. M.; Kober, E. M.; Concepcion, J. J.; Paul, J. J.; Meyer, T. J.; White, P. S. *Inorg. Chim. Acta* **2007**, *360*, 1143-1153.

36. Huang, X.; McLean, R. S.; Zheng, M. *Anal. Chem.* **2005**, *77*, 6225-6228.

37. Banks, C. E.; Crossley, A.; Salter, C.; Wilkins, S. J.; Compton, R. G. *Angew. Chem. Int. Ed.* **2006**, *45*, 2533-2537.

38. Kruusma, J.; Mould, N.; Jurkschat, K.; Crossley, A.; Banks, C. E. *Electrochem. Commun.* **2007**, *9*, 2330-2333.

39. Pumera, M. *Langmuir* **2007**, *23*, 6453-6458.

40. Burrows, C. J.; Muller, J. G. *Chem. Rev.* **1998**, *98*, 1109-1151.

41. Nish, A.; Nicholas, R. J. *Phys. Chem. Chem. Phys.* **2006**, *8*, 3547-3551.

42. Bauer, B. J.; Fagan, J. A.; Hobbie, E. K.; Chun, J.; Bajpai, V. *J. Phys. Chem. C* **2008**, *112*, 1842-1850.

43. Tirado, M. M.; Garcia de la Torre, J. *J. Chem. Phys.* **1979**, *71*, 2581-2587.

44. Eimer, W.; Pecora, R. *J. Chem. Phys.* **1991**, *94*, 2324-2329.

45. Flanagan, J. B.; Margel, S.; Bard, A. J.; Anson, F. C. *J. Am. Chem. Soc.* **1978**, *100*, 4248-4253.

46. Pysh, E. S.; Yang, N. C. *J. Am. Chem. Soc.* **1963**, *85*, 2124-2130.

47. Nazeeruddin, M. K.; Zakeeruddin, S. M.; Kalyanasundaram, K. *J. Phys. Chem.* **1993**, *97*, 9607.

48. Kongkanand, A.; Kamat, P. V. *ACS Nano* **2007**, *1*, 13-21.

49. Gao, B.; Kleinhammes, A.; Tang, X. P.; Bower, C.; Fleming, L.; Wu, Y.; Zhou, O. *Chem. Phys. Lett.* **1999**, *307*, 153-157.

50. Jouguelet, E.; Mathis, C.; Petit, P. *Chem. Phys. Lett.* **2000**, *318*, 561-564.

51. Zhou, W.; Vavro, J.; Nemes, N. M.; Fischer, J. E.; Borondics, F.; Kamaras, K.; Tanner, D. B. *Phys. Rev. B* **2005**, *71*, 205423-1/7.